

1 We thank the reviewer for their thoughtful comments which have improved the
2 manuscript. Line numbers refer to those in GMDD manuscript. New manuscript text is
3 italicized in the replies.

4

5 **Comment:** This study presents a description of a new atmospheric iron dissolution
6 scheme (MIMI) and compares the simulations with available cruise-based observations
7 in the literature. A comprehensive statistical analysis of the model comparison with the
8 observations is also presented. The authors further indicate the difference between the
9 iron solubility calculated at each time step in the model versus the offline one which is
10 routinely presented in most atmospheric Fe modeling studies and used in ocean models.
11 I find this an important finding of the current work on the importance of using online
12 parameterizations in Earth System Models that should be highlighted more in the text.

13 **Response:** We agree that the difference when using online results is an important finding
14 and have thus brought it forward to now be included within the abstract at L32 as follows,

15 *“Comparison of iron solubility calculated at each model time step versus that calculated*
16 *based on a ratio of the monthly mean values, which is routinely presented in aerosol*
17 *studies and used in ocean biogeochemistry models, are on average globally one-third*
18 *(34%) higher.”*

19 And in the results at end of first paragraph of Section 3.4,

20 *“Overall, global annual mean iron solubility calculated online is one-third (34%; NH=40%,*
21 *SH=29%) higher than when calculated offline.”*

22 and strengthened this point within the conclusions at L895 as follows,

23 *“There are significant differences in calculating iron solubility based on the order of the*
24 *averaging operation. When calculating at each model time-step global annual mean iron*
25 *solubility is one-third (34%; NH=40%, SH=29%) higher than when calculated from*
26 *monthly mean values. Earth-system models are designed to integrate land-atmosphere-*
27 *ocean-ice components at each time-step and thus could yield different results based on*
28 *the coupling time-step length employed. Furthermore, the mean [...]*”

29 **Comment:** MIMI is developed for use within Earth system models. Since Earth System
30 modeling is characterized by a heavy computational burden in simulating atmospheric
31 processes, it would be better to present some statistics and discuss more in the
32 manuscript on how much computationally expensive the new module is (e.g., MIMI
33 compared to the previous configuration or to the simple representation of soluble Fe -
34 such as using offline Fe solubility distributions on dust deposited aerosols in the ocean
35 (e.g., see Aumont et al., GMD, 2015, doi:10.5194/gmd-8-2465-2015), as well as on how
36 many species are required to be implemented in the model, etc.

37 **Response:** We agree that this is informative for future development in other models. New
38 methods text added in new Section 2.4.2,

39 *“2.4.2 Computational costs*

40 *Earth System models are generally characterized by having a heavy computational*
41 *burden in simulating atmospheric processes. The inclusion of MIMI requires eight dust*
42 *mineral tracers (a net addition of seven) and six iron tracers. The total addition of aerosol*
43 *tracers new is 39 (13 in each of the three aerosol modes) if dust mineralogy is not already*
44 *present, or 18 new aerosol tracers if it is (e.g., NASA GISS model (Perlwitz et al., 2015b,*
45 *2015a)). The additional computational cost of MIMI within CESM-CAM5 is approximately*
46 *a doubling of the required core-hours; around half of that is associated with dust*
47 *mineralogy speciation and the other half with iron speciation and processing (Table 6)*
48 *Note that additional computational tuning, or changes in configuration, could modify these*
49 *computational change estimates. For example, with dust mineralogy (MAM4DU8) there*
50 *is an approximate 3-fold increase in required core-hours due to model structural*
51 *differences when transitioning from CAM5 to CAM6.”*

52 Additional discussion relating to Reviewers comment about using offline estimates of iron
53 solubility added at L476 within Section 3.3,

54 *“In the absence of iron atmospheric process modelling, ocean biogeochemistry models*
55 *with an iron component (e.g., Aumont et al., 2015; Moore et al., 2004) have estimated*
56 *iron solubility from offline dust modelling by means of an assumption that it contains 3.5%*
57 *iron by weight, of which 2% is soluble. Iron solubility is highly temporally and spatially*

58 variable however, and in the absence of spatial atmospheric emission information,
 59 pyrogenic iron sources, and atmospheric processing of iron an estimate of 2% solubility
 60 leads to underestimates of observed iron solubility in nearly all HNLC ocean regions
 61 (Figure 4).”

62 New Table 6:

63 “Table 6: Simulation time (in seconds per simulated year) for the CESM-MAM4 model.
 64 The CAM5 base model, with the addition of dust mineralogy, and with the addition of dust
 65 mineralogy and iron processing (i.e., MIMI v1.0) shown in black text. Cost of running the
 66 new higher resolution CAM6 model with dust mineralogy also shown for comparison in
 67 blue text. All CAM5 simulations executed on 10 nodes, with 36 cores per node, for two
 68 years (2006-2007) with consistent output fields.”

	CAM5			CAM6
	MAM4 (Base model)	MAM4DU8 (dust mineralogy)	MAM4DU8FE6 (MIMIv1.0)	MAM4DU8 (dust mineralogy)
Number advected aerosol species	24	45	63	46
Gridcell resolution (#lon x #lat)	144x96	144x96	144x96	288x192
Wall clock s a ⁻¹ (simulation)	3954	5856	7836	20167
Core-hours	396	586	784	2017

69

70 **Comment:** P.8 line 221: It is stated that Fe emissions come from all eight mineral dust
 71 species. However, at the beginning of the Sect. 2.3.1 it is provided the Fe-fraction for 5
 72 dust species. Please explain.

73 **Response:** While MIMI carries 8 mineral dust species, only 5 of these provide iron. We
 74 have updated the manuscript to be clearer as follows:

75 “Iron emissions from *the five iron-bearing* mineral dust species (*three dust minerals*
 76 *contain no iron*) were then partitioned [...]”

77 **Comment:** Table 3. Is the med-soluble Fe the readily released Fe reported in Scanza et
78 al. (2018)? If this fraction represents the initial solubility of Fe-containing dust species,
79 why do the authors refer to it as “medium” soluble?

80 **Response:** The medium soluble iron tracer is the sum of the readily released (“fast”) iron
81 (soluble fraction at emission) and the iron which is created via medium reacting
82 atmospheric processing (additional soluble fraction created during transport). As Table 3
83 is referring to emissions we now add additional text to the caption to be clearer,

84 *“At emission med-soluble iron is equivalent to the fast-soluble iron fraction (i.e., the*
85 *fraction which is already assumed to be soluble at emission).”*

86 And in the main text at L224 as follows,

87 *“Note that, slow and med-soluble iron are only produced by non-reversible atmospheric*
88 *processing within the model; therefore, computational costs can be reduced by not*
89 *creating a separate iron tracer representing the fraction which is already soluble at*
90 *emission (i.e., ‘fast’ reacting), but instead add an initial med-soluble iron processed*
91 *emission burden which is equivalent to the assumed fast reacting iron fraction.”*

92 **Comment:** The Authors state that fire iron emissions were globally scaled by a uniform
93 factor of two. However, afterward, they stated that “Total iron emissions from fires in MIMI
94 were 2.2 Tg a⁻¹ Fe, representing an approximate increase in iron emissions from fires of
95 around 25% compared with those from BAM-Fe (see P.10 line 269)”. Is this because of
96 the different BC fire inventories used in the models? Please explain.

97 **Response:** The reviewer is correct that this is due to different fire inventories between
98 models. We have further highlighted this for the reader on L270 as follows,

99 *“The lower 25% increase between BAM-Fe and MIMI iron emissions, as compared to the*
100 *doubling of the fire iron emissions themselves within MIMI, is due to different underlying*
101 *fire emission inventories used in each model.”*

102 **Comment:** Section 2.3.3: The authors do not state the total iron emissions from
103 anthropogenic combustion sources as in the case of fire iron emissions (Sect. 2.3.2; line

104 232). Do the authors consider ship oil-combustion emission? If yes, do they apply the
105 same initially solubility (i.e., 4%) and in what sizes?

106 **Response:** We do not consider shipping emissions in this version of the model.

107 **Comment:** For completeness, it would be also useful to refer to the coarse fraction of
108 anthropogenic combustion iron (if any).

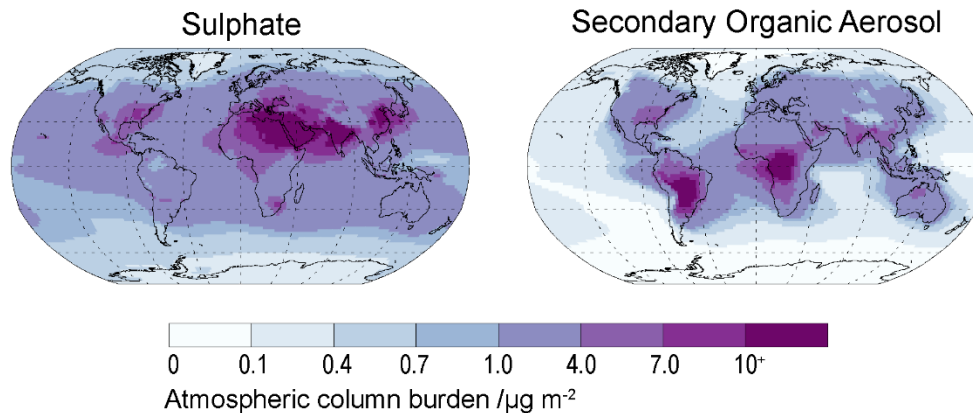
109 **Response:** We have added the following text at L284 as suggested,

110 *“Resulting fine mode anthropogenic combustion emissions were 0.50 Tg Fe a⁻¹ and*
111 *coarse mode emissions were 2.8 Tg Fe a⁻¹. Similar to fire emissions, 10% of fine size*
112 *emissions were partitioned into the Aiken mode at emission, the remainder 90% of fine*
113 *size emissions were emitted into the accumulation mode, and 100% of coarse size*
114 *emissions were emitted to the coarse mode.”*

115 **Comment:** Section 2.4: It is not clear in the manuscript how the model calculates SO₄
116 and SOA; i.e., the proxies of H⁺ and oxalate concentrations for the iron dissolution
117 scheme. Please give more details on their budget terms.

118 **Response:** Sulfate and SOA aerosol are fundamental components of the host CAM
119 model (and all aerosol models) and thus have been described in detail elsewhere in the
120 literature. We therefore feel it best to refer readers to this literature for detailed information
121 but include the basics in the text and plots of simulated burden of each to the SI. New text
122 at L301 in Section 2.4,

123 *“The proton dissolution scheme was dependent upon an estimated [H⁺], calculated from*
124 *the ratio of sulphate to calcite, and the simulated temperature. [...] Both the sulphate and*
125 *secondary organic carbon aerosol (Fig. S1), upon which the iron processing requires, are*
126 *fundamental components of aerosol models (e.g., Kanakidou et al., 2005; Mann et al.,*
127 *2014). In CAM sulfate is mainly formed via oxidation of SO_{2(aq)} with a smaller contribution*
128 *from H₂SO₄ condensation on aerosol while secondary organic aerosol is formed via the*
129 *partitioning of semi-volatile organic gases (Liu et al., 2012). Neither gas-to-particle*
130 *production processes are structurally modified from the description of CAM5 by Lui et al.*
131 *(2012, 2016) by the incorporation of MIMI. A structural model improvement [...]”*



132

133 **Figure S1.** Atmospheric annual mean column burden of sulfate and secondary organic
 134 aerosol for year 2007.

135

136 **Comment:** Do the authors apply modal aerosol microphysics for SO₄ and SOA size
 137 distributions, and if yes, how? Please discuss.

138 **Response:** Yes, all aerosol species undergo aerosol microphysical processes and are
 139 size resolved. But, as stated above, these aerosol species are integral components of the
 140 host aerosol model and its description is beyond this paper. We therefore briefly increase
 141 our outline of the host model (in Section 2) and refer interested readers to the detailed
 142 model description papers as follows on L147,

143 “The other major aerosol species [...] *However, atmospheric iron processing in MIMM*
 144 *requires both sulphate and (secondary) organic aerosols to be simulated as they act as*
 145 *proxies for the reactant species of [H⁺] and oxalate, respectively. In CAM5 sulphate*
 146 *aerosol is present in all three aerosol modes while secondary organic aerosol is only*
 147 *present in the fine Aitken and accumulation modes (Liu et al., 2012, 2016). Aerosol*
 148 *microphysics was applied in the same way to the new iron aerosol tracers as the base*
 149 *aerosol species (Liu et al., 2012, 2016).”*

150 **Comment:** Since, the aerosol pH range is a very important player in atmospheric iron
 151 processing, how the new parameterization compares with the previous one? Did you tune

152 the model to match the previous configuration or to observations? How much is the iron
153 dissolution production (per mode) and how does it compare to the previous model set-up
154 in total soluble Fe production terms? Moreover, how does it compare now to other
155 studies? Where is possible please provide figures.

156 **Response:** We cover aspects of this and the related next two oxalate comments within
157 Section 4.2: Iron atmospheric processing comparison. We feel it best to continue this
158 discussion there (rather than in the methods) and point the reader at the end of the pH
159 paragraph in section 2.4 as follows,

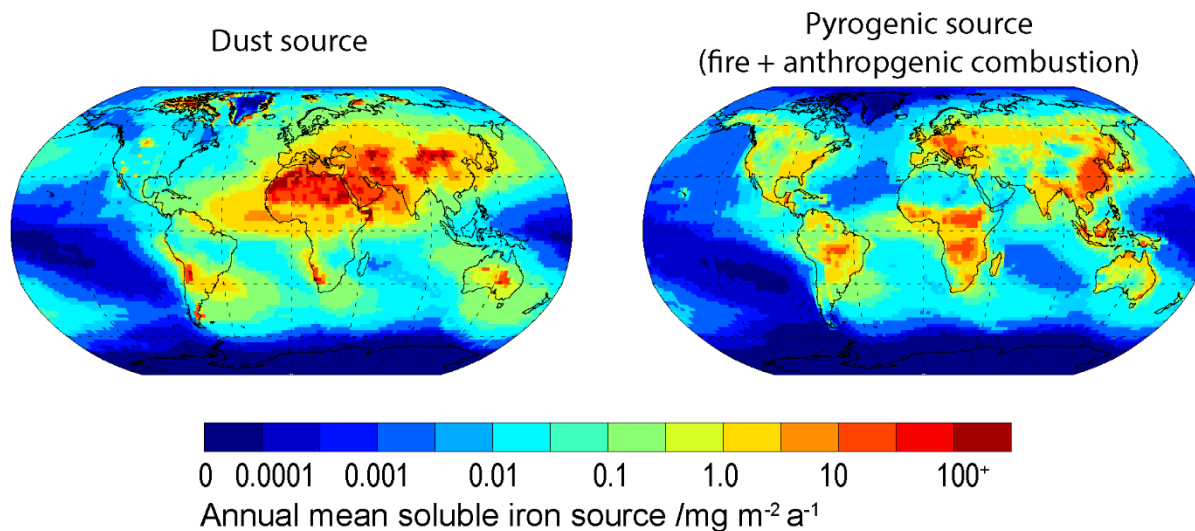
160 *“See Section 4.2 for comparison of acid processing in MIMI with literature and previous*
161 *model (BAM-Fe).”*

162 Figure 10 compares the distribution of the previous model pH with the new version and
163 is described in L631-637. During development aerosol pH was also compared to
164 published ISORROPIA II results. We added new text incorporating this missing detail as
165 follows:

166 *“Comparison of Fig 10. to modelled pH estimates by Myriokefalitakis et al. (2015) shows*
167 *generally good agreement in the NH, but in the SH MIMI simulates less acidic coarse*
168 *mode aerosol over continental regions and more acidic aerosol over marine regions. As*
169 *iron models are unable to capture the high observed iron solubility (>10%) over SH marine*
170 *regions (Myriokefalitakis et al., 2018), and in the absence of remote pH aerosol*
171 *observations, we suggest that our basic parameterization captures an aerosol pH which*
172 *is suitable for use in Earth system models.”*

173 In order to directly compare with the literature (included previous BAM-Fe results) we
174 follow (Myriokefalitakis et al., 2018) and sum iron dissolution with soluble iron emissions
175 (i.e., the net soluble iron source) to create two new maps as follows,

176



177

178 **Figure 12.** Annual mean dust and pyrogenic (sum of fires and anthropogenic
179 combustion) soluble iron source (i.e., sum of emissions and atmospheric processing).

180 New text,

181 *“Comparison of mineral dust and pyrogenic sources of modelled soluble iron (sum of*
182 *emissions and atmospheric dissolution; Fig. 12) with the four iron models (including BAM-*
183 *Fe) reported by Myriokefalitakis et al. (2018) shows that the spatial distribution in MIMI is*
184 *broadly similar for most regions of the world. A notable difference exists in the North*
185 *Pacific region where the soluble iron source in MIMI is lower than all other iron models,*
186 *and similarly with total iron concentrations when compared to observations (Figs. 4 and*
187 *5). Future development of MIMI should thus be focused on the North Pacific, including*
188 *the addition of shipping soluble iron emissions which are relatively concentrated in this*
189 *region (Ito, 2013). An improvement for MIMI can be seen over the Atlantic region directly*
190 *downwind of Saharan soluble iron sources. In general, iron models are over representing*
191 *iron solubility close to dust sources compared to observations (Myriokefalitakis et al.,*
192 *2018) and in order for BAM-Fe to reach better agreement with observed iron solubility in*
193 *this region dust emissions of soluble iron had to be scaled downwards (Conway et al.,*
194 *2019). We suggest this improvement is linked to the improved modal representation of*
195 *aerosol pH in MIMI (Fig. 10).”*

196 **Comment:** Page 12; line 323: The authors state that “in-cloud organic dissolution reaction
197 only occurs where cloud-borne aerosols are present”. Do the authors mean the SO₄ and

198 oxalate production? What other cloud-borne aerosols the model considers? Since oxalate
199 is produced in the aqueous phase of the atmosphere, in contrast to other SOA that can
200 be also produced via gas-to-particle partition, how the authors parameterized oxalate
201 production in cloud droplets? Do you take into account the cloud fraction (and/or the
202 presence of liquid water content?) in your calculations using as a proxy? Please discuss.

203 **Response:** In order to explain these issues better, we propose replacing said sentence
204 with new text as follows,

205 *“All aerosol species in the host CAM5 framework are carried in either an interstitial (i.e.,*
206 *not associated with water) or cloud-borne (i.e., associated with water) phase. The*
207 *organic-ligand reaction only proceeds within MIMI if the condition that cloud is present in*
208 *the grid-cell is first met. If cloud is present then only the iron aerosol which is associated*
209 *with water undergoes organic ligand processing (i.e., the interstitial aerosol component*
210 *remains unchanged). Any future development of MIMI within an aerosol model which*
211 *does not advect a separate tracer for the cloud-borne phase of aerosol would therefore*
212 *need to adjust the reaction to take account of this.”*

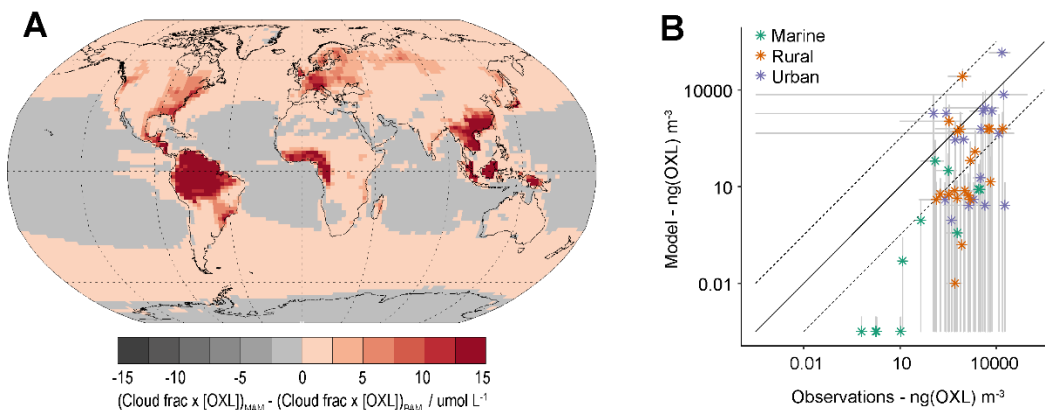
213 **Comment:** Moreover, how oxalate concentrations in the model are compared with other
214 studies and with atmospheric observations. If possible, please provide the oxalate
215 distributions of the model for the new parameterization as well as a comparison with
216 observations.

217 **Response:** Again, we first point the reader to Section 4.2 where the discussion element
218 of the changes to atmospheric dissolution of iron occurs,

219 *“See Section 4.2 for comparison of in-cloud oxalate dissolution in MIMI with literature and*
220 *previous model (BAM-Fe).”*

221 While Figure 11 already compares oxalate between MIMI and its previous version we
222 have added new panel to Figure 11 of the oxalate comparison to observation from
223 Myriokefalitakis et al. (2011) (Table S3).

224



225

226 **Figure 11: A:** Relative difference in organic ligand reaction on in-cloud iron aerosol
 227 dissolution between MIMI and BAM-Fe. Due to significant differences in simulated cloud
 228 cover between CAM4 and CAM5 oxalate concentrations [OXL] are multiplied by the
 229 model simulated cloud fraction in this figure. **B:** Surface level oxalate (OXL) concentration
 230 in the model and observations. Model values are annual mean (2007-2011) and monthly
 231 standard deviation. Observation values are from Table S3 in Myriokefalitakis et al. (2011)
 232 and reported with uncertainty where given.

233

234 And the following new text

235 *“Compared to observations (Myriokefalitakis et al., 2011) modelled oxalate*
 236 *concentrations are well represented at high observed concentrations but are biased low*
 237 *when observed concentrations are low (Fig. 11b). The low model bias is stronger within*
 238 *remote observational regions (marine vs. urban observation sites), suggesting that the*
 239 *removal of secondary organic aerosol may be too strong within the model and/or that*
 240 *there is a missing marine aerosol pre-cursor gas emissions source (Facchini et al., 2008;*
 241 *O’Dowd and de Leeuw, 2007) in this model which significantly lowers simulated*
 242 *secondary organic aerosol, and thus oxalate, concentrations.”*

243 **Comment:** Table 5: Please also provide the K(T), m and A values used for this study for
 244 each Fe-containing mineral.

246 **Response:** Added following values to table:

$$247 \quad K_{\text{med}}(T) = 1.3 \times 10^{-11} \times e^{6.7 \times 10^3 \times \left(\frac{1.0}{298.0} - \frac{1.0}{\text{temp}(K)} \right)} \text{ moles m}^2 \text{ s}^{-1}$$

$$248 \quad K_{\text{slow}}(T) = 1.8 \times 10^{-11} \times e^{9.2 \times 10^3 \times \left(\frac{1.0}{298.0} - \frac{1.0}{\text{temp}(K)} \right)} \text{ moles m}^2 \text{ s}^{-1}$$

$$249 \quad m_{\text{med}} = 0.39$$

$$250 \quad m_{\text{slow}} = 0.50$$

$$251 \quad A_{\text{med}} = 90.0 \text{ m}^2 \text{ g}^{-1}$$

$$252 \quad A_{\text{slow}} = 100.0 \text{ m}^2 \text{ g}^{-1}$$

253

254 **Comment:** Section 3.1: Please provide dust emission strengths per mode used in the
255 model (also in Table 6 as for the other species). Since it is stated that dust lifetime has
256 decreased, does this mean that the increase in dust emissions affect more the coarse
257 mode of dust? Please discuss.

258 **Response:** Added following modal emissions to text on L421 and Table 6:

$$259 \quad \text{Aiken} = 16 \text{ Tg a}^{-1}, \text{ accumulation} = 36 \text{ Tg a}^{-1}, \text{ coarse} = 3198 \text{ Tg a}^{-1}.$$

260 New text on L424:

261 “[...] because dust lifetime has proportionally decreased (Table S2) *which affects coarse*
262 *mode dust aerosol (where 98 – 99% of total dust mass is emitted) more than fine mode*
263 *dust aerosol.*”

264 **Comment:** Page 26; line 610: The authors state that emissions of dust are ~80% higher
265 and the iron it contains ~120% higher in MIMI compared to those in BAM-Fe. What is the
266 mean Fe/Dust fraction in the model after the applied corrections for the new model
267 configuration? How is it compared to other studies?

268 **Response:** We thank the Reviewer for this insightful suggestion. New text describing the
269 Fe/Dust fraction,

270 “The simulated annual mean iron in dust percentage is 4.1%, with the highest percent
271 occurring in the coarse mode at 6.5% and lowest percent occurring in the Aiken mode at
272 1.1%. Accounting for dust mineralogy therefore increases the global mean iron percent
273 by weight above the currently well-used global mean estimate of 3.5% (e.g., Jickells et
274 al., 2005; Shi et al., 2012).”

275 **Comment:** Section 4.3; lines 662-663: the authors state that although in MIMI the amount
276 of total iron deposited in the ocean is approximately double that estimated in BAM-Fe, the
277 soluble iron deposition is similar (Table 7). As a reason for this, it is indicated the reduction
278 in North Central Atlantic. Can this be also due to the different aerosol distribution
279 considered in the models (i.e., bulk vs. modal) or the differences in the iron dissolution
280 terms? Please discuss your conclusions and possibly provide a figure with relative
281 differences between the MIMI and MAM-Fe.

282 **Response:** The Reviewer is correct to point out the structural differences between bulk
283 and modal aerosol model can affect deposition (as shown by changes to dust lifetimes in
284 Table S2) as well as differences in dissolution. The atmospheric dissolution comparisons
285 are shown in Figs. 10 and 11 and the new Figure 12 suggested above further shows the
286 source of soluble iron is significantly lower than CAM4 for this region. We therefore feel
287 another figure is not necessary here. New text at L668,

288 “In MAM4 dust is treated as internally mixed aerosol with sea salt, leading to higher rates
289 of wet deposition than when dust is externally mixed aerosol (Liu et al., 2012) as it is in
290 CAM4. The internally mixed treatment of dust aerosol in MAM4 is thus an important factor
291 leading to the lower simulated dust lifetime when compared to BAM-Fe (Table S2). Over
292 the North Central Atlantic region, the combination of a lower soluble iron source (Fig. 12
293 compared to Fig. S4b by Myriokefalitakis et al. (2018)), dust atmospheric lifetime (Table
294 S2), lower aerosol pH (Fig. 10), and lower relative organic ligand processing (Fig 11) will
295 all work towards reducing the magnitude of atmospheric soluble iron deposition flux in
296 MAM4 compared to BAM-Fe.”

297 **Comment:** Table 7: Although the percent contribution from combustion iron to total iron
298 deposition after the correction in the model increases for all Northern and equatorial
299 oceanic regions for MIMI compared to BAM-Fe, that is not the case for S. Atlantic, S.

300 Pacific, S. Indian, and the Antarctic. Is this because of the increase of total iron due to the
301 increase of dust deposited aerosols? Due to the different size distribution between the
302 two versions of the model? Due to the different fire emission inventory? Or due to shipping
303 emissions?

304 **Response:** As the Reviewer suggests there are multiple reasons which could result in
305 this change. Without a series of dedicated sensitivity simulations, which are beyond this
306 study, it cannot be quantified which is dominating. We therefore include the important
307 differences that the Reviewer raises in terms of this change as follows:

308 *“The percent contribution from pyrogenic iron to total iron deposition between MIMI and*
309 *BAM-Fe is more similar for all northern and equatorial oceanic regions than southern*
310 *oceanic regions. Beyond the correction to anthropogenic combustion emissions, which*
311 *are NH dominated, could be due to differences in the emissions of both dust and fire*
312 *aerosol, structural differences between models relating to the aerosol size and*
313 *composition which alters aerosol deposition rates, or a lower soluble iron source (Fig. 12);*
314 *it is most likely to be a combination of all three.”*

315 **Comment:** In page 5, line 151: “pre-cursor” to “precursor”

316 **Response:** Changed here and also a second occurrence on L650.

317

318 **References:**

319 Aumont, O., Ethé, C., Tagliabue, A., Bopp, L. and Gehlen, M.: PISCES-v2: An ocean
320 biogeochemical model for carbon and ecosystem studies, *Geosci. Model Dev.*, 8(8),
321 2465–2513, doi:10.5194/gmd-8-2465-2015, 2015.

322 Conway, T. M., Hamilton, D. S., Shelley, R. U., Aguilar-Islas, A. M., Landing, W. M.,
323 Mahowald, N. M. and John, S. G.: Tracing and constraining anthropogenic aerosol iron
324 fluxes to the North Atlantic Ocean using iron isotopes, *Nat. Commun.*, 10(1), 1–10,
325 doi:10.1038/s41467-019-10457-w, 2019.

326 Facchini, M. C., Decesari, S., Rinaldi, M., Carbone, C., Finessi, E., Mircea, M., Fuzzi,
327 S., Moretti, F., Tagliavini, E., Ceburnis, D. and O’Dowd, C. D.: Important source of

328 marine secondary organic aerosol from biogenic amines., *Environ. Sci. Technol.*,
329 42(24), 9116–21, 2008.

330 Ito, A.: Global modeling study of potentially bioavailable iron input from shipboard
331 aerosol sources to the ocean, *Global Biogeochem. Cycles*, 27(1), 1–10,
332 doi:10.1029/2012GB004378, 2013.

333 Jickells, T. D., An, Z. S., Andersen, K. K., Baker, a R., Bergametti, G., Brooks, N., Cao,
334 J. J., Boyd, P. W., Duce, R. a, Hunter, K. a, Kawahata, H., Kubilay, N., LaRoche, J.,
335 Liss, P. S., Mahowald, N., Prospero, J. M., Ridgwell, a J., Tegen, I. and Torres, R.:
336 Global iron connections between desert dust, ocean biogeochemistry, and climate.,
337 *Science*, 308(5718), 67–71, doi:10.1126/science.1105959, 2005.

338 Kanakidou, M., Seinfeld, J. H., Pandis, S. N., Barnes, I., Dentener, F. J., Facchini, M.
339 C., Van Dingenen, R., Ervens, B., Nenes, A., Nielsen, C. J., Swietlicki, E., Putaud, J. P.,
340 Balkanski, Y., Fuzzi, S., Horth, J., Moortgat, G. K., Winterhalter, R., Myhre, C. E. L.,
341 Tsigaridis, K., Vignati, E., Stephanou, E. G. and Wilson, J.: Organic aerosol and global
342 climate modelling: a review, *Atmos. Chem. Phys.*, 5(4), 1053–1123, doi:10.5194/acp-5-
343 1053-2005, 2005.

344 Liu, X., Easter, R. C., Ghan, S. J., Zaveri, R., Rasch, P., Shi, X., Lamarque, J. F.,
345 Gettelman, A., Morrison, H., Vitt, F., Conley, A., Park, S., Neale, R., Hannay, C.,
346 Ekman, A. M. L., Hess, P., Mahowald, N., Collins, W., Iacono, M. J., Bretherton, C. S.,
347 Flanner, M. G. and Mitchell, D.: Toward a minimal representation of aerosols in climate
348 models: Description and evaluation in the Community Atmosphere Model CAM5,
349 *Geosci. Model Dev.*, 5(3), 709–739, doi:10.5194/gmd-5-709-2012, 2012.

350 Liu, X., Ma, P. L., Wang, H., Tilmes, S., Singh, B., Easter, R. C., Ghan, S. J. and Rasch,
351 P. J.: Description and evaluation of a new four-mode version of the Modal Aerosol
352 Module (MAM4) within version 5.3 of the Community Atmosphere Model, *Geosci. Model*
353 *Dev.*, 9(2), 505–522, doi:10.5194/gmd-9-505-2016, 2016.

354 Mann, G. W., Carslaw, K. S., Reddington, C. L., Pringle, K. J., Schulz, M., Asmi, A.,
355 Spracklen, D. V., Ridley, D. a., Woodhouse, M. T., Lee, L. a., Zhang, K., Ghan, S. J.,
356 Easter, R. C., Liu, X., Stier, P., Lee, Y. H., Adams, P. J., Tost, H., Lelieveld, J., Bauer,

357 S. E., Tsigaridis, K., van Noije, T. P. C., Strunk, A., Vignati, E., Bellouin, N., Dalvi, M.,
358 Johnson, C. E., Bergman, T., Kokkola, H., von Salzen, K., Yu, F., Luo, G., Petzold, A.,
359 Heintzenberg, J., Clarke, A., Ogren, J. a., Gras, J., Baltensperger, U., Kaminski, U.,
360 Jennings, S. G., O'Dowd, C. D., Harrison, R. M., Beddows, D. C. S., Kulmala, M.,
361 Viisanen, Y., Ulevicius, V., Mihalopoulos, N., Zdimal, V., Fiebig, M., Hansson, H.-C.,
362 Swietlicki, E. and Henzing, J. S.: Intercomparison and evaluation of global aerosol
363 microphysical properties among AeroCom models of a range of complexity, *Atmos.*
364 *Chem. Phys.*, 14(9), 4679–4713, doi:10.5194/acp-14-4679-2014, 2014.

365 Moore, J. K., Doney, S. C. and Lindsay, K.: Upper ocean ecosystem dynamics and iron
366 cycling in a global three-dimensional model, *Global Biogeochem. Cycles*, 18(4), 1–21,
367 doi:10.1029/2004GB002220, 2004.

368 Myriokefalitakis, S., Tsigaridis, K., Mihalopoulos, N., Sciare, J., Nenes, A., Kawamura,
369 K., Segers, A. and Kanakidou, M.: In-cloud oxalate formation in the global troposphere:
370 A 3-D modeling study, *Atmos. Chem. Phys.*, 11(12), 5761–5782, doi:10.5194/acp-11-
371 5761-2011, 2011.

372 Myriokefalitakis, S., Daskalakis, N., Mihalopoulos, N., Baker, A. R., Nenes, A. and
373 Kanakidou, M.: Changes in dissolved iron deposition to the oceans driven by human
374 activity: a 3-D global modelling study, *Biogeosciences*, 12(13), 3973–3992,
375 doi:10.5194/bg-12-3973-2015, 2015.

376 Myriokefalitakis, S., Ito, A., Kanakidou, M., Nenes, A., Krol, M. C., Mahowald, N. M.,
377 Scanza, R. A., Hamilton, D. S., Johnson, M. S., Meskhidze, N., Kok, J. F., Guieu, C.,
378 Baker, A. R., Jickells, T. D., Sarin, M. M., Bikkina, S., Shelley, R., Bowie, A., Perron, M.
379 M. G. and Duce, R. A.: Reviews and syntheses: The GESAMP atmospheric iron
380 deposition model intercomparison study, *Biogeosciences*, 15(21), 6659–6684,
381 doi:10.5194/bg-15-6659-2018, 2018.

382 O'Dowd, C. D. and de Leeuw, G.: Marine aerosol production: a review of the current
383 knowledge, *Philos. Trans. R. Soc. A Math. Phys. Eng. Sci.*, 365(1856), 1753–1774,
384 doi:10.1098/rsta.2007.2043, 2007.

385 Perlwitz, J. P., Pérez García-Pando, C. and Miller, R. L.: Predicting the mineral

386 composition of dust aerosols - Part 1: Representing key processes, *Atmos. Chem.*
387 *Phys.*, 15(20), 11593–11627, doi:10.5194/acp-15-11593-2015, 2015a.

388 Perlwitz, J. P., Pérez García-Pando, C. and Miller, R. L.: Predicting the mineral
389 composition of dust aerosols - Part 2: Model evaluation and identification of key
390 processes with observations, *Atmos. Chem. Phys.*, 15(20), 11629–11652,
391 doi:10.5194/acp-15-11629-2015, 2015b.

392 Shi, Z., Krom, M. D., Jickells, T. D., Bonneville, S., Carslaw, K. S., Mihalopoulos, N.,
393 Baker, A. R. and Benning, L. G.: Impacts on iron solubility in the mineral dust by
394 processes in the source region and the atmosphere: A review, *Aeolian Res.*, 5(May),
395 21–42, doi:10.1016/j.aeolia.2012.03.001, 2012.

396

397

398 We thank the reviewer for their thoughtful comments which have improved the
399 manuscript. New manuscript text is italicized in the replies.

400
401 **Comment:** 1. Lack of observations and sensitivity to averaging are cited as sources of
402 uncertainty in evaluating modeled soluble fraction. Is it possible that other drivers are
403 important here? For example, does the presence or absence of other chemical species,
404 or in-correct species distributions in the model, affect modeled iron solubility? In addition
405 to evaluating sensitivity to averaging techniques, it makes sense to evaluate soluble
406 fraction sensitivity to emissions of other soluble species.

407
408 **Response:** There are other factors beyond the analytical method under which iron
409 solubility is calculated causing uncertainty. We feel we have covered many of the most
410 important points in a detailed manner within L493-500 and the dedicated Future directions
411 Section 5. The undertaking of many more detailed sensitivity simulations is beyond the
412 scope of this model description paper; but this is an excellent suggestion for a follow-on
413 paper within a more relevant journal (e.g., ACP). We wish to convey the Authors
414 comments though and add the following text in opening paragraph to Section 5,

415
416 *“In general, improving the modelled representation of secondary organic aerosol*
417 *(including oxalate) and aerosol pH, particularly for remote regions, is an important task*
418 *for aerosol modeling and one which have co-benefits for iron aerosol modelling.*
419 *Comparisons of soluble fraction of other aerosol species with observations could also be*
420 *used to guide model development.”*

421
422 **Comment:** 2. The explanation of results throughout the paper would benefit from the
423 inclusion of additional quantitative information. While the figures are very comprehensive,
424 highlighting more quantitative outcomes within the text would strengthen the paper.

425
426 **Response:** We have made the manuscript more qualitative by including more information
427 from Tables and Figures within the text.

428

429 **Comment:** 3. Table 3: What is the fate of the remaining fraction of each mineral treated
430 in the model?

431

432 **Response:** The remaining mineral fractions are advected as their respective mineral
433 species. New Table 6, as suggested by R1, helps further highlight this for the reader by
434 including the number of advected tracers,

435

436 *“Table 6: Simulation time (in seconds per simulated year) for the CESM-MAM4 model.*
437 *The CAM5 base model, with the addition of dust mineralogy, and with the addition of dust*
438 *mineralogy and iron processing (i.e., MIMI v1.0) shown in black text. Cost of running the*
439 *new higher resolution CAM6 model with dust mineralogy also shown for comparison in*
440 *blue text. All CAM5 simulations executed on 10 nodes, with 36 cores per node, for two*
441 *years (2006-2007) with consistent output fields.”*

	CAM5			CAM6
	MAM4 (Base model)	MAM4DU8 (dust mineralogy)	MAM4DU8FE6 (MIMIv1.0)	MAM4DU8 (dust mineralogy)
Number advected aerosol species	24	45	63	46
Gridcell resolution (#lon x #lat)	144x96	144x96	144x96	288x192
Wall clock s a ⁻¹ (simulation)	3954	5856	7836	20167
Core-hours	396	586	784	2017

442

443

444 and we also add the following text to the header of Table 3,

445

446 *“Residual mineral dust mass is then advected as its respective tracer.”*

447

448 Note that this is covered in the main text already in L216-220 and so do not add any new
449 text to the body of the manuscript.

450

451 **Comment:** 4. Table 4: Indicate in the header that these are fire emissions ratios.

452

453 **Response:** Added at end of header.

454

455 “Modelled fire emission ratio for Fe:BC then calculated from observed ratios.”

456

457 **Comment:** 5. Line 344: Should this be statistically?

458

459 **Response:** Yes, thank you.

460

461 **Comment:** 6. Line 420, Figure 2: It would be more informative to include an additional
462 table of slopes, intercepts, etc. for each region and for all regions combined.

463

464 **Response:** As Figure 2 has limited points per region (and so regional statistics would not
465 be robust) we have included Hemispheric level details for Figure 2. However, we think
466 this an excellent suggestion for a regional scale evaluation of total iron for Figure 4.

467

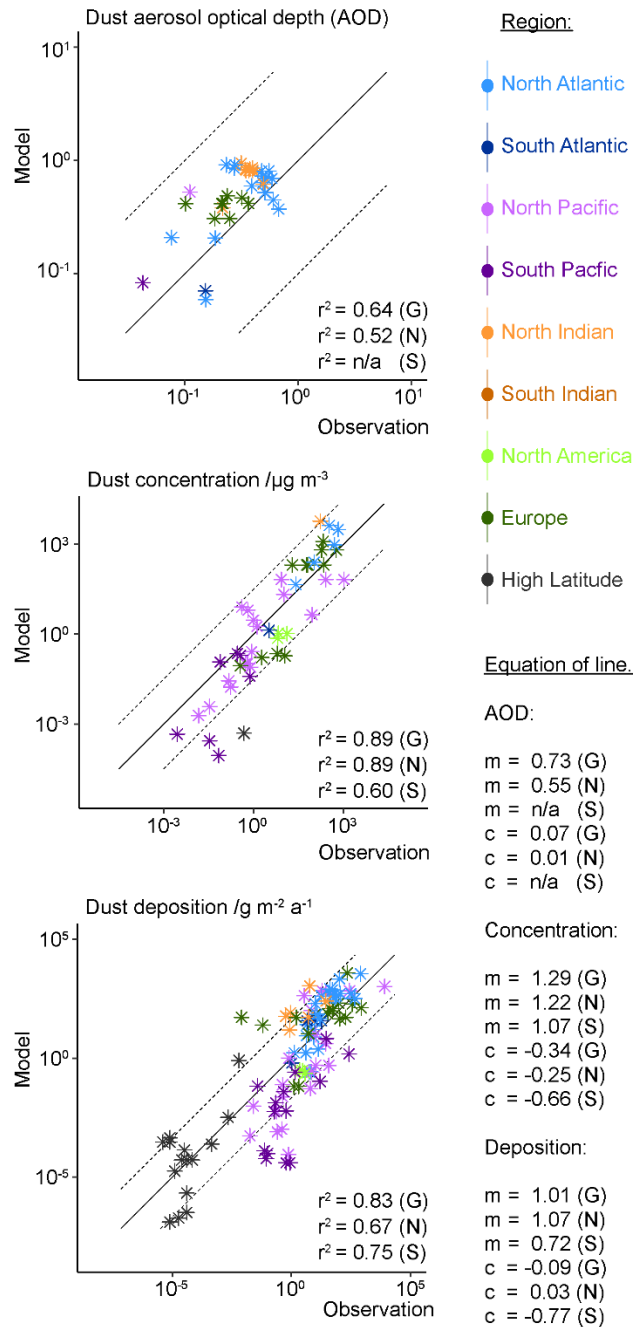
468 New text for Figure 2,

469

470 *Globally, both dust concentrations (correlation: $r^2 = 0.89$) and deposition (correlation:*
471 *$r^2 = 0.83$) are simulated well compared to observation within MIMI. A higher correlation of*
472 *modelled dust concentrations with observations is calculated in the Northern Hemisphere*
473 *(NH; $r^2 = 0.89$) compared to the Southern Hemisphere (SH; $r^2 = 0.67$), but with gradient*
474 *of line of best fit is further from 1:1 (NH: 1.22 vs. SH: 1.07). Conversely, for dust deposition*
475 *a lower correlation with observations is simulated in NH ($r^2 = 0.75$) compared to the SH*
476 *($r^2 = 0.60$) but with a gradient of the line of best fit closer to 1:1 (NH: 1.07 vs. SH: 0.72).*

477

478 Updated Figure 2:



479

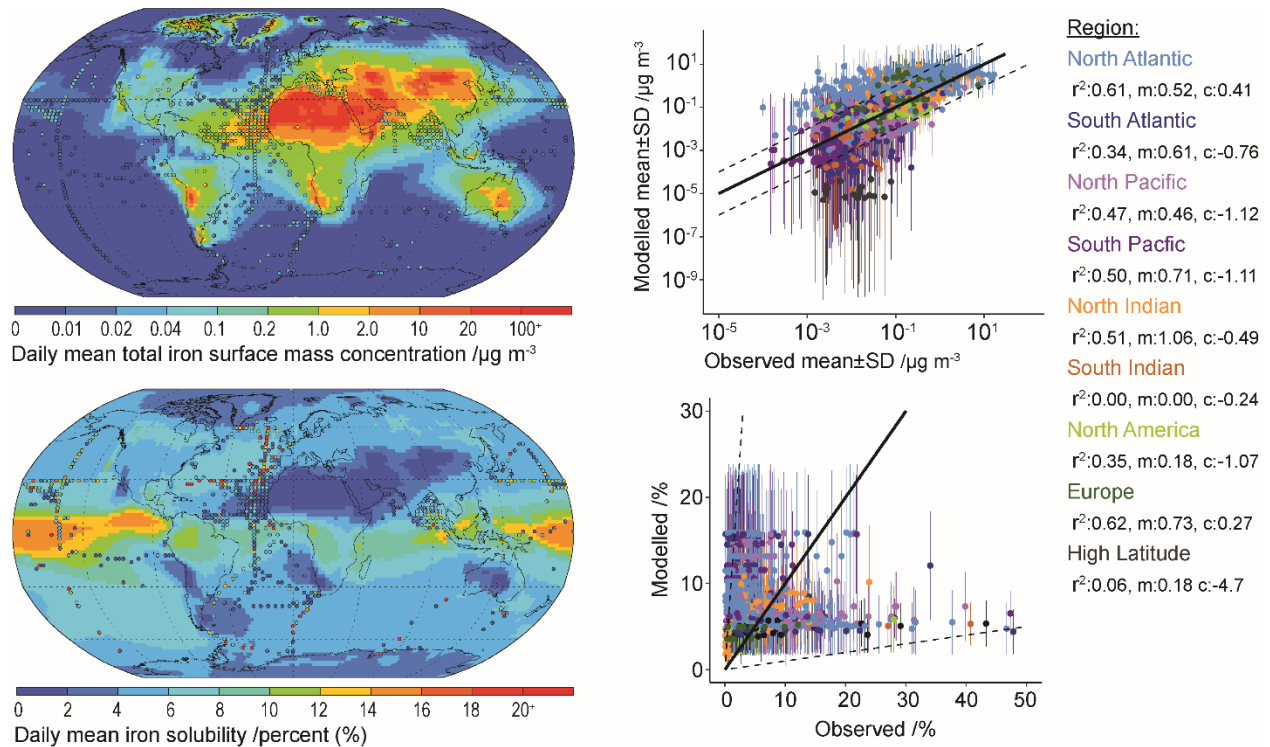
480

481 **“Figure 2.** Dust aerosol optical depth, surface concentrations and deposition in modal aerosol
 482 model and observations (Albani et al., 2014; Holben et al., 2000). *Correlation (r^2), gradient (m)*
 483 *and intercept (c) shown for global (G), Northern Hemisphere (N) and Southern Hemisphere (S)*
 484 *regions.*”

485 Updated Figure 4:

486

487



488

489

490 **Figure 4.** Daily mean model total iron concentration and solubility from 2007 to 2011.
491 Observations (circles) overlaid (at resolution of the model grid) as a mean from 1524 individual
492 records in Mahowald et al. (2009) and in Myriokefalitakis et al. (2018). Also shown are scatter
493 plots of the model mean and standard deviation compared to each available observation and
494 identified by oceanic region. *Correlation (r^2), gradient (m) and intercept (c) for total iron with*
495 *observations shown for each region.*

496

497 **Comment:** 7. Figure 4: Label the scatter plots as mean and standard deviation.

498

499 **Response:** Added (see above).

500

501 **Comment:** 8. Line 547: "...differences between method are not insignificant..."

502

503 **Response:** Altered as suggested.

504

505 **Comment:** 9. Lines 567-572: Repeated text.

506

507 **Response:** Removed repeated text.

508

509 **Comment:** 10. Lines 572-574: As written, this sentence could be interpreted as, the ratios
510 of tails only exist in certain regions. Whether narrow or wide, many distributions will have
511 tails. Perhaps rewriting the sentence to indicate that extreme ratios of tails are found in
512 specific regions would eliminate ambiguity.

513

514 **Response:** Altered sentence as suggested, now reads as,

515

516 “The *extreme* ratio of the tails of soluble and total iron are only found *in specific* regions
517 with the highest temporal variability [...]”

518

519 **Comment:** 11. Line 610: “...the iron it contains is~120% higher...”

520

521 **Response:** Altered as suggested.

522

523 **Comment:** 12. Lines 616-617: This designation of fire emissions as combustion
524 emissions here is inconsistent with the emissions categories presented in the rest of the
525 paper.

526

527 **Response:** We agree that keeping consistency throughout is important to keep the
528 reader orientated. We have removed the reference to combustion and now refer to the
529 sum of fires and anthropogenic combustion as pyrogenic iron both here and throughout
530 the manuscript where confusion could occur.

531

532 **Comment:** 13. Line 690: The first instance of acronym should be spelled out.

533

534 **Response:** Line 40 contains first instance of acronym and is spelled out.

535

536 **Comment:** 14. Lines 692-694: Was the sensitivity to vertical resolution near the surface
537 tested in this study? If not, please cite a reference here.

538

539 **Response:** It was not and to our knowledge no study in the literature has explicitly
540 examined this for dust deposition (but have for PM10 and the vertical profile). Removed
541 previous sentence and replaced with new text,

542

543 *“The dry deposition flux is sensitive to the aerosol properties, surface roughness and*
544 *modelled turbulence. Although increasing the vertical resolution has been shown to*
545 *increase surface PM₁₀ concentration (Menut et al., 2013) and better simulate the dust*
546 *vertical profile (Teixeira et al., 2016), it is not as yet clear if this would correspondingly*
547 *increase the dry deposition flux.”*

548

549 **Comment:** 15. Line 709: The first instance of acronym should be spelled out.

550

551 **Response:** This is the only instance of said acronym in the main text and so remove it
552 and just state as follows,

553

554 “Inter Tropical Convergence Zone”

555

556 **Comment:** 16. Section 5: This was by far the most well-written section of the paper. I
557 found the writing of the majority of the other sections to be choppy and difficult to read.

558

559 **Reply:** We have included many improvements to the text from both Reviewers and made
560 additional ones ourselves where we could see it would help improve the manuscript.

561

562 References:

563

564 Menut, L., Bessagnet, B., Colette, A. and Khvorostiyannov, D.: On the impact of the
565 vertical resolution on chemistry-transport modelling, Atmos. Environ., 67, 370–384,

566 doi:10.1016/j.atmosenv.2012.11.026, 2013.
567 Teixeira, J. C., Carvalho, A. C., Tuccella, P., Curci, G. and Rocha, A.: WRF-chem
568 sensitivity to vertical resolution during a saharan dust event, Phys. Chem. Earth, 94,
569 188–195, doi:10.1016/j.pce.2015.04.002, 2016.
570
571
572
573

574 **Improved methodologies for Earth system modelling of atmospheric soluble iron and**
575 **observation comparisons using the Mechanism of Intermediate complexity for Modelling**
576 **Iron (MIMI v.1.0).**

577 Douglas S. Hamilton¹, Rachel A. Scanza², Yan Feng³, Joe Guinness⁴, Jasper F. Kok⁵, Longlei
578 Li¹, Xiaohong Liu⁶, Sagar D. Rathod⁷, Jessica S. Wan¹, Mingxuan Wu⁶, and Natalie M. Mahowald¹

- 579 1. Department of Earth and Atmospheric Science, Cornell University, Ithaca, NY, USA
580 2. Atmospheric Sciences and Global Change Division, Pacific Northwest National Laboratory, Richland,
581 Washington, USA
582 3. Environmental Science Division, Argonne National Laboratory, Argonne, IL, USA
583 4. Department of Statistics and Data Science, Cornell University, Ithaca, NY, USA
584 5. Department of Atmospheric and Oceanic Sciences, University of California, Los Angeles, CA 90095, USA
585 6. Department of Atmospheric Science, University of Wyoming, Laramie, WY, USA
586 7. Department of Civil and Environmental Engineering, University of Illinois at Urbana-Champaign, Urbana, IL,
587 USA

588

589 **Abstract**

590 Herein, we present the description of the Mechanism of Intermediate complexity for Modelling
591 Iron (MIMI [v1.0](#)). This iron processing module was developed for use within Earth system models
592 and has been updated within a modal aerosol framework from the original implementation in a
593 bulk aerosol model. MIMI simulates the emission and atmospheric processing of two main
594 sources of iron in aerosol prior to deposition: mineral dust and combustion processes.
595 Atmospheric dissolution of insoluble to soluble iron is parametrized by an acidic interstitial [aerosol](#)
596 reaction and a separate in-cloud [aerosol](#) reaction scheme based on observations of enhanced
597 aerosol iron solubility in the presence of oxalate. Updates include a more comprehensive
598 treatment of combustion iron emissions, improvements to the iron dissolution scheme, and an
599 improved physical dust mobilization scheme. An extensive dataset consisting predominantly of
600 cruise-based observations was compiled to compare to the model. The annual mean modelled
601 concentration of surface-level total iron compared well with observations, but less so in the soluble
602 fraction ([iron solubility](#)) where observations are much more variable in space and time. Comparing
603 model and observational data is sensitive to the definition of the average and the temporal and
604 spatial range over which it is calculated. Through statistical analysis and examples, we show that
605 a median or log-normal distribution is preferred when comparing with soluble iron observations.
606 [Comparison of iron solubility calculated at each model time step to versus that calculated based](#)
607 [on a ratio of the monthly mean values, which is routinely presented in aerosol studies and used](#)
608 [in ocean biogeochemistry models, are on average globally one-third \(34%\) higher.](#) We redefined
609 ocean deposition regions based on dominant iron emission sources and found that the daily
610 variability in soluble iron simulated by MIMI was larger than that of previous model simulations.

611 MIMI simulated a general increase in soluble iron deposition to Southern Hemisphere oceans by
612 a factor of two to four compared with the previous version, which has implications for our
613 understanding of the ocean biogeochemistry of these predominantly iron limited ocean regions.

614

615

616 **1 Introduction**

617 Iron is an essential micronutrient for ocean primary productivity (Martin et al., 1991; Martin, 1990).
618 Iron deficiency in oceans leads to high-nutrient low-chlorophyll (HNLC) conditions under which
619 the photosynthetic productivity of phytoplankton is iron limited (Boyd et al., 2007; Jickells et al.,
620 2005), and in other regions iron may be an important nutrient for nitrogen fixation by diazotrophs
621 (Capone et al., 1997; Moore et al., 2013, 2006). Atmospheric deposition of bioavailable iron (i.e.,
622 the fraction of the total iron deposited that is readily available for ocean biota uptake) contained
623 in aerosol is an important source of new iron for the remote open ocean (Duce and Tindale, 1991;
624 Fung et al., 2000); therefore, iron impacts the ability of oceans to act as a sink of atmospheric
625 carbon dioxide (Jickells et al., 2014; Moore et al., 2013).

626 Several definitions for bioavailable iron have been proposed. The solubility of iron is considered
627 to be a key factor modulating its bioavailability (Baker et al., 2006a, 2006b); therefore, we consider
628 bioavailable iron to be the dissolved (labile) iron in either a (II) or (III) oxidation state, and we
629 define this as the soluble iron concentration throughout the manuscript. However, since most
630 aerosol iron is insoluble at emission the processing of insoluble iron to a soluble form must occur
631 during atmospheric transport. The acidic processing of iron contained in aerosol is one pathway
632 under which soluble iron can be liberated from an insoluble form with decreasing pH (Duce and
633 Tindale, 1991; Solmon et al., 2009; Zhu et al., 1997). Organic ligands, in particular oxalate, also
634 increase iron solubility by weakening or cleaving the Fe–O bonds found in iron oxide minerals via
635 complexation (Li et al., 2018; Panias et al., 1996), and in nature this reaction proceeds most
636 rapidly in a slightly acidic aqueous medium, such as cloud droplets (Cornell and Schindler, 1987;
637 Paris et al., 2011; Xu and Gao, 2008). Organic ligand processing has been estimated to increase
638 soluble iron concentrations by up to 75% more than is achievable with acid processing alone (Ito,
639 2015; Johnson and Meskhidze, 2013; Myriokefalitakis et al., 2015; Scanza et al., 2018). However,
640 there is no single mechanism that describes the observed inverse relationship of higher iron
641 solubilities with decreasing iron concentrations (Sholkovitz et al., 2012). Rather, Mahowald et al.
642 (2018) used a 1–D plume model to demonstrate that the observed trend can be explained by
643 either the differences in iron solubility at emission or the atmospheric dissolution of insoluble iron.

644 Thus, there is no observational constraint to indicate which is more likely, unless spatial
645 distribution is also considered.

646 The recent increase in efforts to model iron solubility (Ito, 2015; Ito and Xu, 2014; Johnson and
647 Meskhidze, 2013; Luo et al., 2008; Meskhidze et al., 2005; Myriokefalitakis et al., 2015; Scanza
648 et al., 2018) reflects its importance for understanding biogeochemical cycles (Andreae and
649 Crutzen, 1997; Arimoto, 2001; Jickells et al., 2005; Mahowald, 2011) and how human activity may
650 be perturbing them (Mahowald et al., 2009, 2017). However, the multi-faceted nature of how iron
651 interacts within the Earth system results in many uncertainties regarding how best to represent
652 the atmospheric iron cycle within models, which are themselves of varying complexity
653 (Myriokefalitakis et al., 2018). To incorporate the processes currently thought to be the most
654 significant (Journet et al., 2008; Meskhidze et al., 2005; Paris et al., 2011; Shi et al., 2012) and
655 improve model-to-observation comparisons of the soluble iron fraction, particularly in remote
656 ocean regions (Baker et al., 2006b; Ito, 2015; Mahowald et al., 2018; Matsui et al., 2018;
657 Sholkovitz et al., 2012), model development has been focused on refining the atmospheric iron
658 emission sources and subsequent atmospheric processing (Ito, 2015; Ito and Xu, 2014; Johnson
659 and Meskhidze, 2013; Luo et al., 2008; Meskhidze et al., 2005; Myriokefalitakis et al., 2015;
660 Scanza et al., 2018).

661 A recent multi-model evaluation of four global atmospheric iron cycle models (Myriokefalitakis et
662 al., 2018) showed that total iron deposition is over-represented close to major dust source regions
663 and under-represented in remote regions compared with observations from all four models. This
664 is consistent with previous model inter-comparisons studies that demonstrated the difficulty in
665 simultaneously simulating both atmospheric concentrations and deposition fluxes of desert dust
666 (Huneus et al., 2011). Importantly, none of the atmospheric iron processing models can capture
667 the high (>10%) solubilities measured over the Southern Ocean; this is potentially owing to the
668 model processes associated with transport and aging of aerosol iron requiring further
669 development (Ito et al., 2019). Conclusions from Myriokefalitakis et al. suggest that future model
670 improvements should focus on a more realistic aerosol size distribution and the representation of
671 mineral-to-combustion sources of iron. Most of the development of the Mechanism of Intermediate
672 Complexity for Modelling iron (MIMI), as described therein, focused on these points. First, we
673 transitioned from a bulk aerosol scheme to a two-moment modal aerosol scheme (Liu et al., 2012),
674 and second, we re-evaluated pyrogenic iron emissions from anthropogenic combustion and fires
675 combustion-iron emissions. The modal aerosol scheme was used to calculate both aerosol mass
676 and number at each time-step within an updated global aerosol microphysics model, and both

677 the [fire and anthropogenic](#) combustion emissions from Luo et al. (2008), which are likely to be
678 underestimated (Conway et al., 2019; Ito et al., 2019; Matsui et al., 2018), were improved upon.

679
680 Ocean observations of iron, and its soluble fraction, are limited both spatially and temporally owing
681 to the significant costs and logistical constraints associated with accumulating data from scientific
682 cruises. Thus, there is an inherent disparity in attempting to compare climatological means
683 calculated from temporally-chronological model results with observational means calculated from
684 temporally-limited and sporadic observations (e.g., Mahowald et al., 2008, 2009). This is
685 important because natural aerosol emissions are variable on seasonal, annual, and decadal
686 timescales, both in terms of primary natural iron emission sources (mineral dust and wildfires)
687 and the source of aerosol acidity. For example, sulphuric acid from the oxidation of dimethyl
688 sulphide and fire SO₂ (Bates et al., 1992; Chin and Jacob, 1996) have been observed to aid iron
689 dissolution when far from anthropogenic acid sources (Zhuang et al., 1992). Limitations
690 associated with the collection of continuous annual or inter-annual ship-based data across
691 multiple remote ocean regions are immutable at present, which hinders the required derivation of
692 basic statistical properties of such highly-variable data (Smith et al., 2017). Attention could
693 therefore be given to the methodologies under which such model-observation comparisons are
694 undertaken instead.

695 The present manuscript is presented in four parts. The first part (section 2) introduces updates
696 made to the Bulk Aerosol Module (BAM) iron scheme of Scanza et al. (2018) and its
697 implementation within the Modal Aerosol Module (MAM), with four modes (MAM4), within the
698 Community Earth System Model (CESM). In the second part (section 3), we compare iron
699 concentrations and the fractional solubility of iron with the observational data. Then the third part
700 (section 4) compares our updated version of the model with its predecessor. Finally, we suggest
701 further developments for atmospheric iron modelling and for comparing model results with
702 sporadic observations (section 5).

703

704

705 **2 Aerosol model**

706 The present study improves upon the previous atmospheric iron cycle module developed for the
707 Community Atmosphere Model (CAM) version 4 (CAM4) embedded in the CESM; we will refer to
708 this version as BAM-Fe (Scanza et al., 2015, 2018) therein. We incorporated the iron module
709 within the MAM framework (Liu et al., 2012, 2016) currently in the Department of Energy's Energy

710 Exascale Earth System Model (E3SM; Golaz et al., 2019) and the CAM versions 5 and 6 (CESM-
711 CAM5/6; (Neale et al., 2010)); we refer to this new version of the iron model by its name (MIMI)
712 ~~therein throughout the manuscript~~. Table 1 serves as a reference and summarizes the modifications
713 made for MIMI, which are discussed throughout the manuscript.

714 We use MAM4 with four simulated log-normal aerosol size modes: three modes (Aitken,
715 accumulation, and coarse) containing iron and a fourth primary carbonaceous mode. Table 2
716 details the new ~~combustion-pyrogenic~~ iron (i.e., from fires and anthropogenic combustion) modal
717 aerosol properties, while those of mineral dust iron follow existing dust aerosol properties (Liu et
718 al., 2012). Generally, the modelled density of iron is similar to size-resolved ambient aerosol
719 densities measured in Eastern China (Hu et al., 2012), which has significant dust and combustion
720 aerosol sources. MIMI was initially implemented and tested within a development branch of CAM
721 5.3, as per Wu et al. (2017) and Wu et al. (2018), using Cheyenne (Computational and Information
722 Systems Laboratory, 2017) and closely resembles CESM version 1.2.2. We used a 2.5° x 1.9°
723 horizontal (longitude by latitude) resolution and 56 vertical layers up to 2 hPa. Stratiform
724 microphysics followed a two-moment cloud microphysics scheme (Gettelman et al., 2010;
725 Morrison and Gettelman, 2008). The other major aerosol species black carbon (BC), organic
726 carbon, sea salt and sulphate (SO₄) were also simulated but are not explicitly examined here
727 because we are focused on ~~the~~ iron aerosol modelling. However, atmospheric iron processing in
728 MIMI requires both sulphate and (secondary) organic aerosols to be simulated as they act as
729 proxies for the reactant species of [H+] and oxalate, respectively. In CAM5 sulphate aerosol is
730 present in all three aerosol modes while secondary organic aerosol is only present in the fine
731 Aitken and accumulation modes (Liu et al., 2012, 2016). Aerosol microphysics was applied in the
732 same way to the new iron aerosol tracers as the base aerosol species (Liu et al., 2012, 2016).
733 Fire emissions were vertically distributed between six injection height ranges: 0–0.1, 0.1–0.5, 0.5–
734 1.0, 1.0–2.0, 2.0–3.0, and 3.0–6.0 km, as per AeroCom recommendations (Dentener et al., 2006).
735 Fire emissions were uniformly distributed in model levels between height limits. Unless otherwise
736 stated, aerosol and pre-cursor gas mass emissions were from the Climate Model Intercomparison
737 Program (CMIP5) inventory (Lamarque et al., 2010). Major gas-phase oxidants (O₃, OH, NO₃ and
738 HO₂) were supplied offline and were also from Lamarque et al. (2010). Meteorology (*U*, *V*, and *T*)
739 was nudged to Modern-Era Retrospective analysis for Research and Applications (MERRA) data
740 for 2006-2011. Unless otherwise stated, the last five years were used for analysis.

741

742

743 **Table 1.** Short summary of major differences between BAM-Fe and MIMI.

BAM-Fe (CAM4) Externally mixed bulk aerosol tracers with 4 size bins (0.1-1.0, 1.0-2.5, 2.5-5.0, 5.0-10.0 μm)	MIMI (CAM5) Internally mixed 2-moment aerosol tracers with 3 aerosol iron <u>size</u> modes (Aitken, accumulation, coarse)
Static soil erodibility from offline maps: DEAD (Zender et al., 2003) scheme	Time-varying soil erodibility calculated online: Kok et al. (2014a) scheme
8 dust minerals, 5 of which are iron bearing	No change
Static Luo et al. combustion iron emissions	Static Luo et al. combustion iron emissions x5
Static Luo et al. fire iron emissions	Time-varying Fe:BC fire iron emission ratio
Surface fire iron emissions	Vertically distributed fire iron emissions
Static aerosol pH across aerosol size <u>bins</u>	Aerosol pH size dependent
Assumed oxalate concentration based on primary organic carbon	Assumed oxalate concentration based on secondary organic carbon
In-cloud aerosol concentrations based on simulated cloud fraction	Separate in-cloud and interstitial aerosol tracers

744

745

746 The model used in this study performed well when compared to observations from a variety of
747 different environments, and produced aerosol concentrations that were close to those of the multi-
748 model mean of similarly complex aerosol models (Fanourgakis et al., 2019).

749

750 **Table 2.** Combustion iron aerosol size and number properties.

Mode	Number mode diameter, D_{gn} (μm)	Geometric standard deviation (σ)	Volume mean particle diameter, D_{emit} (μm) ¹	Density, ρ (kg/m^3)
Aitken	0.03 ^a	1.8 ^a	0.0504	1500 ^c
Accumulation	0.08 ^a	1.8 ^a	0.134	1500 ^c
Coarse	1.00 ^b	2.0 ^b	2.06	2600 ^c

751 1. $D_{emit} = D_{gn} \times \exp(1.5 \times (\ln(\sigma))^2)$

752 a. Liu et al. (2012)

753 b. Dentener et al. (2006) and Liu et al. (2012)

754 c. Wang et al. (2015)

755

756

757 **2.1 Dust aerosol modelling**

758 ~~Desert-Mineral~~ dust aerosol was modelled via the Dust Entrainment And Deposition model
759 (DEAD; Zender et al., 2003), which was previously updated to include the brittle fragmentation
760 theory of vertical dust flux (Kok, 2011) on mineral size fractions (Albani et al., 2014; Scanza et al.,
761 2015). We further improved the emissions of dust in MAM to follow a physically-based vertical
762 flux theory (Kok et al., 2014a), which has been shown to significantly improve dust emissions (Kok
763 et al., 2014b). Notice that this method allowed for the removal of the soil erodibility map approach
764 previously employed by the DEAD scheme (Table 1), and still provided more accurate simulations
765 of regional dust emissions and concentration (Kok et al., 2014b). Dust aerosol optical depth (AOD)
766 was calculated using mineralogy-based radiation interactions as described by Scanza et al.
767 (2015). Dust emissions were tuned such that a global annual mean dust AOD of ~0.03 was
768 attained, as recommended by Ridley et al. (2016) and matching values in Scanza et al. (2015) for
769 a similar model configuration.

770 Dust mineralogy in MIMI is designed to be comprised of eight separate transported tracers: illite,
771 kaolinite, montmorillonite, hematite, quartz, calcite, feldspar and gypsum (Scanza et al., 2015).
772 Mineral soil distributions were supplied offline (Claquin et al., 1999) with the emission of each dust
773 mineral species further refined following the brittle fragmentation theory (Scanza et al., 2015).

774

775 **2.2 Iron aerosol modelling**

776 The simulated lifecycle of iron can be grouped into three main stages: (1) iron emission to
777 atmosphere, (2) physical-chemical iron processing during transport and (3) final iron deposition
778 and, thus, loss from the atmosphere. In the following sections, we describe the emissions and
779 subsequent atmospheric dissolution of iron (stages 1 and 2), while the effects of this on the
780 magnitude of oceanic soluble iron deposition (stage 3) in MIMI are examined and compared to
781 BAM-Fe in section 4.

782 Iron optical properties are currently considered to reflect those of hematite because this mineral
783 contains 97% of the iron aerosol mass fraction (see section 2.3.1).

784

785

786

787 2.3 Iron aerosol emissions

788 MIMI contains three major iron emission sources: mineral dust, fires (defined here as the sum of
789 wildfires and human-mediated biomass burning) and anthropogenic combustion (defined here as
790 the sum of industrial and domestic biofuel burning). In the BAM-Fe version of the model, fire and
791 anthropogenic combustion emissions were combined into a single static monthly mean value. In
792 MIMI, fire emissions of iron were updated to be distinct from other combustion-pyrogenic iron
793 sources and were parametrized to track the BC emissions from fires using an Fe:BC ratio. Fire
794 BC emissions were simulated to be time varying on a monthly scale, resulting in a much more
795 pronounced seasonality to fire emissions (e.g., Giglio et al., 2013) compared to BAM-Fe where
796 seasonality was not imposed.

797 For all iron species in each mode, the aerosol number emissions ($Fe_{emit,num}$) were calculated from
798 the mass emissions within the same mode ($Fe_{emit,mass}$) using the properties in Table 2 and
799 following Liu et al. (2012),

$$Fe_{emit,num} = \frac{Fe_{emit,mass}}{\left(\frac{\pi}{6}\right) \times \rho \times D_{emit}^3} \quad \text{Equation 1}$$

800

801 2.3.1 Iron emissions within mineral dust aerosol

802 Based on previous research by Journet et al. (2008) and Ito and Xu (2014), the iron fraction in
803 each mineral species was prescribed at emission as follows: 57.5% in hematite, 11% in smectite,
804 4% in illite, 0.24% in kaolinite, 0.34% in feldspar, and 0% in the remaining three mineral species
805 (Table 3); which has been shown to improve the accuracy of the modelled total iron fraction
806 estimated from mineral dust (Scanza et al., 2018; Zhang et al., 2015). The mass of each of the
807 eight mineral dust species advected at each model time step was the residual mineral mass (i.e.,
808 after the removal of the iron mass), such that the sum of all eight minerals and the total iron from
809 mineral dust equalled unity, and hence, the original total singular dust mass emitted from the land
810 surface.

811 Iron emissions from the five iron-bearing mineral dust species (three dust minerals contain no
812 iron) were then partitioned into the four advected mineral-dust-bearing iron aerosol tracers (Table
813 3); iron tracers were defined as being (in)soluble and by the speed of the atmospheric reaction
814 rate acting on them: slow or medium (Scanza et al., 2018). Note that, slow- and med-soluble iron
815 are only produced by non-reversible atmospheric processing within the model: therefore,

816 computational costs can be reduced by not creating a separate iron tracer representing the
 817 fraction which is already soluble at emission (i.e., ‘fast’ reacting), but instead add an initial med-
 818 soluble iron processed emission burden which is equivalent to the assumed fast reacting iron
 819 fraction.

820

821 **Table 3.** Mass fraction of iron in each simulated iron bearing dust mineral species and allocation
 822 to each mineral iron tracer at emission. At emission med-soluble iron is equivalent to the fast-
 823 soluble iron fraction (i.e., the fraction which is already assumed to be soluble at emission).
 824 Residual mineral dust mass is then advected as its respective tracer.

Mineral dust mass percent allocated to each dust iron tracer at emission

Mineral	Med-soluble	Med-insoluble	Slow-soluble	Slow-insoluble	Total
Hematite	0.0%	0.0%	0.0%	57.5%	57.5%
Smectite	0.55%	10.45%	0.0%	0.0%	11.0%
Illite	0.11%	3.89%	0.0%	0.0%	4.0%
Kaolinite	0.01%	0.0%	0.0%	0.23%	0.24%
Feldspar	0.01%	0.0%	0.0%	0.33%	0.34%

825

826

827 2.3.2 Iron aerosol emissions from fires

828 Following Luo et al. (2008), we used observed Fe:BC mass ratios to estimate fine and coarse
 829 mode iron emissions from fires. An additional difference between BAM (CAM4) and MAM (CAM5)
 830 models is the emission dataset used to estimate global fire emissions of aerosol and trace gases.
 831 The BAM model uses adjusted AeroCom fire emissions (Dentener et al., 2006; Scanza et al.,
 832 2018), while MAM uses CMIP5 fire emissions (Lamarque et al., 2010). Base fire BC emissions
 833 within the CMIP5 database are 2.55 Tg a⁻¹ BC; however, the scaling of emissions from fires has
 834 been shown to be necessary to improve model to observed (aerosol optical depth and particulate
 835 matter) BC ratios (Reddington et al., 2016; Ward et al., 2012). Therefore, we globally scaled the
 836 fire iron emissions by a uniform factor of two, which is comparable with the overall lower scaling
 837 factor from a review of the literature by Reddington et al. (2016: Table 2). Fine mode iron
 838 emissions from fires were then segregated to assign 10% of the fine sized mode-mass to the
 839 Aitken mode, with the remaining 90% assigned to the accumulation mode.

840
841
842
843
844
845

Table 4. Measured iron (Fe) and black carbon (BC) values (various units; as only the Fe:BC ratio is required they are not included) and the Fe/BC ratio. Calculated with three decimal places, ratio reported to one significant figure to reflect high uncertainty. [Modelled fire emission ratio for Fe:BC then calculated from observed ratios.](#)

Biome	Reference	Fe	BC	Fe/BC
Cerrado	Yamasoe et al. (2000)	0.08	12.6	0.006
	Yamasoe et al. (2000)	0.05	6.5	0.008
	Ward et al. (1991)	0.9	3.3	0.273
Mean Fe:BC ratio = 0.1				
Temperate	Ward et al. (1991)	0.1	5.0	0.020
	Mean Fe:BC ratio = 0.02			
Tropical	Luo et al. (2008)	-	-	0.020
	Artaxo et al. (2013)	179	2801	0.639
	Artaxo et al. (2013)	27	405	0.067
	Artaxo et al. (2013)	20	98	0.204
	Artaxo et al. (2013)	12	235	0.051
	Ward et al. (1991)	0.9	10	0.090
	Yamasoe et al. (2000)	0.03	7.3	0.004
	Yamasoe et al. (2000)	0.05	3.9	0.013
Mean Fe:BC ratio = 0.06				
Global	Mean Fe:BC ratio = 0.06			

846
847

848 Luo et al. (2008) used a single Amazonian observational dataset in their study to determine the
849 flux of iron [aerosol](#) from fires (Fe:BC). We extended this to incorporate other Amazonian fire
850 (Fe:BC) data and, importantly, non-Amazonian biome fire (Fe:BC) data, which are likely to have
851 different combustion properties, and hence iron emissions (e.g., Akagi et al., 2011). From Table
852 4, we suggest that after adding 11 more data inventory values, Luo et al. likely under-represented
853 the global fine mode Fe:BC ratio at 0.02. We instead used the global mean Fe:BC ratio from the
854 additional data of 0.06. Conversely, Luo et al. likely over-represented the coarse mode Fe/BC
855 ratio at 1.4. By including additional observational information from Artaxo et al. (2013) we reduced

856 this to 1.0. Using size-segregated wet season (i.e., representing a locally-transported emission
857 source) observation data from Artaxo et al. (2013), we estimated that the amount of BC mass in
858 the coarse mode was 37% of fine mode mass. Overall this doubles the fractional contribution of
859 fine mode (BAM: 0.1–1 μ m size bin, MAM: sum of Aitken and accumulation modes) iron emissions
860 from fires (BAM-Fe: fine = 7% of total mass, MIMI: fine = 14% of total mass).

861 Using the soluble Fe:BC ratio of 0.02 reported in Luo et al. (2008) resulted in 33% solubility of
862 fine mode iron from fires at emission, which is lower than the 46% reported in Oakes et al. (2012)
863 and higher than the 12% reported in Ito (2013). As few data exist in the literature pertaining to
864 coarse mode BC, or more importantly its ratio to iron, we retained the 4% solubility of iron in the
865 coarse mode at emission, as suggested by Luo et al.

866 Total iron emissions from fires in MIMI were 2.2 Tg Fe a^{-1} (Aitken: 0.02 Tg a^{-1} , accumulation: 0.28
867 Tg a^{-1} , coarse: 1.9 Tg a^{-1}), representing an approximate increase in iron emissions from fires of
868 around 25% compared with those from BAM-Fe, with most of the mass (86%) still in the coarse
869 mode. The lower 25% increase between BAM-Fe and MIMI iron emissions, as compared to the
870 doubling of the fire iron emissions themselves within MIMI, is due to different underlying fire
871 emission inventories used in each model. Aerosol number concentrations were then calculated
872 using Equation 1 and the physical properties listed in Table 2. We adopted the methodology of
873 Wang et al. (2015) by assuming that the density of iron aerosol from fires (and anthropogenic
874 combustion) in the Aitken and accumulation modes matches that of BC, while in the coarse mode
875 matches that of mineral dust. The vertical distribution of iron emissions from fires were also
876 updated in MIMI (BAM-Fe emitted all iron from fires at the surface) to account for pyro-convection,
877 which lofts aerosol to higher altitudes at the point of emission within the model (Rémy et al., 2017;
878 Sofiev et al., 2012; Wagner et al., 2018).

879

880 **2.3.3 Iron emissions from anthropogenic combustion sources**

881 Separate lines of evidence (Conway et al., 2019; Ito et al., 2019; Matsui et al., 2018) have shown
882 that anthropogenic industrial iron emissions are highly likely to be larger than previously estimated
883 (e.g., Ito, 2015; Luo et al., 2008; Myriokefalitakis et al., 2018a). Therefore, anthropogenic
884 combustion emissions of iron in MIMI were the same as those in BAM-Fe, as first reported by Luo
885 et al. (2008), uniformly multiplied by a factor of five to bring into closer agreement with
886 observations of industrial magnetite emissions in line with Matsui et al. (2018). Resulting fine
887 mode anthropogenic combustion emissions were 0.50 Tg Fe a^{-1} and coarse mode emissions were

888 2.8 Tg Fe a⁻¹. Similar to fire emissions, 10% of fine size emissions were partitioned into the Aiken
889 mode at emission, the remainder 90% of fine size emissions were emitted into the accumulation
890 mode, and 100% of coarse size emissions were emitted to the coarse mode. We retain the Luo
891 et al. (2008) estimate of 4% combustion iron solubility at emission (Chuang et al., 2005).
892 Calculations of aerosol number concentrations of combustion iron followed the same procedure
893 as described for fire emissions in the previous Section 2.3.2.

894

895 **2.4 Atmospheric iron aerosol processing**

896 2.4.1 Acid and organic ligand processing

897 Once airborne, iron undergoes a series of physical and chemical processing steps within the
898 atmosphere, each working to alter the soluble iron fraction (i.e., its solubility). The MIMI
899 atmospheric iron dissolution scheme is summarized-presented in Table 5, with a full description
900 reported previously by Scanza et al. (2018). Within each of the three iron-bearing aerosol size
901 modes, six tracers of iron were advected within the model: medium-insoluble and medium-soluble
902 mineral dust iron (containing both readily-released and medium-reactive mineral dust iron
903 (Scanza et al., 2018)), slow-insoluble and slow-soluble mineral dust iron, and insoluble and
904 soluble pyrogenic (sum of fires and anthropogenic combustion) iron which was (assumed to be
905 medium-reactive (Scanza et al., 2018)). Both proton and organic ligand promoted iron dissolution
906 mechanisms were modelled. The proton promoted dissolution scheme was dependent upon an
907 estimated [H⁺], calculated from the ratio of sulphate to calcite, and the simulated temperature.
908 Organic ligand dissolution was dependent upon the simulated organic carbon concentration as
909 oxalate (the main reactant) itself was not modelled. Both the sulphate and secondary organic
910 carbon aerosol (Fig. S1), upon which the iron processing requires, are fundamental components
911 of aerosol models (e.g., Kanakidou et al., 2005; Mann et al., 2014). In CAM sulphate is mainly
912 formed via oxidation of SO_{2(aq)} with a smaller contribution from H₂SO₄ condensation on aerosol
913 while secondary organic aerosol is formed via the partitioning of semi-volatile organic gases (Liu
914 et al., 2012). Neither gas-to-particle production processes are structurally modified from the
915 description of CAM5 by Lui et al. (2012, 2016) by the incorporation of MIMI. A structural model
916 improvement was that MAM (CAM5) advected separate tracers for the interstitial and cloud-borne
917 aerosol phases, and so the proton and organic ligand promoted dissolution reactions were applied
918 to each aerosol tracer phase, respectively.

919 Dust aerosol moving through areas containing acidic gases, with a pH 1–2, increases the solubility
920 of the iron contained within it (Ingall et al., 2018; Longo et al., 2016; Meskhidze et al., 2003;
921 Solmon et al., 2009); with mineralogy being a key factor determining the rate of dissolution at a
922 given pH (Journet et al., 2008; Scanza et al., 2018). Modelled aerosol pH in MIMI was
923 parametrised to depend only on the ratio of the calcium to sulphate aerosol concentration (Scanza
924 et al., 2018). At each time step, if $[SO_4] > [Calcite]$, then the aerosol was assumed to be acidic
925 with a low pH, while if $[SO_4] < [Calcite]$, then aerosol was assumed to be well buffered (Böke et
926 al., 1999) and the pH = 7.5. In MIMI, we updated the pH calculation from BAM-Fe two-fold: (1) In
927 BAM-Fe, pH was calculated as the mean across all four size bins (0.1–10 μm), while in MIMI, pH
928 was calculated separately for each interstitial aerosol size mode. (2) Aerosol measurements of
929 pH have shown that interstitial aerosol is likely to be more acidic than was assumed in BAM-Fe
930 (Longo et al., 2016; Weber et al., 2016), even when taking into account declining sulphate levels
931 (Weber et al., 2016); therefore, we have lowered the aerosol pH to 1 (from 2) in both the Aitken
932 and accumulation modes where sulphate aerosol dominates. However, in the coarse mode,
933 where dust dominates, we retained the lower pH boundary of 2. Furthermore, MAM aerosol was
934 simulated as an internally mixed aerosol; therefore, the $SO_4:Ca$ ratio included the mixing of these
935 aerosol components within each mode. [See Section 4.2 for comparison of acid processing in](#)
936 [MIMI with literature and previous model \(BAM-Fe\).](#)

937 All aerosol species in the host CAM5 framework are carried in either an interstitial (i.e., not
938 associated with water) or cloud-borne (i.e., associated with water) phase. The organic-ligand
939 reaction only proceeds within MIMI if the condition that cloud is present in the grid-cell is first met.
940 If cloud is present then only the iron aerosol which is associated with water undergoes organic
941 ligand processing (i.e., the interstitial aerosol component remains unchanged). Any future
942 development of MIMI within an aerosol model which does not advect a separate tracer for the
943 cloud-borne phase of aerosol would therefore need to adjust the reaction to take account of this.

944 An assumed oxalate concentration in MIMI was estimated based on the modelled organic carbon
945 concentration and could not exceed a maximum concentration threshold of 15 $\mu\text{mol/L}$ (Scanza et
946 al., 2018). In BAM-Fe, oxalate was derived from the sum of both the primary and secondary
947 organic carbon aerosol concentrations, while in MIMI this was updated to be dependent only upon
948 the secondary organic carbon source because oxalate is itself a product of the oxidation of volatile
949 organic carbon gases (Myriokefalitakis et al., 2011). An additional term was added to the reaction
950 mechanism to account for the small amount of organic ligand processing proceeding by species
951 other than oxalate (Scanza et al., 2018). [See Section 4.2 for comparison of in-cloud organic](#)
952 [dissolution in MIMI with literature and previous model \(BAM-Fe\).](#)

953 **Table 5.** Summary of atmospheric processing reaction equations from Scanza et al. (2018). Here
 954 / represents either medium or slow reacting iron aerosol (combustion iron is modelled as medium).
 955 The pH calculation is updated to be calculated within each mode and oxalate ($C_2O_4^{2-}$)
 956 concentrations are calculated based only on the secondary organic aerosol (SOA) concentrations.

	Reaction equation	Reaction rate constituents
Acid processing of aerosol		$RFe_{l,acid} = K_l(T) \times a(H^+)^{m_l} \times f(\nabla G_r) \times A_l \times MW_l$
		$K_l(T) \text{ is the temperature dependent rate coefficient (moles } m^{-2} s^{-1})$
		$K_{med}(T) = 1.3 \times 10^{-11} \times e^{6.7 \times 10^3 \times (\frac{1.0}{298.0} - \frac{1.0}{temp(K)})}$
	Equation 2:	$K_{slow}(T) = 1.8 \times 10^{-11} \times e^{9.2 \times 10^3 \times (\frac{1.0}{298.0} - \frac{1.0}{temp(K)})}$
	$\frac{d}{dt}[Fe_{soluble}] = RFe_{i,acid} \times [Fe_{insoluble}]$	$a(H^+) \text{ is the proton concentration, with an empirical reaction order } m_l$ $m_{med} = 0.39; m_{slow} = 0.50$
		$\text{If } [SO_4] > [Calcite] \text{ then } pH = 1 \text{ in Aitken and accumulation modes or 2 in coarse.}$ $\text{Else } pH = 7.5.$
		$f(\nabla G_r) \text{ accounts for dissolution rate change with variation from equilibrium (equals 1 for simplicity (Luo et al., 2008))}$
		$A_l \text{ is the specific surface area (} m^2 g^{-1} \text{)}$ $MW_l \text{ is the molecular weight (} g mol^{-1} \text{)}$ $A_{med} = 90.0 m^2 g^{-1}; A_{slow} = 100.0 m^2 g^{-1}$
Organic ligand processing		$RFe_{l,oxal} = a_l \times [C_2O_4^{2-}] + b_l$
	Equation 4:	$\text{If } l = \text{medium (or combustion) iron:}$ $a = 2.3 \times 10^{-7} \mu M^{-1} s^{-1}; b = 4.8 \times 10^{-7} s^{-1}$
	$\frac{d}{dt}[Fe_{soluble}] = RFe_{i,oxal} \times [Fe_{insoluble}]$	$\text{If } l = \text{slow iron:}$ $a = 9.5 \times 10^{-9} \mu M^{-1} s^{-1}; b = 3.0 \times 10^{-8} s^{-1}$
	Equation 5:	$\text{For longitude}(i), \text{latitude}(j) \text{ and level}(k):$
	$\frac{d}{dt}[Fe_{insoluble}] = -\left(\frac{d}{dt}[Fe_{soluble}]\right)$	$[C_2O_4^{2-}]_{i,j,k} = 150 \times \frac{[SOA_{i,j,k}]}{\max[SOA]}$

957 **2.4.2 Computational costs**

958 Earth System models are generally characterized by having a heavy computational burden in
 959 simulating atmospheric processes. The inclusion of MIMI requires eight dust mineral tracers (a
 960 net addition of seven) and six iron tracers. The total addition of aerosol tracers new is 39 (13 in
 961 each of the three aerosol modes) if dust minerology is not already present, or 18 new aerosol
 962 tracers if it is (e.g., NASA GISS model (Perlwitz et al., 2015a, 2015b)). The additional
 963 computational cost of MIMI within CESM-CAM5 is approximately a doubling of the required core-
 964 hours; around half of that is associated with dust minerology speciation and the other half with
 965 iron speciation and processing (Table 6). Note that additional computational tuning, or changes
 966 in configuration, could modify these computational change estimates. For example, with dust
 967 minerology (MAM4DU8) there is an approximate 3-fold increase in required core-hours due to
 968 model structural differences when transitioning from CAM5 to CAM6.

970 Table 6: Simulation time (in seconds per simulated year) for the CESM-MAM4 model. The CAM5
 971 base model, with the addition of dust minerology, and with the addition of dust minerology and
 972 iron processing (i.e., MIMI v1.0) shown in black text. Cost of running the new higher resolution
 973 CAM6 model with dust minerology also shown for comparison in blue text. All CAM5 simulations
 974 executed on 10 nodes, with 36 cores per node, for two years (2006-2007) with consistent output
 975 fields.

	CAM5			CAM6
	MAM4 (Base model)	MAM4DU8 (dust minerology)	MAM4DU8FE6 (MIMIV1.0)	MAM4DU8 (dust minerology)
Number advected aerosol species	24	45	63	46
Gridcell resolution (#lon x #lat)	144x96	144x96	144x96	288x192
Wall clock s a ⁻¹ (simulation)	3954	5856	7836	20167
Core-hours	396	586	784	2017

979 **2.5 Observation and model iron calculations**

980 **2.5.1 Spatially aggregating limited observations**

981 The observations of total iron concentrations and the fractional solubility of iron used in this study
982 are the joint totals (1524 records) of those reported in Mahowald et al. (2009) and Myriokefalitakis
983 et al. (2018). However, many of these observations represent averages of only one or a few days
984 of iron and soluble iron measurements, and thus can be difficult to compare against annual, or
985 longer, mean time periods calculated within the model. Furthermore, building empirical
986 distributions of iron properties from observations requires a larger sample size than currently
987 available in many regions. We therefore tested how aggregating the observations spatially,
988 sometimes termed ‘super-obbing’, altered our model evaluation. Our objective was to capture the
989 small regional scale properties of iron, and not those at a point source; therefore, we assume that
990 the benefits gained by aggregating in this way, to help produce a statically-statistically useful
991 amount of observations, outweighs any potential biases.

992 **2.5.2 Variations in model temporal averaging**

993 The model was run at a 30-minute time resolution. At each 30-minute time_step, soluble iron, total
994 iron, and the ratio of soluble to total iron (iron solubility) were computed. The model output was
995 S_i (daily mean soluble iron concentration on day i), T_i (daily mean total iron concentration on day
996 i), and R_i (daily mean iron solubility on day i). Note that R_i is the daily mean of the calculated 30-
997 minute solubilities and hence is not equal to S_i / T_i . We define online solubility as the average-of-
998 ratios and was calculated as follows:

$$\left(\sum_{i=1}^n R_i \right) / n \quad \text{Equation 6}$$

999

1000 where n represents the total number of records over which the average was calculated. Online
1001 solubility is reported throughout this study. In Section 3.4, we then compare the average-of-ratios
1002 to the ratio-of-averages (defined as offline solubility), calculated as follows:

1003

$$\frac{(\sum_{i=1}^n S_i) / n}{(\sum_{i=1}^n T_i) / n} = \frac{\bar{S}}{\bar{T}} \quad \text{Equation 7}$$

1004

1005 where \bar{S} and \bar{T} are the grid cell averages of soluble and total iron concentrations, respectively,
 1006 over the total time period considered in this study (2007 to 2011). While Equation 7 is common
 1007 within the literature, this methodology can produce larger variability in iron solubility across grid
 1008 cells because it is based on both soluble and total iron annual mean concentrations. In the online
 1009 method, variability is reduced as extreme values in soluble and total iron concentrations generally
 1010 do not occur at the same time. We can define the occurrence of extreme values, with respect to
 1011 the time frame considered, by analysing a relative Z-score metric, calculated as follows:

$$Z_{Fe,t} = \frac{(Fe_t - \overline{Fe_t})}{\sigma Fe_t} \quad \text{or} \quad Z_{Fe,s} = \frac{(Fe_s - \overline{Fe_s})}{\sigma Fe_s} \quad \text{Equation 8}$$

1012
 1013
 1014 where Fe is either total (Fe_t) or soluble (Fe_s) iron. The relative normalized Z-score can then be
 1015 calculated as follows:

$$\sum_{i=1}^n (z_{t,i} - z_{s,i}) / z_{t,i} \quad \text{Equation 9}$$

1016
 1017 where $Z_{t,i}$ and $Z_{s,i}$ are the Z-scores of total and soluble iron concentrations, respectively, at each
 1018 grid cell for each time step i . The Z-score metric provides a relative direction and distance of an
 1019 instantaneous value with respect to its mean. The Z-score is reported in multiples of the standard
 1020 deviation (Equation 8); therefore, a Z-score of zero indicates that the data point value is identical
 1021 to the mean value. To assess the relative difference in the variability, at a given time, between
 1022 the modelled total and soluble iron concentration and its mean we calculated the difference in Z-
 1023 scores between total and soluble iron concentrations and normalized it using the Z-score of total
 1024 iron concentration (Equation 9). Note that the Z-score of the soluble iron concentration could also
 1025 be used to normalise the difference. This method allows for the examination of how the
 1026 occurrence of extreme concentration values in total and soluble iron influences the method of
 1027 solubility calculation (Equation 6 vs. Equation 7).

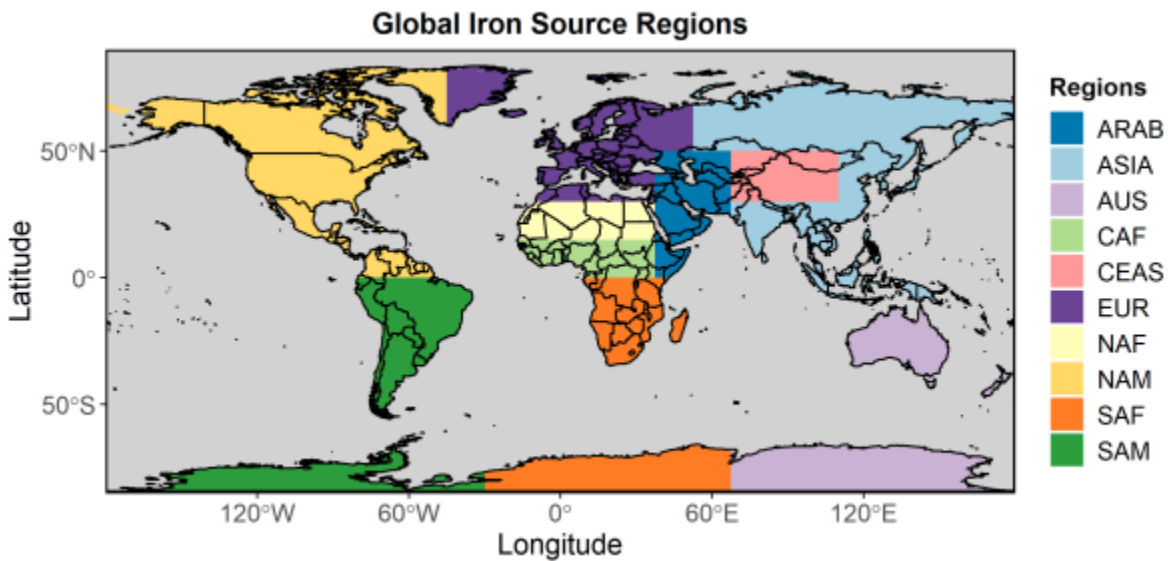
1028
 1029 **2.6 Iron ocean deposition source apportionment**

1030 An ocean deposition source apportionment sub-study was designed to classify ocean deposition
 1031 regions according to the dominant atmospheric soluble iron sources, rather than ocean basins

1032 defined from a more traditional physical oceanographic viewpoint (e.g., Gregg et al., 2003). By
1033 incorporating recent model estimates for dust and the importance of combustion-pyrogenic iron
1034 emissions (Luo et al., 2008; Matsui et al., 2018) the seven large-scale source regions defined in
1035 Mahowald et al. (2008) were modified slightly to separate the major dust iron source regions from
1036 fire and anthropogenic combustion iron source regions. This resulted in a total of 10 iron emission
1037 source regions (Fig. 1; see also Table S1 for details).

1038 Simulations in the source apportionment study used BAM-Fe, as described in Scanza et al. (2018)
1039 with slight modification. Briefly, anthropogenic combustion iron emissions were increased by a
1040 uniform factor of five, and iron from fires followed the updated Fe:BC ratio (Table 4) and seasonal
1041 variability in the fire BC emissions; all as per MIMI. Aerosols were externally mixed in BAM, and
1042 therefore altering the regional aerosol loading did not affect aerosol transport or deposition in the
1043 more significant way it could in MAM, in which aerosol are internally mixed. This information was
1044 then used in Section 4.3.1 to compare the differences in daily mean deposition of soluble iron
1045 between the BAM-Fe and MIMI models within each defined ocean region.

1046



1047

1048 **Figure 1.** Major iron aerosol emission source regions.

1049

1050 **3 Modelled dust and iron aerosol concentrations compared to observations**

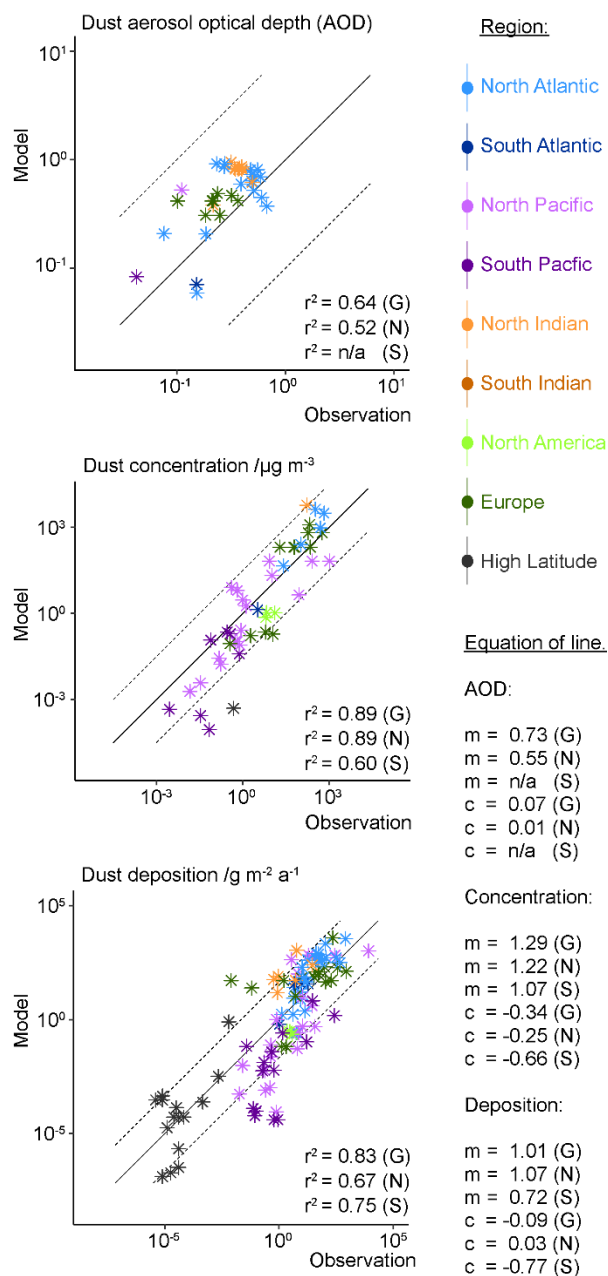
1051 In terms of Earth system modelling, and the biogeochemistry that connects the land–atmosphere–
1052 ocean components, we are ultimately motivated here to improve the magnitude of the atmosphere
1053 to ocean iron deposition flux and its fractional solubility (from which the soluble iron flux can be

1054 derived). We compare the model results with a series of observations, and herein, highlight some
1055 of the problems discovered when directly comparing with a sporadic (in both space and time)
1056 observation dataset, as is currently common practice (Myriokefalitakis et al., 2018).

1057

1058 **3.1 Global dust comparisons**

1059 Comparison of dust AOD with regional dust AOD observations (Fig. 2) from the AERONET
1060 observational datasets (Holben et al., 2000), as subsampled in Albani et al. (2014), shows good
1061 agreement globally (correlation: $r^2 = 0.64$). This results in MAM annual global mean emissions of
1062 $3250 \pm 77 \text{ Tg dust a}^{-1}$, (Aiken = 16 Tg a^{-1} , accumulation = 36 Tg a^{-1} , coarse = 3198 Tg a^{-1}), which
1063 is at the higher end of literature estimates of $\sim 500\text{--}4000 \text{ Tg dust a}^{-1}$ (Bullard et al., 2016; Huneus
1064 et al., 2011; Kok et al., 2017). Dust emissions in MAM are $84 \pm 4\%$ higher than our previous mean
1065 of $1768 \text{ Tg dust a}^{-1}$ in BAM (Scanza et al., 2018), because dust lifetime has proportionally
1066 decreased (Table S2) which affects coarse mode dust aerosol (where 98 – 99% of total dust mass
1067 is emitted) more than fine mode dust aerosol. Globally, both dust concentrations (correlation: r^2
1068 = 0.89) and deposition (correlation: $r^2 = 0.83$) are simulated well compared to observation within
1069 MIMI. A higher correlation of modelled dust concentrations with observations is calculated in the
1070 Northern Hemisphere (NH; $r^2 = 0.89$) compared to the Southern Hemisphere (SH; $r^2 = 0.67$), but
1071 with gradient of line of best fit is further from 1:1 (NH: 1.22 vs. SH: 1.07). Conversely, for dust
1072 deposition a lower correlation with observations is simulated in NH ($r^2 = 0.75$) compared to the
1073 SH ($r^2 = 0.60$) but with a gradient of the line of best fit closer to 1:1 (NH: 1.07 vs. SH: 0.72). Overall,
1074 results presented in this study suggest an improvement in on previous dust modelling
1075 complications related to underestimating dust deposition when tuned to dust concentration
1076 (Huneus et al., 2011).



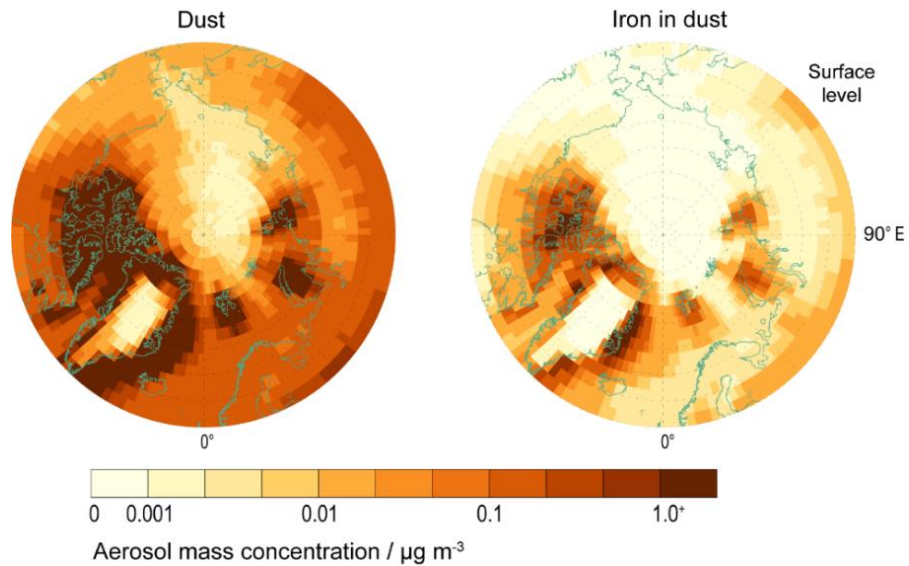
1077

1078 **Figure 2.** Dust aerosol optical depth, surface concentrations and deposition in modal aerosol
 1079 model and observations (Albani et al., 2014; Holben et al., 2000). Correlation (r^2), gradient (m)
 1080 and intercept (c) shown for global (G), Northern Hemisphere (N) and Southern Hemisphere (S)
 1081 regions.

1082

1083 **3.2 High latitude dust and iron aerosol**

1084



1085

1086

1087 **Figure 3.** High latitude (>60°N) dust (sum of eight mineral species and four dust-iron species)
1088 and iron (sum of four dust-iron species) mass concentrations ($\mu\text{g m}^{-3}$) at the surface model level.

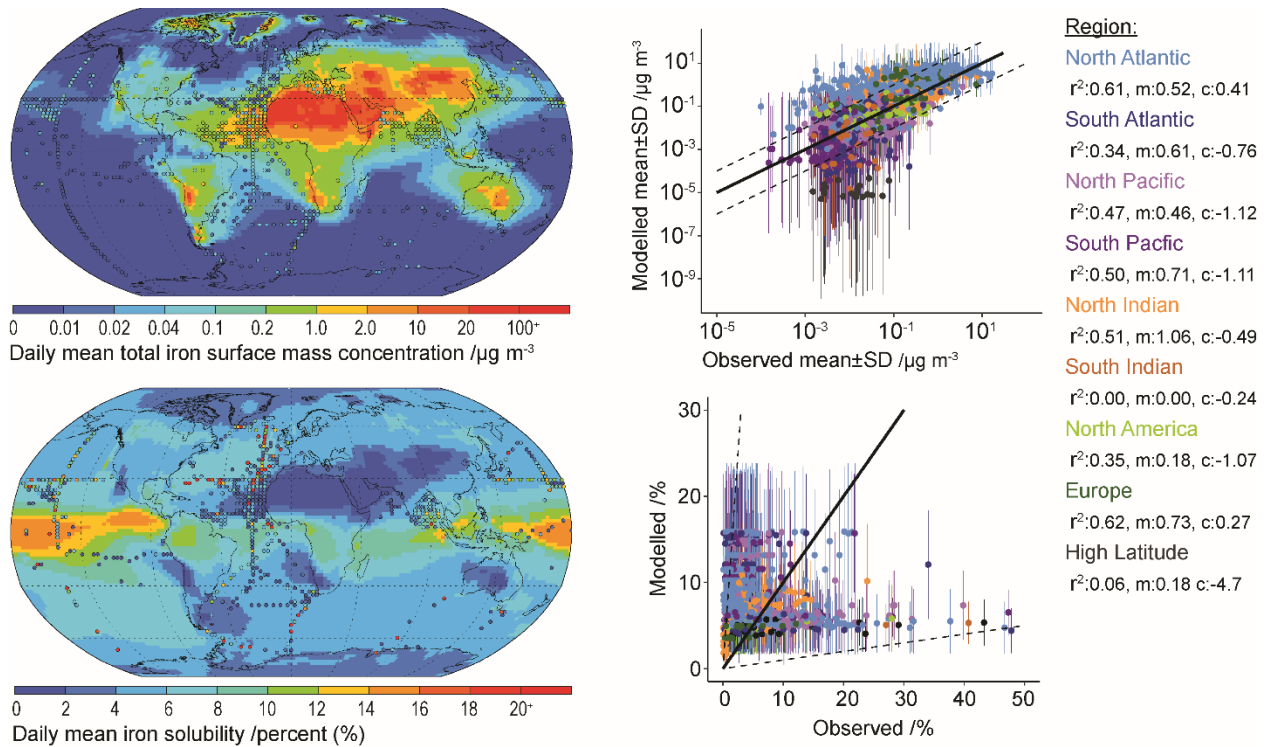
1089

1090 Including the parametrization of Kok et al. (2014a) removes the requirement of a soil erodibility
1091 map (Table 1). In addition, in previous versions of the model, the high latitude dust sources were
1092 zeroed, because there were no observations at that time for high latitude sources of dust (Albani
1093 et al., 2014). However, more recent observations have suggested high latitude dust sources do
1094 exist (Bullard et al., 2016; Crusius et al., 2011; Tobo et al., 2019), often related glacial processes
1095 (Bullard, 2017) with a higher fraction of bioavailable iron relative to lower latitude dust sources
1096 (Shoenfelt et al., 2017). Thus, for the new version of the model we have allowed for the inclusion
1097 of high latitude dust sources (Fig. 3). In general, aerosol dust and iron concentrations peak closest
1098 towards the coast lines and during summer. Emissions of dust from >50°N are $\sim 1.3 \pm 0.2\%$ of the
1099 global dust total, which is half of the estimates derived from field and satellite data at 2–3% of the
1100 global total (Bullard, 2017; Bullard et al., 2016). However, the resulting magnitude and seasonality
1101 of dust concentrations has been shown in a recent study to be consistent with observed
1102 measurements from Svalbard (Tobo et al., 2019).

1103

1104 **3.3 Global iron aerosol concentration and fractional solubility**

1105



1106

1107

1108 **Figure 4.** Daily mean model total iron concentration and solubility from 2007 to 2011.
 1109 Observations (circles) overlaid (at resolution of the model grid) as a mean from 1524 individual
 1110 records in Mahowald et al. (2009) and in Myriokefalitakis et al. (2018). Also shown are scatter
 1111 plots of the model mean and standard deviation compared to each available observation and
 1112 identified by oceanic region. Correlation (r^2), gradient (m) and intercept (c) for total iron with
 1113 observations shown for each region.

1114

1115

1116 There are several propositions explaining the sources of soluble iron, and the inverse relationship
 1117 between total iron amount and iron solubility (Sholkovitz et al., 2012). While total iron mass
 1118 concentrations are dominated by desert dust sources, soluble iron can be a product of mineral
 1119 dust processed in the atmosphere or emitted from different-pyrogenic sources (Chuang et al.,
 1120 2005; Guieu et al., 2005; Ito et al., 2019; Luo et al., 2008; Meskhidze et al., 2003; Schroth et al.,

1121 2009). Previous studies have shown that either of these can explain the inverse relationship, and
1122 that the spatial distribution of data is required to provide more information (Mahowald et al., 2018).
1123 Therefore, we explored how to best use the spatial data to compare with the model results. The
1124 five-year (2007 to 2011) mean iron concentration from MIMI is compared to an extensive dataset
1125 of observations of total iron and its fractional solubility (Fig. 4). ~~Except for between 30 and 60°N~~
1126 ~~in the North Pacific (and near Hawaii) and a latitudinal band ~30°N in the North Atlantic,~~ The
1127 model captures the global mean observational total iron concentration well; however, relatively
1128 low regional correlations ($r^2 < 0.4$) occur in the South Indian ($r^2 = 0.0$), South Atlantic ($r^2 = 0.34$),
1129 North America ($r^2 = 0.35$) and high latitude ($r^2 = 0.06$) ocean regions, suggesting future model
1130 improvements can be focused here.

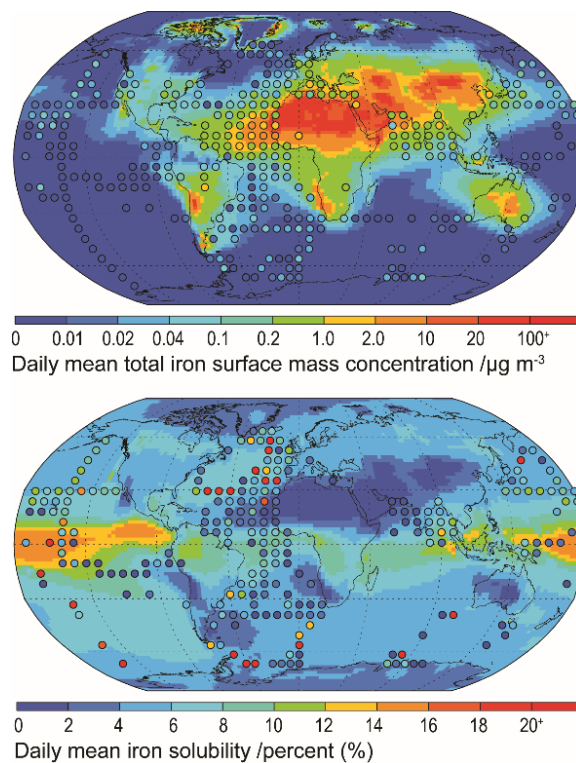
1131 In the absence of iron atmospheric process modelling, ocean biogeochemistry models with an
1132 iron component (e.g., Aumont et al., 2015; Moore et al., 2004) have estimated iron solubility from
1133 offline dust modelling by means of an assumption that it contains 3.5% iron by weight, of which
1134 2% is soluble. Iron solubility is highly temporally and spatially variable however, and in the
1135 absence of spatial atmospheric emission information, pyrogenic iron sources, and atmospheric
1136 processing of iron an estimate of 2% solubility leads to underestimates of observed iron solubility
1137 in nearly all HNLC ocean regions (Fig. 4).

1138 Aggregating observations onto a lower resolution grid (sometimes termed ‘super-obbing’)
1139 compared with the model can help reduce the representation error when comparing with such
1140 limited observations (Schutgens et al., 2017). Fig. 5 uses an observational resolution one-third
1141 that of the model and the model-to-observation comparison of the mean state is thus improved.
1142 Persistent observation-based features of the local environment become more obvious while,
1143 conversely, less frequent ones diminish. At this observational resolution, the low total iron
1144 concentrations in the North Atlantic ~30°N, as seen in Fig. 4, are perhaps not a common feature,
1145 and the model much more precisely represents the climatological state here than Fig. 4 might
1146 suggest. However, examining the North Pacific reveals that the model imprecisely represents the
1147 mean state here. Potential missing iron sources in remote regions, such as the North Pacific,
1148 include: (1) shipping emissions (Ito, 2013), which have a high soluble iron content from oil
1149 combustion (Schroth et al., 2009); (2) volcanic emissions, which provide a localized “fertilizer” to
1150 the surface ocean owing to the macronutrients and trace metal nutrients contained within them
1151 (Achterberg et al., 2013; Langmann et al., 2010; Rogan et al., 2016); and (3) low Asian and South
1152 American aerosol concentrations, either through underrepresenting combustion emission sources

1153 (Matsui et al., 2018) or in the transport and deposition of aerosol within these regions (Wu et al.,
1154 2018). These are discussed in more detail in the discussion [Sections 5.1 and 5.2](#).

1155

1156



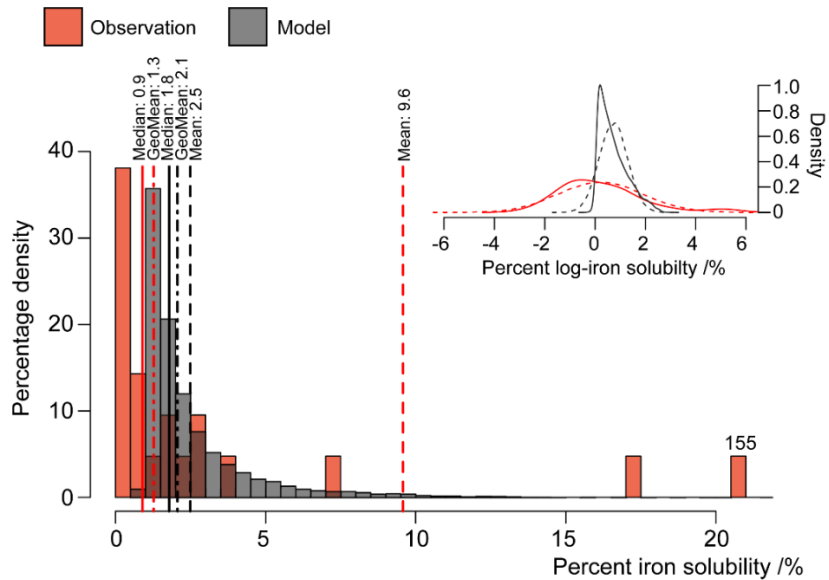
1157

1158

1159 **Figure 5.** Daily mean model total iron concentration and solubility from 2007 to 2011.
1160 Observations (circles) overlaid (at resolution one-third of the model grid) as a mean from 1524
1161 individual records in Mahowald et al. (2009) and in Myriokefalitakis et al. (2018).

1162

1163



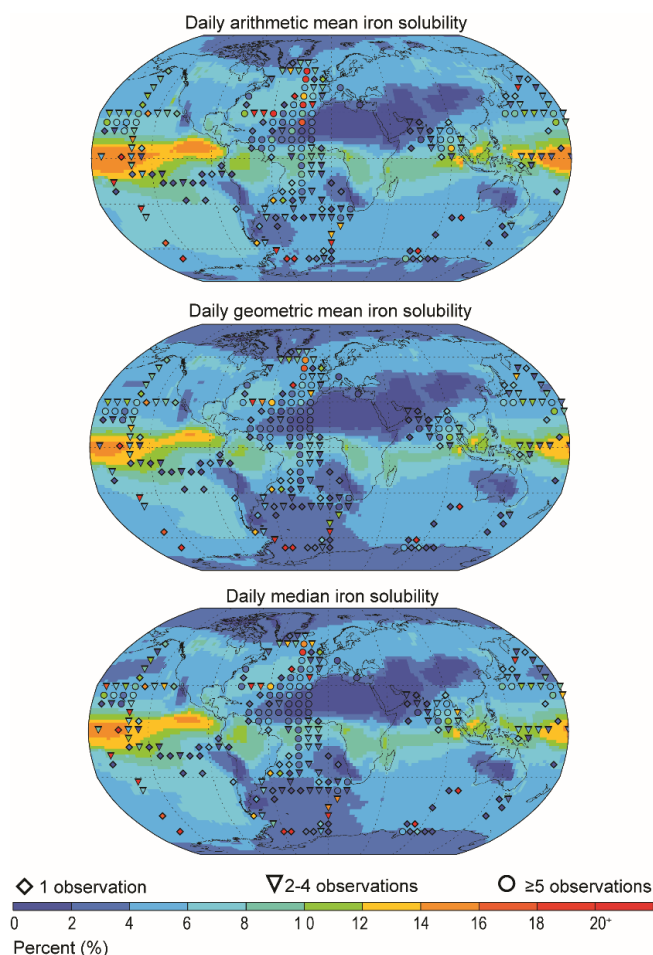
1164

1165 **Figure 6.** Histogram of observations (n = 21) and daily model results (2007 to 2011) of iron
 1166 solubility between 16 to 20°N and 27 to 32°W (one observation point and nine co-located model
 1167 grid cells in Fig. 4). Mean (dashed lines), geometric mean (dot-dash lines) and median (full line)
 1168 values shown above respective dataset colour line. Note that the single observation value of
 1169 155% is off the scale and placed as such with value given above. **Insert.** Log-plot for the same
 1170 data (solid lines) with projected log-normal distribution from mean and standard deviation of data
 1171 (dashed lines).

1172

1173 In terms of iron solubility (soluble iron concentration / total iron concentration), the model is not
 1174 capturing the observational mean state in many regions (Fig. 5). A detailed examination of the
 1175 observation point at 18°N and 330°E (anomalous green point surrounded by blue points in the
 1176 North African outflow plume in Fig. 4) and the nine model grid cells co-located with it in Fig. 6
 1177 shows how a single high observation (155% percent solubility) is causing a representation issue
 1178 (see also section 4.3.1 regarding soluble iron deposition). Both model and observation histogram
 1179 distributions are similar, as are the median (model: 1.8, observation: 0.9) and geometric mean
 1180 (model: 2.1, observation: 1.3) values. However, the arithmetic means are not similar (model: 2.5,
 1181 observation: 9.6) and while a high observation value of 155% is likely to be an outlier, and should
 1182 be at most 100%, it still informs us about what is possible and simply discounting it (even at an
 1183 adjusted 100%) would require strong justification. It is therefore advisable to instead alter the
 1184 estimator of the average. Comparing model to observation differences calculated using the
 1185 median or geometric mean reveals that they are similar in magnitude, as one would expect for

1186 log-normally distributed data (Fig. 6 insert). Although the median is robust with respect to outliers,
1187 the model results may not exhibit a uniform Gaussian distribution (Fig. 6 insert; solid compared
1188 to dashed lines) and often the amount of available observations is also low (Fig. 7) suggesting
1189 that its use also requires careful consideration. An equivalent methodology to the geometric mean
1190 in Fig. 7 would be to first log transform the data before calculating the arithmetic mean. Arguments
1191 pertaining to the appropriate methodology for comparing model results to temporally limited
1192 observations extend beyond the iron aerosol examination in this study to all aerosol comparisons
1193 with limited observations.



1194

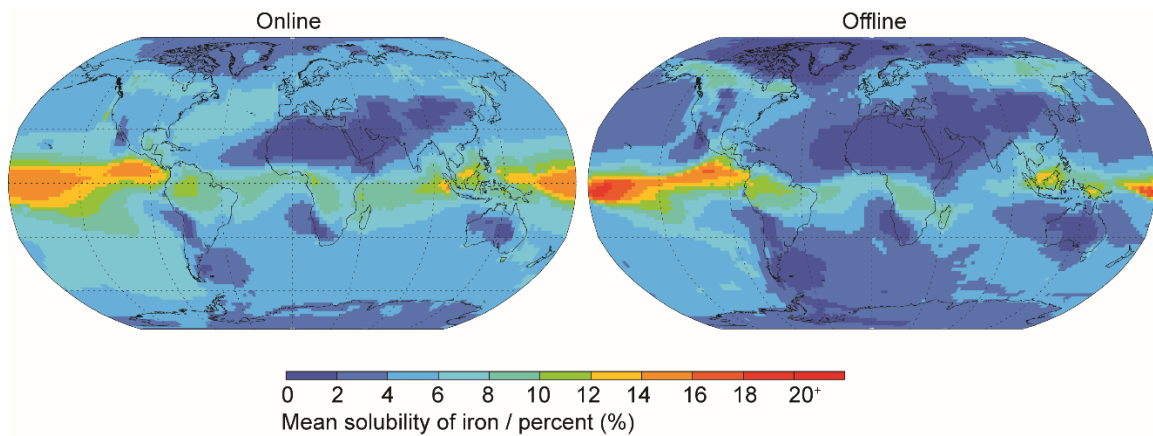
1195 **Figure 7.** Daily arithmetic mean, geometric mean, and median model solubility (2007 to 2011).
1196 Observations overlaid (at resolution one-third of the model grid) as either the arithmetic mean,
1197 geometric mean or median, respective to the model averaging. Number of observations denoted
1198 by symbol: lowest confidence (one observation, diamond); intermediate confidence (two to four
1199 observations, triangle); highest confidence (five or more observations, circle).

1200 **3.4 Calculating iron solubility**

1201 It is interesting to note the effect that the order of operations (taking the average-of-ratios
1202 compared to the ratio-of-averages) has when calculating iron solubility (Fig. 8). Throughout **the**
1203 **this studymanuscript**, percent iron solubility was calculated at each model time step (30 minutes)
1204 and then the daily mean output analysed (online; Equation 6) at an annual or 5 year mean time
1205 resolution. It is also acceptable to use the simulated soluble and total iron concentrations to
1206 generate the annual or 5 year mean iron solubility in a postprocessing step (offline; Equation 7).
1207 The resulting differences between methods **is-are** not insignificant however, with the offline
1208 method creating a distribution in which, low iron solubility is generally lower and the highest
1209 (>18%) iron solubilities are generally higher. **Overall, global annual mean iron solubility calculated**
1210 **online is one-third (34%; NH=40%, SH=29%) higher than when calculated offline.**

1211

1212



1213

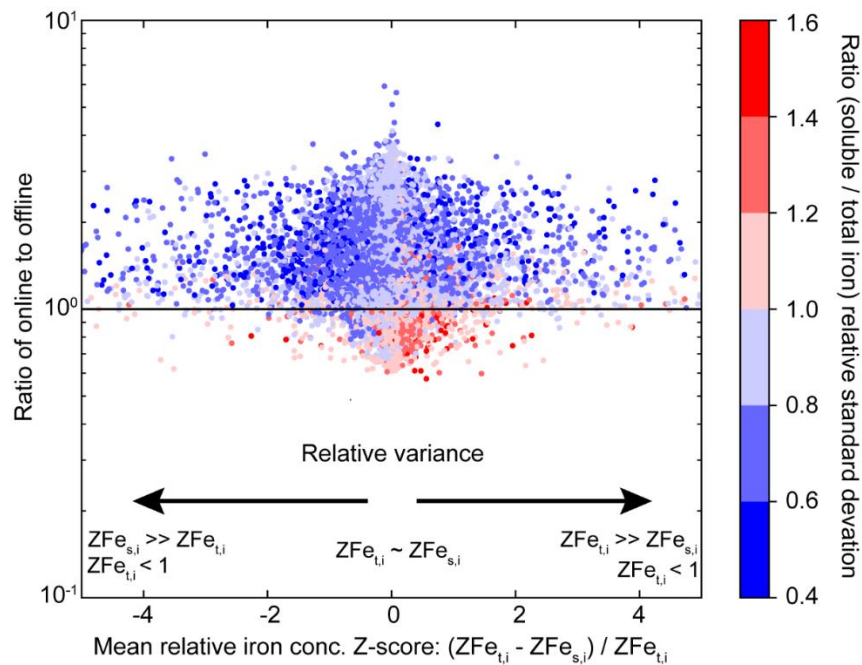
1214 **Figure 8.** Mean solubility of iron when solubility is calculated at each 30 min model time step
1215 ('online') and when it is calculated post processing from the daily mean soluble and total iron
1216 concentration ('offline').

1217

1218 The average relative Z-score (Equations 8 and 9) is around zero for most model grid cells (Fig.
1219 9) indicating that they mostly followed similar temporal and relative magnitude trends. However,
1220 even if the average relative Z-scores are around zero and the ratio of relative standard deviations
1221 is around one, the ratio of online:offline calculated iron solubility is most likely >1. Temporal
1222 differences in the soluble and total iron concentration might therefore be controlling the overall

1223 solubility at each model grid cell. We also find that the ratio of online and offline solubility is >1 for
 1224 most of the cases when the ratio of relative standard deviations of soluble and total iron is <1 (Fig.
 1225 S42), indicating that the differences in ~~the~~ both methods of iron solubility calculation are sensitive
 1226 to the differences in relative size of the tails of the distribution. That is, if soluble iron has narrower
 1227 tails compared to total iron at any grid cell, it is highly likely that a higher solubility will be obtained
 1228 in the online method compared to the offline. ~~We also find that the ratio of online and offline~~
 1229 ~~solubility is >1 for most of the cases when the ratio of relative standard deviations of soluble and~~
 1230 ~~total iron is <1 (Fig. S1), indicating that the differences in the both methods of solubility calculation~~
 1231 ~~are sensitive to the differences in relative size of the tails of the distribution. That is, if soluble iron~~
 1232 ~~has narrower tails compared to total iron at any grid cell, it is highly likely that a higher solubility~~
 1233 ~~will be obtained in the online method compared to the offline.~~ The extreme ratio of the tails of
 1234 soluble and total iron are generally only found around in specific regions with highest temporal
 1235 variability in emissions and modelled solubilization of insoluble iron (Fig S42).

1236



1237

1238 **Figure 9.** Relationship of online to offline derived iron solubility to the relative Z-score for total
 1239 (ZFe_t) and soluble (ZFe_s) iron and the relative standard deviation ($\sigma Fe / \overline{Fe}$) at each grid cell for
 1240 the year 2007.

1241

1242 Field measurements have generally suggested an inverse relationship between total and soluble
1243 iron concentrations (Myriokefalitakis et al., 2018). This means that high total iron concentrations
1244 are generally accompanied by low soluble iron concentrations and vice versa. By assuming that
1245 the field measurements faithfully represented the actual average values of soluble and total iron
1246 concentration at those locations, we implicitly assume that all the measurements have a Z-score
1247 of zero. In Fig. 9 we show that this is not the case with the modelled results, and the two variables
1248 can be relatively farther from their respective means even when averaged over the modelled time
1249 period.

1250 Sensitivity of a result to the order of operations extends beyond iron solubility to any variable that
1251 is calculated in a similar manner, and current multi-model inter-comparison project (MIP) protocols
1252 do not explicitly account for this. However, the effects of outliers, in both online and offline
1253 methods, can be reduced by employing the geometric mean and has been used in some MIP's
1254 (e.g., Mann et al., 2014). It will be also be important to consider differences in the solubility of iron
1255 induced by the choice of the order of operations as ocean biogeochemical models move away
1256 from using offline results from global climate or chemistry transport models to online results within
1257 Earth system models, which are designed to couple the two components at each time step. For
1258 short term interactions between deposited iron and ocean biota shorter term averaging may be
1259 more important (e.g., Guieu et al., 2014), but for long term period accumulation of iron that is
1260 (re-)cycling in the oceans, the longer term average may be more appropriate (Moore et al., 2013).
1261 One should be aware, however, that iron is readily removed from the ocean mixed layer, and
1262 thus, the lifetime of iron may well be short enough for the 'online' calculation to be more
1263 appropriate much of the time (Guieu et al., 2014).

1264

1265

1266 **4.0 MIMI vs. BAM-Fe**

1267 In this section, we discuss how the new modal aerosol mode version of MIMI compares to its
1268 predecessor bulk aerosol model version (BAM-Fe) throughout all three stages of the atmospheric
1269 iron life-cycle.

1270

1271

1272 **4.1 Iron emission comparison**

1273 Globally averaged emissions of dust (3200 Tg a⁻¹) and its iron component (126 Tg a⁻¹) are within
 1274 the current multi-model range (Table 7). The simulated annual mean iron in dust percentage is
 1275 4.1%, with the highest percent occurring in the coarse mode at 6.5% and lowest percent occurring
 1276 in the Aiken mode at 1.1%. Accounting for dust mineralogy therefore increases the global mean
 1277 iron percent by weight above the currently well-used global mean estimate of 3.5% (e.g., Jickells
 1278 et al., 2005; Shi et al., 2012).

1280 **Table 76.** Dust, fire, and combustion emissions of iron and relevant co-emitted aerosol emissions
 1281 (to two significant figures). Multi-model emission range from the four global atmospheric iron
 1282 models (including BAM-Fe) reported in Myriokefalitakis et al. (2018). Fine (sum of Aiken and
 1283 accumulation modes) and coarse (coarse mode) size mass emissions also given for dust, fire iron
 1284 and combustion iron.

1285

	Annual mean emissions /Tg a ⁻¹			
	BAM-Fe	MIMI	Luo et al. (2008)	Multi model
Dust	1800	3200	1600	1200–5100
<u>Fine, Coarse</u>	<u>20,1700</u>	<u>50, 3200</u>		
Dust iron	57	126 <u>30</u>	55	38–13 <u>04</u>
<u>Pyrogenic iron</u> <u>(Fire&Comb.)</u>	1.9	5.5	1.7	1.8–2.7
Fire BC	4.1	2.6	3.6	
Total fire iron	1.2	2.2	1.1	
Fine, Coarse	0.08, 1.1	0.30, 1.90	0.07, 1.00	
Combustion BC	4.6	5.0	5.0	
Total comb. iron	0.66	3.3	0.66	
Fine, Coarse	0.10, 0.56	0.50, 2.80	0.10, 0.56	

1286

1287 Compared to BAM-Fe, MIMI dust emissions are ~80% higher and the iron it contains is ~120%
1288 higher ~~in MIMI compared to those in BAM-Fe~~ (Table 76). Although both the BAM-Fe and MIMI
1289 models are globally tuned to a similar dust AOD (~0.03), and based within the same host model
1290 (CESM), changing from a bulk aerosol scheme (e.g., Albani et al., 2014; Scanza et al., 2015) to
1291 a modal aerosol scheme (~~e.g., Albani et al., 2014; Scanza et al., 2015~~) reduces the aerosol
1292 lifetime significantly (Liu et al., 2012 and Table S2). The spatial distribution of dust emissions is
1293 also different following the move to the Kok et al. (2014a, 2014b) parameterization (Table 1),
1294 resulting in the spatial distribution of dust AOD also altering (Fig. S23). Total combustion
1295 pyrogenic iron emissions (sum of fires and anthropogenic combustion activity) in MIMI are also
1296 higher than previous estimates by a factor of between two and three (Table 76), reflecting the
1297 recently growing evidence indicating that they have been previously underestimated (Conway et
1298 al., 2019; Ito et al., 2019; Matsui et al., 2018).

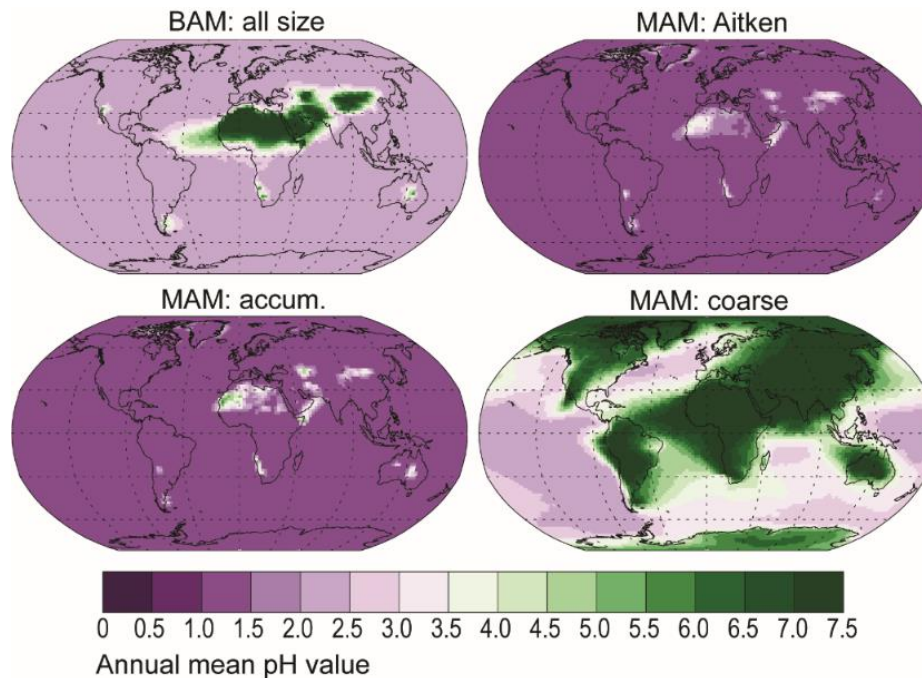
1299

1300 **4.2 Iron atmospheric processing comparison**

1301 There is a much lower aerosol pH in the fine aerosol modes (Aitken and accumulation) in MIMI
1302 compared to that in BAM-Fe (Fig. 10). This is due to a combination of resolving pH in each aerosol
1303 size mode in MIMI and the subsequent lowering of the pH value (1) being applied in the two fine
1304 aerosol modes (Aitken and accumulation). Conversely, dust dominating the coarse aerosol mode
1305 provides more of an opportunity for [Calcite] > [SO₄] in this aerosol size fraction, resulting in most
1306 continental areas having a high coarse mode aerosol pH in MIMI compared with the higher pH
1307 being much more localized to the major desert regions in BAM-Fe. Acidic processing of iron in
1308 MIMI ~~is~~ therefore proceeds faster globally in the ~~two~~ fine sized aerosol modes (Aitken and
1309 accumulation) compared to the BAM-Fe fine ~~mode~~ size bin (0.1-1 μ m), but generally slower over
1310 continental regions in the coarse mode than in BAM-Fe coarse size bins (1-10 μ m).

1311 Comparison of Fig.10 to modelled pH estimates by Myriokefalitakis et al. (2015) shows generally
1312 good agreement in the NH, but in the SH MIMI simulates less acidic coarse mode aerosol over
1313 continental regions and more acidic aerosol over marine regions. As iron models are unable to
1314 capture the high observed iron solubility (>10%) over SH marine regions (Myriokefalitakis et al.,
1315 2018), and in the absence of remote pH aerosol observations, we suggest that our basic
1316 parameterization captures an aerosol pH which is suitable for use in Earth system models

1317

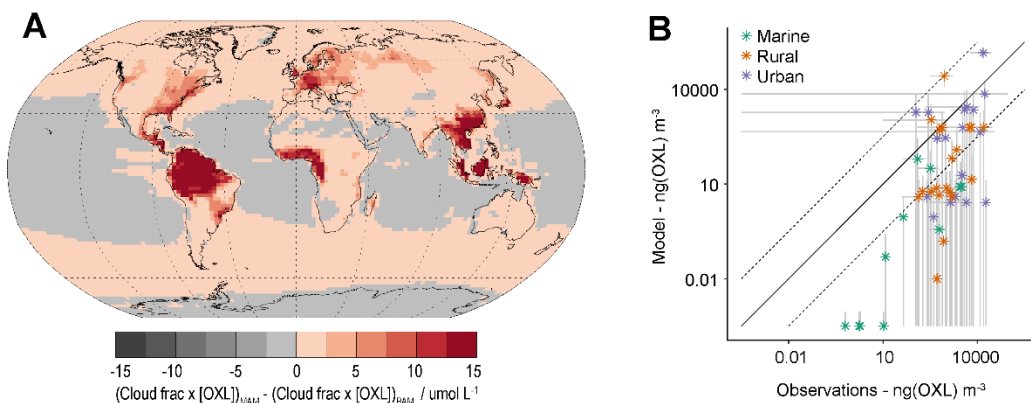


1318

1319 **Figure 10.** Surface level annual mean interstitial aerosol pH. If [SO₄] > [Calcite] then pH = 1 in
 1320 Aitken and accumulation modes or 2 in coarse, else pH = 7.5 (Table 5)(see methods for pH
 1321 calculation).

1322

1323 Model physics, and hence simulated cloud cover, is significantly different between CAM4 and
 1324 CAM5. Fig. 11a shows the relative model difference in the oxalate dissolution-reaction distribution
 1325 between MIMI, which also includes an increase in the tuning factor by an order of magnitude (from
 1326 15 to 150; Table 5), and BAM-Fe by normalising by the simulated cloud fraction in each model
 1327 respectively. The effect of oxalate on iron dissolution is therefore larger in MIMI over extra-tropical
 1328 ocean regions, where iron models underrepresent solubility (Myriokefalitakis et al., 2018), and
 1329 land regions which are dense in tropical vegetation or industry (both centres of large aerosol pre-
 1330 cursor gas emissions). Compared to observations (Myriokefalitakis et al., 2011; Table S3)
 1331 modelled oxalate concentrations are well represented at high observed concentrations but are
 1332 biased low when observed concentrations are low (Fig. 11b). The low model bias is stronger
 1333 within remote observational regions (marine vs. urban observation sites), suggesting that the
 1334 removal of secondary organic aerosol may be too strong within the model and/or that there is a
 1335 missing marine aerosol pre-cursor gas emissions source (Facchini et al., 2008; O’Dowd and de
 1336 Leeuw, 2007) in this model which significantly lowers simulated secondary organic aerosol, and
 1337 thus oxalate, concentrations.



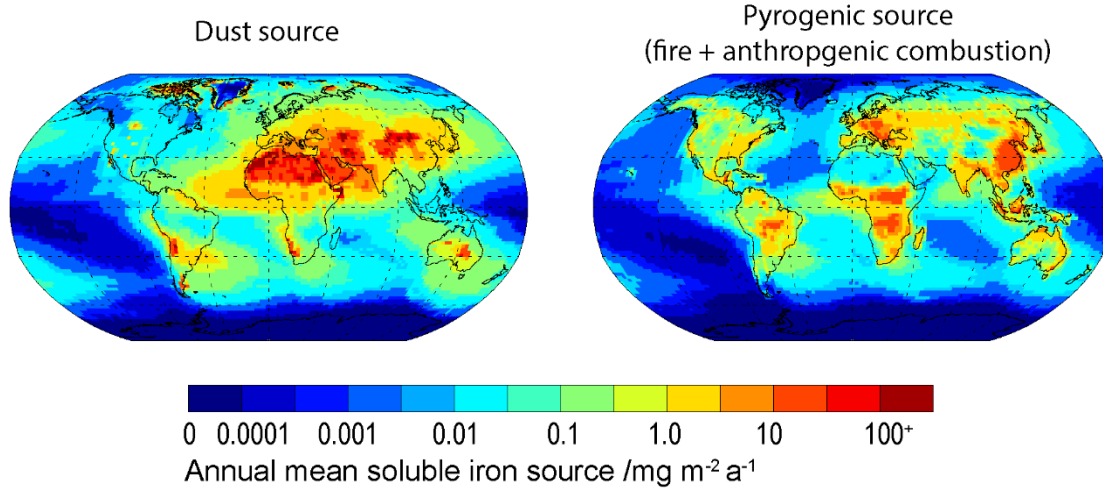
1338

1339

1340 **Figure 11. A:** Relative difference in organic ligand reaction on in-cloud iron aerosol dissolution
 1341 between MIMI and BAM-Fe. Due to significant differences in simulated cloud cover between
 1342 CAM4 and CAM5 oxalate concentrations [OXL] are multiplied by the model simulated cloud
 1343 fraction in this figure. **B:** Surface level oxalate (OXL) concentration in the model and observations.
 1344 Model values are annual mean (2007-2011) and monthly standard deviation. Observation values
 1345 are from Table S3 in Myriokefalitakis et al. (2011) and reported with uncertainty where given.

1346 Comparison of mineral dust and pyrogenic sources of modelled soluble iron (sum of emissions
 1347 and atmospheric dissolution; Fig. 12) with the four iron models (including BAM-Fe) reported by
 1348 Myriokefalitakis et al. (2018) shows that the spatial distribution in MIMI is broadly similar for most
 1349 regions of the world. A notable difference exists in the North Pacific region where the soluble iron
 1350 source in MIMI is lower than all other iron models, and similarly with total iron concentrations when
 1351 compared to observations (Figs. 4 and 5). Future development of MIMI should thus be focused
 1352 on the North Pacific, including the addition of shipping soluble iron emissions which are relatively
 1353 concentrated in this region (Ito, 2013). An improvement for MIMI can be seen over the Atlantic
 1354 region directly downwind of Saharan soluble iron sources. In general, iron models are over
 1355 representing iron solubility close to dust sources compared to observations (Myriokefalitakis et
 1356 al., 2018) and in order for BAM-Fe to reach better agreement with observed iron solubility in this
 1357 region dust emissions of soluble iron had to be scaled downwards (Conway et al., 2019). We
 1358 suggest this improvement is linked to the improved modal representation of aerosol pH in MIMI
 1359 (Fig. 10).

1360



1361

1362 **Figure 12.** Annual mean dust and pyrogenic (sum of fires and anthropogenic combustion)
 1363 soluble iron source (i.e., sum of emissions and atmospheric processing).

1364

1365 4.3 Iron ocean deposition flux comparison

1366 Similar to the previous study by Scanza et al. (2018), we report the amount of total and soluble
 1367 iron deposited in each of the major ocean basins (Table 87) as defined by Gregg et al. (2003).
 1368 We find that, in MIMI the amount of total iron deposited in-to all ocean basins is approximately
 1369 double that estimated in BAM-Fe (26 vs. 12 Tg Fe a⁻¹, respectively), while soluble iron deposition
 1370 is similar (~0.5 Tg Fe a⁻¹ in both models). The larger mineral dust emission flux in MIMI (3200 Tg
 1371 dust a⁻¹ compared to BAM-Fe dust emission of 1800 Tg dust a⁻¹) is driving most of the increases
 1372 to total iron deposition because it is the primary iron source (Table 67). In general, the magnitude
 1373 of soluble iron deposition to the oceans is more evenly distributed across hemispheres in MIMI
 1374 owing to a major reduction (approximately one half) in the equatorial North Central Atlantic basin
 1375 deposition flux and increases to Southern Hemisphere (SH) ocean deposition fluxes of a factor of
 1376 two to four. In MAM4 dust is treated as internally mixed aerosol with sea salt, leading to higher
 1377 rates of wet deposition than when dust is externally mixed aerosol (Liu et al., 2012) as it is in
 1378 CAM4. The internally mixed treatment of dust aerosol in MAM4 is thus an important factor leading
 1379 to the lower simulated dust lifetime when compared to BAM-Fe (Table S2). Over the North Central
 1380 Atlantic region, the combination of a lower soluble iron source (Fig. 12 compared to Fig S4b by
 1381 Myriokefalitakis et al. (2018)), dust atmospheric lifetime (Table S2), lower aerosol pH (Fig. 10),
 1382 and lower relative organic ligand processing (Fig. 11) will all work towards reducing the magnitude

1383 of atmospheric soluble iron deposition flux in MAM4 compared to BAM-Fe. There are significant
 1384 increases in anthropogenic combustion iron deposition in all equatorial and Northern Hemisphere
 1385 (NH) ocean basins, driven by the 5-fold increase in combustion emissions implemented in MIMI.
 1386 The percent contribution from pyrogenic iron to total iron deposition between MIMI and BAM-Fe
 1387 is however more similar for all northern and equatorial oceanic regions than southern oceanic
 1388 regions. Beyond the correction to anthropogenic combustion emissions, which are NH dominated,
 1389 this could be due to differences in the emissions of both dust and fire aerosol, structural
 1390 differences between models relating to the aerosol size and composition which alters aerosol
 1391 deposition rates, or a lower soluble iron source (Fig. 12); it is most likely to be a combination of
 1392 all three.

1393
 1394 **Table 78.** Global and regional ocean basin deposition ($Gg\ a^{-1}$) of total and soluble iron in BAM-
 1395 Fe (Scanza et al., 2018) and MIMI (this study). Deposition was multiplied by the ocean fraction of
 1396 model grid cell and is reported at two significant figures. Percent contribution from pyrogenic (sum
 1397 of fires and anthropogenic combustion) iron sources to deposition also given. Ocean basins are
 1398 those defined by Gregg et al. (2003) and previously used by Scanza et al. (2018).
 1399

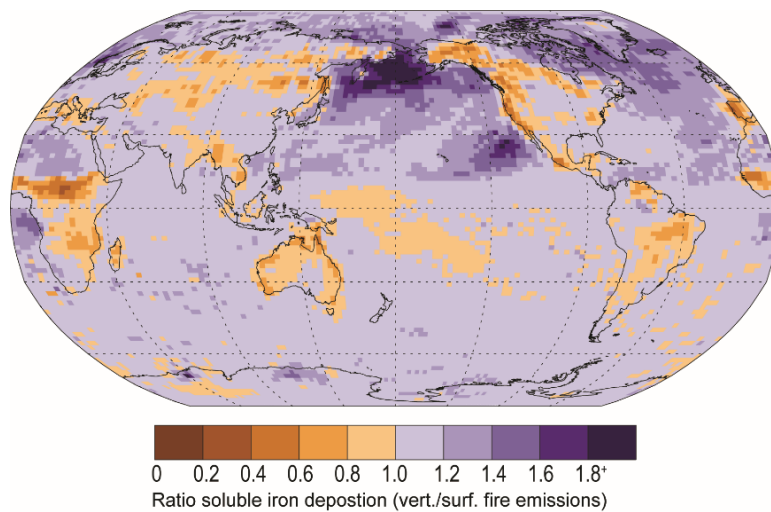
	Dust and comb. deposition /Gg a ⁻¹				Percent <u>iron</u> from <u>pyrogenic sources</u> /%			
	Total iron		Soluble iron		Total iron		Soluble iron	
	BAM-Fe	MIMI	BAM-Fe	MIMI	BAM-Fe	MIMI	BAM-Fe	MIMI
Global	12000	26000	500	530	3.3	5.0	7.6	23
N. Atlantic	1800	5300	46	86	1.9	2.9	4.8	11
N. Pacific	730	1200	35	36	10	19	15	43
NC. Atlantic	2900	5700	92	89	0.30	0.52	0.9	3.7
NC. Pacific	230	300	16	12	7.9	24	10	56
N. Indian	2700	7000	62	101	1.2	2.1	3.9	10
Eq. Atlantic	2600	2600	190	95	2.8	9.9	5.5	34
Eq. Pacific	59	91	6.2	6.7	21	37	25	68
Eq. Indian	830	1200	35	39	5.9	12	11	38
S. Atlantic	65	790	4.1	16	30	4.8	50	25
S. Pacific	21	250	1.4	6.4	41	7.8	50	30
S. Indian	42	200	3.0	6.9	51	16	58	46
Antarctic	270	1300	12	37	20	12	48	44

1400
 1401

1402 The fraction of fire aerosol which is injected above the boundary layer is crucial for determining
1403 its capacity for long range transport (e.g., Turquety et al., 2007). Vertically distributing fire iron
1404 emissions in MIMI, as compared to emitting all iron from fires at the surface as in BAM-Fe,
1405 increases the long-range transport of iron aerosol to remote ocean regions (Fig. 4213). In general,
1406 vertically distributing fire emissions results in small increases in soluble iron deposition (between
1407 0 and 20%) in SH ocean regions and a larger increase (between 20 and 40%) to NH oceans, with
1408 converse lower land deposition close to the major regions of fire activity. The exception being in
1409 the sub-Arctic North Pacific, a HNLC region, where iron deposition from fires significantly
1410 increased until more than doubling that when surface fire emissions are used. ~~The modelled ratio
1411 change in deposition between vertical/surface emissions will be sensitive to the vertical resolution
1412 of the model, where a higher resolution in the bottom layers will lead to increases in near-source
1413 deposition for surface emissions.~~

1414 The dry deposition flux is sensitive to the aerosol properties, surface roughness and modelled
1415 turbulence. Although increasing the vertical resolution has been shown to increase surface PM₁₀
1416 concentration (Menut et al., 2013) and better simulate the dust vertical profile (Teixeira et al.,
1417 2016), it is not as yet clear if this would correspondingly increase the dry deposition flux.

1418



1419

1420

1421 **Figure 4213.** The ratio of soluble iron deposition from fires when emissions are emitted with a
1422 vertical distribution to fires compared with when emission are only at the surface (i.e.,
1423 vertical/surface). Single year (2007) comparison only.

1424

1425 4.3.1 Source region comparison

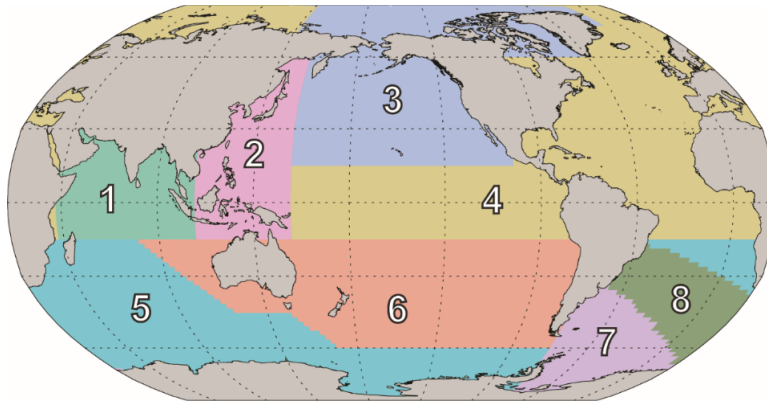
1426 The eight regions in Fig. 1314 are chosen based on 10 (one for each region in Fig. 1) simulations
1427 undertaken using the modified version of BAM-Fe described in the methods [Section 2.6](#). The
1428 emission region (Fig. 1) with the highest fractional contribution to the total soluble deposition flux
1429 in each grid cell was examined and from this the boundaries of each region in Fig. 1214
1430 delineated. The resulting eight ocean iron deposition regions are split equally into four in the NH
1431 and four in the SH. Note, however, that the NH–SH divide sits at 15° S, and not the equator, which
1432 is due to transport differences in each hemisphere and the position of the [ITCZ/Inter Tropical](#)
1433 [Convergence Zone](#). Of the four regions that can be defined as being major dust deposition
1434 receptors (Fig. 144; [bottom panel](#) bar chart) the North Indian Ocean (#1), North Atlantic and
1435 Central Pacific (#4), and South America dust (#7) regions have a single dominant source each,
1436 while the North Pacific (#3) region is more variable. These dust-dominated iron deposition regions
1437 are similarly reproduced by other global iron models (Ito et al., 2019; Myriokefalitakis et al., 2018).
1438 The regions of the Southern Hemisphere Oceans (#5) and Australian and South Pacific (#6)
1439 receive similar amounts of mineral dust and [combustion-pyrogenic](#) iron, suggesting that the iron
1440 sources are spatially closer and, thus, share much more similar transport pathways than the South
1441 East Asian Ocean (#2) and South America [Combustion-Pyrogenic](#) (#8) regions, which have a
1442 much more distinct [combustion-pyrogenic iron](#) source signal. Deposition regions are more clearly
1443 defined when using this methodology compared to those from a more traditional classification of
1444 ocean basins based on physio-geographical oceanography (Fig. S34). This information can be
1445 used to assess which ocean regions are most likely to be affected by anthropogenic perturbations
1446 to the magnitude of iron sources within different regions, whether through land use land cover
1447 change or industrialization.

1448

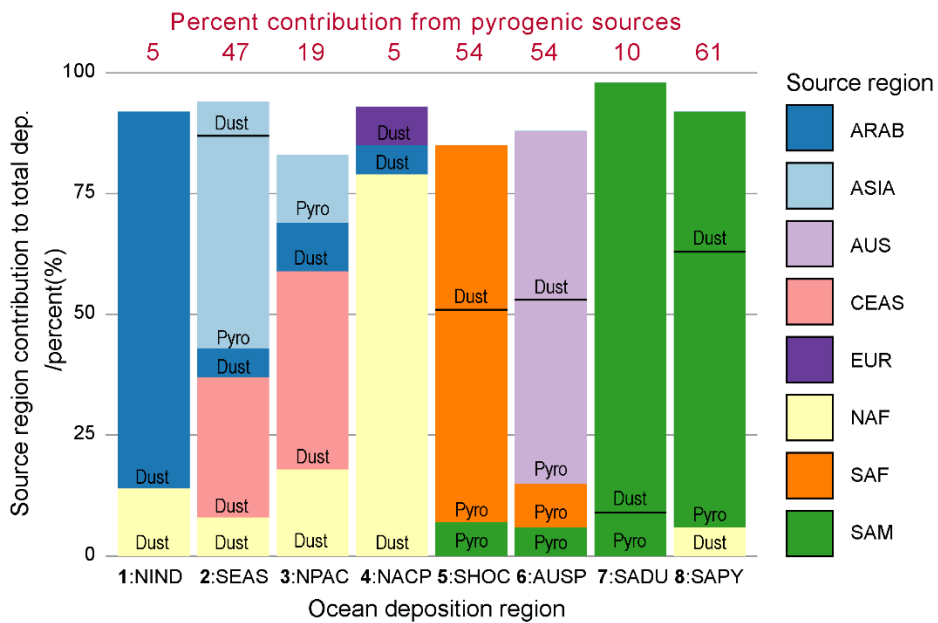
1449 The variability in the daily soluble iron deposition flux to each of the eight ocean regions, as seen
1450 in Fig. 1314, is much larger in MIMI than it is in BAM-Fe (Fig. 1415), reaching over 10 orders of
1451 magnitude between the minimum and maximum flux in many regions. This is due in part to the
1452 increased variability in fire emissions, which was improved in MIMI to track the BC emitted from
1453 fires, and switching from the offline soil erodibility map used in BAM-Fe to the Kok et al. (2014a)
1454 physical based emission parametrization used in MIMI. Anthropogenic combustion emissions are
1455 temporally static in both model frameworks, and therefore do not affect the variability in this study
1456 as much as fires and mineral dust but will in future if this is changed to represent a seasonal

1457 emission cycle. We can see that each of the dust and fire updates in MIMI are having a large
1458 impact by comparing the Patagonian dust dominated South America Dust (SADU) region and the
1459 fire dominated South America ~~Combustion~~ Pyrogenic (SAPYGO) region. Most of the dust
1460 deposited (30 to 90%) in the ocean occurs during large dust events that are on just 5% of the
1461 days (Mahowald et al., 2009) resulting in large differences between median and mean deposition
1462 amounts in all regions, as seen in Fig. 4415. It is important to note that the mean is always above
1463 the inter-quartile range, further supporting our previous arguments pertaining to the modelled
1464 mean not being an ideal estimate of the average as it does not represent the log normal
1465 distribution of aerosol. Comparing the mean:median ratio suggests that extreme dust events are
1466 also more pronounced in MIMI (CAM5) than those in BAM-Fe (CAM4).

1467



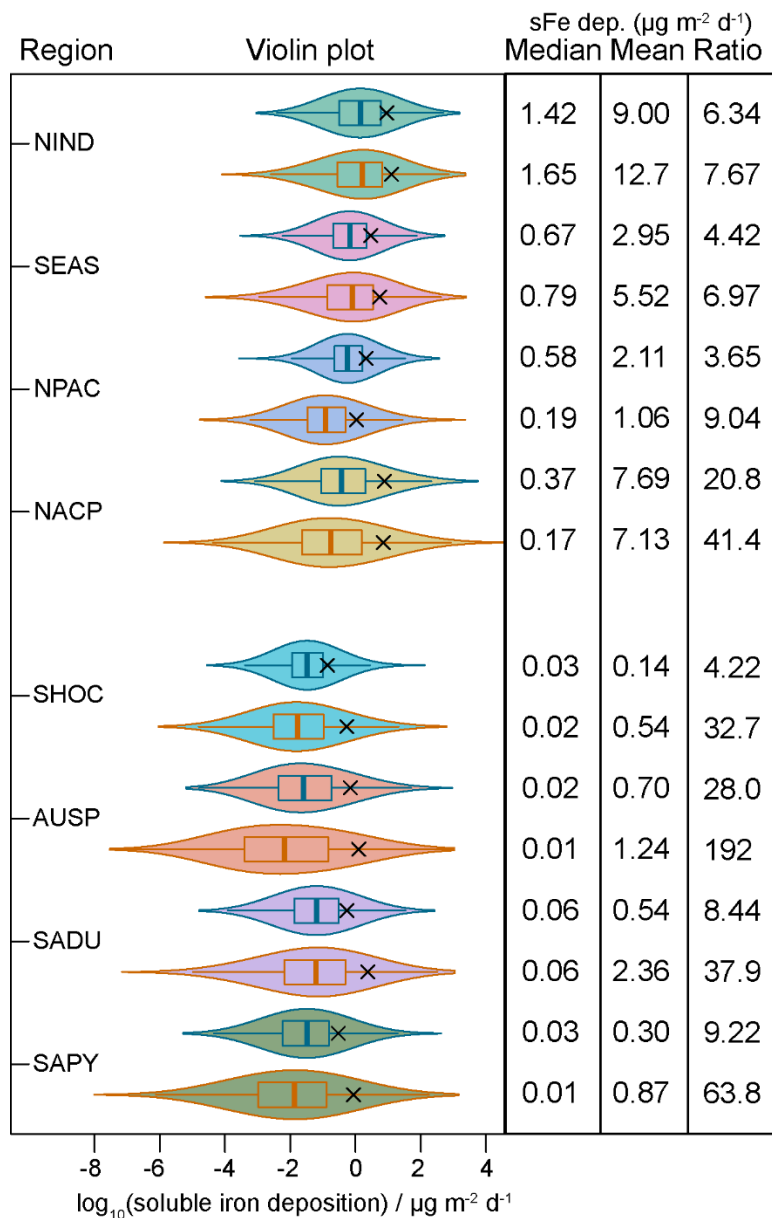
1468



1469

1470 **Figure 1314. Top.** Eight ocean soluble iron deposition regions defined by dominant source region
 1471 apportionment. Region 1: North Indian Ocean (NIND). Region 2: South East Asian Ocean
 1472 (SEAS). Region 3: North Pacific (NPAC). Region 4: North Atlantic and Central Pacific (NACP).
 1473 Region 5: Southern Hemisphere Oceans (SHOC). 6: Australian and Southern Pacific (AUSP). 7:
 1474 South America Dust (SADU). 8: South America Combustion-Pyrogenic (SAPYCO). **Bottom.**
 1475 Contribution of each emission source region (Fig. 1) to the total iron deposition across the region.
 1476 Contribution of dust and pyrogenic (sum of fires and anthropogenic combustion) combustion iron
 1477 from source region also shown. Regions contributing <5% filtered out.

1478



1479

1480 **Figure 1415.** Violin plots of five years of \log_{10} daily soluble iron deposition ($\mu\text{g m}^{-2} \text{d}^{-1}$) within each
 1481 grid cell for the eight ocean regions defined in Fig. 1314. Only grid cells where ocean fraction >0.5
 1482 are included in analysis. Violin colour matches Fig. 1 region colour: North Indian Ocean (NIND);
 1483 South East Asian Ocean (SEAS); North Pacific (NPAC); North Atlantic and Central Pacific
 1484 (NACP); Southern Hemisphere Oceans (SHOC); Australian and Southern Pacific (AUSP);
 1485 Southern American Dust (SADU); Southern American Combustion (SAPYGO). Violin outline
 1486 colours: blue lines = BAM results while orange lines = MAM results. Black cross = \log_{10} mean
 1487 daily soluble iron deposition. Median, mean and ratio (mean/median) values for all five years of
 1488 daily deposition amounts across each basin also given.

1489 **5 Future directions**

1490 The purpose of model to observation comparisons is to identify situations (regions, times, model
1491 settings, or combinations thereof) in which the model output is inconsistent with observed realities;
1492 with the goal being to further refine the model in the future. Each individual observation represents
1493 a snapshot of the atmospheric state at a specific point in space and time and when an observation
1494 falls outside of the distribution of model output values, from the same location and time, we can
1495 view this as evidence of a model misspecification. For the example of iron modelling, constraining
1496 current model-observation discrepancies would benefit from further exploring the model
1497 sensitivity of simulated iron and its solubility to uncertainties in five major parameter sets: dust
1498 iron emissions, ~~combustion~~ pyrogenic iron emissions, atmospheric iron dissolution chemistry, dry
1499 deposition rates and wet deposition rates. In general, improving the modelled representation of
1500 secondary organic aerosol (including oxalate) and aerosol pH, particularly for remote regions, is
1501 an important task for aerosol modelling and one which would have co-benefits for iron aerosol
1502 modelling. Comparisons of soluble fraction of other aerosol species with observations could also
1503 be used to guide model development.

1504 Here we discuss some of the model parameters which are likely important for improving modelled
1505 iron emissions and deposition in MIMI, and ergo iron process models in general, in the future.

1506

1507 **5.1 Improving iron aerosol Emissions**

1508 Downwind of significant mineral dust sources iron models generally overestimate the observed
1509 amount of total iron (Myriokefalitakis et al., 2018) and soluble iron comparisons are highly
1510 sensitive to the assumed initial solubility of mineral dust iron at emissions (Conway et al., 2019).
1511 Conversely in remote ocean regions, improving the representation of combustion emissions has
1512 been shown to be a necessary step towards more accurate representations of observed high iron
1513 solubilities at low iron concentrations (Ito et al., 2019).

1514

1515 **5.1.1 Mineral dust iron aerosol emissions**

1516 In Fig. 4 the high model estimates of total iron, compared to observations, downwind of North
1517 African mineral dust sources could be due to uncertainties in the magnitude of hematite emissions
1518 within the model. Hematite contains by far the largest fraction of iron of any mineral in MIMI
1519 (Table 3) with a major source in the Sahel (Fig. S45). The Sahel is a borderline dust source and

1520 emissions from this region have been shown to be sensitive to different model dynamics, even
1521 when forced with reanalysis winds, for example between CAM4 and CAM5 (Scanza et al., 2015).
1522 Other studies have shown a large sensitivity of dust generation to the details of the soil erodibility
1523 map (e.g., Cakmur et al., 2006). For CAM5 with the DEAD emissions scheme Scanza et al. (2015)
1524 showed that improvements in estimating the direct radiative forcing of mineral dust could be
1525 achieved by assuming that hematite is only emitted from clay minerals and not silt, an effective
1526 reduction of ~30% from the coarse mode emission of hematite. Although MIMI has employed an
1527 updated dust emission scheme (Table 1; Kok et al., 2014a) the model is still sensitive to
1528 assumptions within the offline minerology maps and applications of the brittle fragmentation
1529 theory therein. For instance, the single scattering albedo, which is a critical parameter in
1530 estimating the direct radiative forcing (e.g., Di Biagio et al., 2009), becomes more comparable to
1531 observations (Kim et al., 2011) if the same assumption as Scanza et al. (2015) is applied (Fig.
1532 S56). Quantifying the uncertainty on the climate response to different assumptions in minerology
1533 and dust emissions, and any reanalysis meteorology driving them, is therefore an important task.

1534

1535 **5.1.2 ~~Combustion~~ Pyrogenic iron aerosol emissions**

1536 Matsui et al. (2018) recently showed that combustion iron emissions have been underestimated
1537 in current models. One possible reason for this underestimate is that anthropogenic combustion
1538 iron emissions from Luo et al. (2008) are for 1996. Taking steelmaking and coal consumption
1539 (which are also linked to iron emissions) as a proxy for economic development (Ghosh, 2006; Lee
1540 and Chang, 2008) shows that growth in these sectors boomed exponentially post 2000,
1541 particularly in Asia and India (Ghosh, 2006; Lee and Chang, 2008). Therefore 1996 emissions
1542 are not capturing recent industrial developments and updating the anthropogenic combustion iron
1543 emission inventory for use in the 21st Century is a critical next step.

1544 During a fire, the iron contained in leaves and wood (Price, 1968) will be released to the
1545 atmosphere along with iron contained in the surrounding soil, whether entrained from the ground
1546 due to pyro-convective updrafts (Wagner et al., 2018) or a remobilization of terrigenous particles
1547 which have previously been deposited onto vegetation (Gaudichet et al., 1995; Paris et al., 2010).
1548 All sources are subsequently internally mixed within the smoke plume before any downwind
1549 observation occurs. Differentiating the iron contribution from the biomass which is burnt to that
1550 from the entrained dust was not considered in any of the studies in Table 4 but would be required
1551 to define the correct minerology and solubility of iron from fires. If we assume that biomass

1552 contains low concentrations of iron relative to the surrounding soils then we could expect a
1553 difference in observed Fe:BC ratios between a cerrado (savannah) environment, where
1554 surrounding soils are dry and dust is easily mobilized, compared to a tropical environment, where
1555 soils are wet, and dust is not as easily mobilized. But we do not see this in Table 4, and both
1556 regions have a similar range which spans around two orders of magnitude from low to high.
1557 However, no concrete conclusions can be drawn from such a limited dataset and so more
1558 observations are needed to distinguish which source (biomass or dust) is contributing most to the
1559 iron measured downwind of fires.

1560 The physical, chemical, and biological properties of the underlying soil are also impacted by fires
1561 (Certini, 2005) and it can be years after the fire has occurred before returning to a pre-fire state
1562 is achieved. For example, the removal of vegetation and the surface crust by fires from dune
1563 regions will create a new opportunity for dust mobilization (Strong et al., 2010) and higher intensity
1564 fires can also increase the erodibility of soils and availability of fine particles through breaking
1565 down the soil structure (Levin et al., 2012). Furthermore, under high temperatures the fire can
1566 transform the underlying soil mineralogy, with decreases to iron in clay minerals and increases in
1567 magnetic iron oxide ~~s~~ minerals (Crockford and Willett, 2001; Ketterings et al., 2000; Ulery and
1568 Graham, 1993). The amount of dust emitted from post-fire landscapes is potentially very
1569 significant with Wagenbrenner et al. (2017) estimating an extra 12-352 Tg of dust as PM₁₀ (40%
1570 of which was estimated to be PM_{2.5}) was emitted to the atmosphere in 2012 from post-fire
1571 landscapes in the western U.S. alone. The impact of fires on total and soluble iron emissions in
1572 dust from within post-burn regions is also likely to be different but requires further study, although
1573 likely depends on the fire regime and the time since the fire occurred.

1574 The most advanced iron processing models currently consider industrial, domestic, wildfires and
1575 shipping ~~combustion~~-pyrogenic emissions (Myriokefalitakis et al., 2018). An emerging discussion
1576 is the importance of volcanic ash, and the iron it contains, on ocean biogeochemistry (Langmann,
1577 2013). Figs. 4 through 7 showed that MIMI underrepresents both total iron and its solubility in the
1578 remote extra-tropical Pacific where volcanic emissions may be an important missing iron source.
1579 Future understanding in volcanic iron sources are potentially important as once deposited to the
1580 ocean, particularly in those regions that are iron limited or seasonally iron limited, volcanic inputs
1581 have been shown to alter satellite chlorophyll (Hamme et al., 2010; Rogan et al., 2016) and the
1582 drawdown of macronutrients (Lindenthal et al., 2013). The volume of metals released by a volcano
1583 is subject to many uncertainties, including both the nature of the volcano and its eruption type and
1584 strength; leading to estimates which can vary by many orders of magnitude (Mather et al., 2006,

1585 2012). To date most studies have focused on ocean inputs from shorter term explosive eruptions,
1586 rather than continuous inputs from quiescent passive degassing volcanoes which are likely to be
1587 most important only for the central Pacific region downwind of volcanoes located within the “ring
1588 of fire” (Olgun et al., 2011).

1589

1590 **5.2 Aerosol deposition**

1591 Examination of aerosol dry deposition in CAM5 by Wu et al (2018) showed that the deposition
1592 velocity for Aitken and accumulation sized BC particles is potentially an order of magnitude too
1593 high. It is highly likely that this will also be the case for dust. As the largest discrepancies between
1594 model and observations are in remote ocean regions improving the models long-range transport
1595 of iron by investigating deposition rates is an important constraint to be applied to the model.

1596

1597 **6. Conclusion**

1598 It is important to accurately model the atmospheric iron cycle because of the impacts of iron on
1599 human health, ocean biogeochemistry and climate. Atmospheric iron process modelling suitable
1600 for use in global climate and Earth system modelling is a new model development area, and as
1601 such currently undergoing rapid development. Here we have detailed the development of the
1602 Mechanism of Intermediate complexity for Modelling Iron (MIMI [v1.0](#)), such that it now represents
1603 iron emissions, atmospheric processing and deposition within a global modal aerosol
1604 microphysics framework.

1605 The solubility of iron depends on the underlying aerosol iron properties, such as dust mineralogy
1606 and combustion fuel type, and the degree to which dissolution from an insoluble to soluble iron
1607 form has occurred in the atmosphere. Which of these is the dominant factor for describing the
1608 observed inverse relationship between the solubility of iron to the total iron mass is currently
1609 unknown (Mahowald et al., 2018). Updating the mineral dust emission scheme to a physical
1610 based parametrisation however has improved model performance by increasing total iron close
1611 to mineral dust sources, where solubility is observed to be low (Figs. 4 through 7). Updating
1612 ~~combustion-pyrogenic iron~~ emissions from fires increases the long range transport of soluble iron
1613 to remote ocean regions, where observed solubility is higher (Figs. 4 through 7), while increasing
1614 [anthropogenic](#) combustion iron emissions by a factor of five brings the total in line with more
1615 recent evaluations of their magnitude (Conway et al., 2019; Matsui et al., 2018). Emission updates

1616 have also increased the variability in soluble iron deposition (Fig. 1415). Improvements to the
1617 atmospheric iron processing scheme in MIMI also increase iron dissolution in more remote
1618 regions relative to mineral dust sources, again in line with observations.

1619 Comparison with observations (Figs. 4 through 7) show that in general MIMI simulates total iron
1620 concentrations well. However, comparison of modelled iron solubility to observation reveals that
1621 while the model captures many regional features, some are missed. It is unclear, however,
1622 whether this problem arises from the model or observational representation of the system owing
1623 to the insufficient numbers of observations available to build a robust observational result for such
1624 a highly variable quantity in the Earth system, even when aggregating over small regional scales.
1625 There are significant differences in calculating iron solubility based on the order of the averaging
1626 operation. When calculating at each model time step global annual mean iron solubility is one-
1627 third (34%; NH=40%, SH=29%) higher than when calculated from monthly mean values. Earth-
1628 system models are designed to integrate land-atmosphere-ocean-ice components at each time-
1629 step and thus could yield different results based on the coupling time-step length employed. and
1630 Furthermore, the mean is shown to not be an accurate representation of the average atmospheric
1631 state, due to the non-Gaussian distribution of aerosol concentrations. In many regions however
1632 there are just a few (less than five) observations, and often only one, and so while the use of the
1633 median is robust with respect to extreme values, a limited observational dataset cannot truly
1634 discriminate if extreme values are outliers or, rather, the norm. Use of the mean also significantly
1635 overestimates the average atmospheric soluble iron deposition to the ocean and is always larger
1636 than the upper quartile of the distribution in daily deposition. However, this bias may be tempered
1637 due to ocean biogeochemistry processes likely being relevant over timescales which are longer
1638 than those in the atmosphere. Future work will need to consider how best to compare model to
1639 sporadic observations, potentially making use of distributions rather than a more limited absolute
1640 average.

1641 The main sources of soluble iron deposition vary both between and within ocean basin. The
1642 redefinition of ocean basins based on the dominant iron deposition source, rather than a
1643 traditional physio-geographical ocean basin, can therefore aid in determining where continental
1644 anthropogenic activity will have the greatest impact on ocean biogeochemistry and which source
1645 region is linked to where model-observation comparisons are poor. For example, modelling of
1646 total iron and its solubility in the South Atlantic could be improved by further improving our
1647 understanding of industrial combustion and fires within South America. Furthermore, soluble iron
1648 deposition to Southern Hemisphere oceans in MIMI, where combustion and fire emissions have

1649 a significant impact, is between a factor of two to four higher compared to BAM-Fe, itself the
1650 model simulating the largest atmospheric fluxes to the ocean of the comparable models studied
1651 in Myriokefalitakis et al. (2018). As integrated Earth system models develop in the future taking a
1652 holistic view to understanding how dust and fires are coupled, in terms of feedbacks on iron
1653 emissions, is an important step for predicting how future changes in climate will alter the climate
1654 and Earth system response to human perturbations of the natural system.

1655

1656 **Code and data availability**

1657 ~~Model C~~code (emissions and atmospheric processing for MIMI v1.0) and data is available at:
1658 <http://www.geo.cornell.edu/eas/PeoplePlaces/Faculty/mahowald/dust/Hamiltonetal2019/>

1659 ~~immediately from the corresponding author upon request and will be incorporated in a future~~
1660 ~~E3SM model release. Model data is available from the corresponding author upon request.~~

1661 Observational [iron](#) data is available from Mahowald et al. (2009) and Myriokefalitakis et al. (2018).

1662 [Observational oxalate data is available from Myriokefalitakis et al. \(2011\).](#)

1663

1664 **Author contributions**

1665 D.S.H. developed MIMI which incorporates model code previously developed by R.A.S., Y.F.,
1666 J.F.K., X.L., and M.W. D.S.H. undertook all model simulations and wrote the manuscript with
1667 support from N.M.M., J.G., and S.D.R.. D.S.H. prepared all Figures and Tables apart from Fig. 1
1668 and Table S1 (J.S.W.), Figs. [S23](#) and [S56](#) (L.L.), and Fig. 9 and [S42](#) (S.D.R.). All authors edited
1669 manuscript text.

1670

1671 **Acknowledgements**

1672 This work was supported by Department of Energy (DE) and National Science Foundation (NSF)
1673 grants for atmospheric deposition impacts on ocean biogeochemistry (DE-Sc0016362; NSF
1674 1049033; CCF-1522054). D.S.H. was also supported by the Atkinson Center for a Sustainable
1675 Future. J.F.K. acknowledges support from NSF grant 1552519. S.D.R. would like to thank the
1676 Collaborative Proposal Fire Dust Air and Water Improving Aerosol Biogeochemistry Interactions
1677 in ACME (DE-Sc0016321) in supporting his Masters. X.L. and M.W. would like to thank the
1678 support of NASA CloudSat and CALIPSO Science Program (grant NNX16AO94G). We would like
1679 to acknowledge high-performance computing support from Cheyenne ([doi:10.5065/D6RX99HX](https://doi.org/10.5065/D6RX99HX))
1680 provided by NCAR's Computational and Information Systems Laboratory, sponsored by the
1681 National Science Foundation.

1682

1683

1684

1685

1686

1687

1688 Achterberg, E. P., Moore, C. M., Henson, S. A., Steigenberger, S., Stohl, A., Eckhardt, S.,
1689 Avendano, L. C., Cassidy, M., Hembury, D., Klar, J. K., Lucas, M. I., Macey, A. I., Marsay, C. M.
1690 and Ryan-Keogh, Thomas, J.: Natural iron fertilisation by the Eyjafjallajokull volcanic eruption,
1691 *Geophys. Res. Lett.*, 40, 921–926, doi:10.1002/grl.50221, 2013.

1692 Akagi, S. K., Yokelson, R. J., Wiedinmyer, C., Alvarado, M. J., Reid, J. S., Karl, T., Crouse, J.
1693 D. and Wennberg, P. O.: Emission factors for open and domestic biomass burning for use in
1694 atmospheric models, *Atmos. Chem. Phys.*, 11(9), 4039–4072, doi:10.5194/acp-11-4039-2011,
1695 2011.

1696 Albani, S., Mahowald, N. M., Perry, A. T., Scanza, R. A., Zender, C. S., Heavens, N. G., Maggi,
1697 V., Kok, J. F. and Otto-Bliesner, B. L.: Improved dust representation in the Community
1698 Atmosphere Model, *J. Adv. Model. Earth Systems*, 6(3), 541–570,
1699 doi:10.1002/2013MS000279. Received, 2014.

1700 Andreae, M. O. and Crutzen, P. J.: Atmospheric Aerosols: Biogeochemical Sources and Role in
1701 Atmospheric Chemistry, *Science*, 276(5315), 1052–1058, doi:10.1126/science.276.5315.1052,
1702 1997.

1703 Arimoto, R.: Eolian dust and climate: relationships to sources, tropospheric chemistry, transport
1704 and deposition, *Earth-Science Rev.*, 54(1–3), 29–42, doi:10.1016/S0012-8252(01)00040-X,
1705 2001.

1706 Artaxo, P., Rizzo, L. V., Brito, J. F., Barbosa, H. M. J., Arana, A., Sena, E. T., Cirino, G. G.,
1707 Bastos, W., Martin, S. T. and Andreae, M. O.: Atmospheric aerosols in Amazonia and land use
1708 change: from natural biogenic to biomass burning conditions, *Faraday Discuss.*,
1709 doi:10.1039/c3fd00052d, 2013.

1710 Aumont, O., Ethé, C., Tagliabue, A., Bopp, L. and Gehlen, M.: PISCES-v2: An ocean
1711 biogeochemical model for carbon and ecosystem studies, *Geosci. Model Dev.*, 8(8), 2465–
1712 2513, doi:10.5194/gmd-8-2465-2015, 2015.

1713 Baker, A. R., Jickells, T. D., Biswas, K. F., Weston, K. and French, M.: Nutrients in atmospheric
1714 aerosol particles along the Atlantic Meridional Transect, *Deep Sea Res. Part II Top. Stud.*
1715 *Oceanogr.*, 53(14–16), 1706–1719, doi:10.1016/j.dsr2.2006.05.012, 2006a.

1716 Baker, A. R., Jickells, T. D., Witt, M. and Linge, K. L.: Trends in the solubility of iron, aluminium,
1717 manganese and phosphorus in aerosol collected over the Atlantic Ocean, *Mar. Chem.*, 98(1),
1718 43–58, doi:10.1016/j.marchem.2005.06.004, 2006b.

1719 Bates, T. S., Lamb, B. K., Guenther, A., Dignon, J. and Stoiber, R. E.: Sulfur Emissions to the
1720 Atmosphere from Natural Sources, *J. Atmos. Chem.*, 14, 315–337, 1992.

1721 Di Biagio, C., Di Sarra, A., Meloni, D., Monteleone, F., Piacentino, S. and Sferlazzo, D.:
1722 Measurements of Mediterranean aerosol radiative forcing and influence of the single scattering
1723 albedo, *J. Geophys. Res. Atmos.*, 114(6), 1–12, doi:10.1029/2008JD011037, 2009.

1724 Böke, H., Göktürk, E. H., Caner-Saltık, E. N. and Demirci, Ş.: Effect of airborne particle on
1725 SO₂–calcite reaction, *Appl. Surf. Sci.*, 140(1–2), 70–82, doi:10.1016/S0169-4332(98)00468-1,
1726 1999.

1727 Boyd, P. W., Jickells, T., Law, C. S., Blain, S., Boyle, E. A., Buesseler, K. O., Coale, K. H.,
1728 Cullen, J. J., Baar, H. J. W. De, Follows, M., Harvey, M., Lancelot, C., Levasseur, M., Owens, N.
1729 P. J., Pollard, R., Rivkin, R. B., Sarmiento, J., Schoemann, V., Smetacek, V., Takeda, S.,
1730 Tsuda, A., Turner, S. and Watson, A. J.: Mesoscale Iron Enrichment Experiments 1993 – 2005:
1731 Synthesis and Future Directions, *Science*, 315, 612–618, 2007.

1732 Bullard, J. E.: The distribution and biogeochemical importance of highlatitude dust in the Arctic
1733 and Southern Ocean- Antarctic regions, *J. Geophys. Res.*, 122(5), 3098–3103,
1734 doi:10.1002/2016JD026363, 2017.

1735 Bullard, J. E., Baddock, M., Bradwell, T., Crusius, J., Darlington, E., Gaiero, D., Gassó, S.,
1736 Gisladottir, G., Hodgkins, R., McCulloch, R., McKenna-Neuman, C., Mockford, T., Stewart, H.
1737 and Thorsteinsson, T.: High-latitude dust in the Earth system, *Rev. Geophys.*, 54(2), 447–485,
1738 doi:10.1002/2016RG000518, 2016.

1739 Cakmur, R. V., Miller, R. L., Perlwitz, J., Geogdzhayev, I. V., Ginoux, P., Koch, D., Kohfeld, K.
1740 E., Tegen, I. and Zender, C. S.: Constraining the magnitude of the global dust cycle by
1741 minimizing the difference between a model and observations, *J. Geophys. Res. Atmos.*, 111(6),
1742 1–24, doi:10.1029/2005JD005791, 2006.

1743 Capone, D., Zehr, J., Paerl, H., Bergman, B. and Carpenter, E.: Trichodesmium, a globally
1744 significant marine cyanobacterium, *Science (80-.)*, 276, 1221–1229, 1997.

1745 Certini, G.: Effects of fire on properties of forest soils: A review, *Oecologia*, 143(1), 1–10,
1746 doi:10.1007/s00442-004-1788-8, 2005.

1747 Chin, M. and Jacob, D. J.: Anthropogenic and natural contributions to tropospheric sulfate: A
1748 global model analysis, *J. Geophys. Res. Atmos.*, 101(D13), 18691–18699,

1749 doi:10.1029/96JD01222, 1996.

1750 Chuang, P. Y., Duvall, R. M., Shafer, M. M. and Schauer, J. J.: The origin of water soluble
1751 particulate iron in the Asian atmospheric outflow, *Geophys. Res. Lett.*, 32(7), 1–4,
1752 doi:10.1029/2004GL021946, 2005.

1753 Claquin, T., Schulz, M. and Balkanski, Y. J.: Modeling the Minerology of Atmospheric Dust
1754 Sources, *J. Geophys. Res. Res.*, 104(D18), 22243–22256, 1999.

1755 Computational and Information Systems Laboratory: Cheyenne: HPE/SGI ICE XA System
1756 (University Community Computing), Boulder, CO Natl. Cent. Atmos. Res.,
1757 doi:10.5065/D6RX99HX, 2017.

1758 Conway, T. M., Hamilton, D. S., Shelley, R. U., Aguilar-Islas, A. M., Landing, W. M., Mahowald,
1759 N. M. and John, S. G.: Tracing and constraining anthropogenic aerosol iron fluxes to the North
1760 Atlantic Ocean using iron isotopes, *Nat. Commun.*, 10(1), 1–10, doi:10.1038/s41467-019-
1761 10457-w, 2019.

1762 Cornell, R. and Schindler, P.: Photochemical dissolution of goethite in acid/oxalate solution,
1763 *Clays Clay Miner.*, 35(5), 347–352, doi:10.1346/CCMN.1987.0350504, 1987.

1764 Crockford, R. H. and Willett, I. R.: Application of mineral magnetism to describe profile
1765 development of toposequences of a sedimentary soil in south-eastern Australia, *Aust. J. Soil*
1766 *Res.*, 39(5), 927–949, doi:10.1071/SR00077, 2001.

1767 Crusius, J., Schroth, A. W., Gassó, S., Moy, C. M., Levy, R. C. and Gatica, M.: Glacial flour dust
1768 storms in the Gulf of Alaska: Hydrologic and meteorological controls and their importance as a
1769 source of bioavailable iron, *Geophys. Res. Lett.*, 38(L06602), 1–5, doi:10.1029/2010GL046573,
1770 2011.

1771 Dentener, F., Kinne, S., Bond, T., Boucher, O., Cofala, J., Generoso, S., Ginoux, P., Gong, S.,
1772 Hoelzemann, J. J., Ito, A., Marelli, L., Penner, J. E., Putaud, J.-P., Textor, C., Schultz, M., van
1773 der Werf, G. R. and Wilson, J.: Emissions of primary aerosol and precursor gases in the years
1774 2000 and 1750 prescribed data-sets for AeroCom, *Atmos. Chem. Phys.*, 6, 4321–4344, 2006.

1775 Duce, R. and Tindale, N.: Atmospheric transport of iron and its deposition in the ocean, *Limnol.*
1776 *Ocean.*, 36(8), 1715–1726, 1991.

1777 Facchini, M. C., Rinaldi, M., Decesari, S., Carbone, C., Finessi, E., Mircea, M., Fuzzi, S.,
1778 Ceburnis, D., Flanagan, R., Nilsson, E. D., de Leeuw, G., Martino, M., Woeltjen, J. and O’Dowd,

1779 C. D.: Primary submicron marine aerosol dominated by insoluble organic colloids and
1780 aggregates, *Geophys. Res. Lett.*, 35(17), 1–5, doi:10.1029/2008GL034210, 2008.

1781 Fanourgakis, G. S., Kanakidou, M., Nenes, A., Bauer, S. E., Bergman, T., Carslaw, K. S., Grini,
1782 A., Hamilton, D. S., Johnson, J. S., Karydis, V. A., Kirkevåg, A., Kodros, J. K., Lohmann, U.,
1783 Luo, G., Makkonen, R., Matsui, H., Neubauer, D., Pierce, J. R., Schmale, J., Stier, P.,
1784 Tsigaridis, K., van Noije, T., Wang, H., Watson-Parris, D., Westervelt, D. M., Yang, Y.,
1785 Yoshioka, M., Daskalakis, N., Decesari, S., Gysel-Beer, M., Kalivitis, N., Liu, X., Mahowald, N.
1786 M., Myriokefalitakis, S., Schrödner, R., Sfakianaki, M., Tsimpidi, A. P., Wu, M. and Yu, F.:
1787 Evaluation of global simulations of aerosol particle and cloud condensation nuclei number, with
1788 implications for cloud droplet formation, *Atmos. Chem. Phys.*, 19(13), 8591–8617,
1789 doi:10.5194/acp-19-8591-2019, 2019.

1790 Fung, I., Meyn, S. K., Tegen, I., Doney, S., John, J. and Bishop, J.: Iron supply and demand in
1791 the upper ocean, *Global Biogeochem. Cycles*, 14(1), 281–295, 2000.

1792 Gaudichet, A., Echalar, F., Chatenet, B., Quisefit, J. P., Malingre, G., Cachier, H., Buat-Menard,
1793 P., Artaxo, P. and Maenhaut, W.: Trace elements in tropical African savanna biomass burning
1794 aerosols, *J. Atmos. Chem.*, 22(1–2), 19–39, doi:10.1007/BF00708179, 1995.

1795 Gettelman, A., Liu, X., Ghan, S. J., Morrison, H., Park, S., Conley, A. J., Klein, S. A., Boyle, J.,
1796 Mitchell, D. L. and Li, J. L. F.: Global simulations of ice nucleation and ice supersaturation with
1797 an improved cloud scheme in the Community Atmosphere Model, *J. Geophys. Res. Atmos.*,
1798 115(18), 1–19, doi:10.1029/2009JD013797, 2010.

1799 Ghosh, S.: Steel consumption and economic growth: Evidence from India, *Resour. Policy*,
1800 31(1), 7–11, doi:10.1016/j.resourpol.2006.03.005, 2006.

1801 Giglio, L., Randerson, J. T. and van der Werf, G. R.: Analysis of daily, monthly, and annual
1802 burned area using the fourth-generation global fire emissions database (GFED4), *J. Geophys.*
1803 *Res. Biogeosciences*, 118(1), 317–328, doi:10.1002/jgrg.20042, 2013.

1804 Golaz, J., Caldwell, P. M., Roedel, L. P. Van, Petersen, M. R., Tang, Q., Wolfe, J. D., Abeshu,
1805 G., Anantharaj, V., Asay-davis, X. S., Bader, D. C., Baldwin, S. A., Bisht, G., Bogenschutz, P.
1806 A., Branstetter, M., Brunke, M. A., Brus, S. R., Burrows, S. M., Cameron-smith, P. J., Donahue,
1807 A. S., Deakin, M., Easter, R. C., Evans, K. J., Feng, Y., Flanner, M., Foucar, J. G., Fyke, J. G.,
1808 Hunke, E. C., Jacob, R. L., Jacobsen, D. W., Jeffery, N., Jones, P. W., Keen, N. D., Klein, S. A.,
1809 Larson, V. E., Leung, L. R., Li, H., Lin, W., Lipscomb, W. H., Ma, P., Mccoy, R. B., Neale, R. B.,

1810 Price, S. F., Qian, Y., Rasch, P. J., Eyre, J. E. J. R., Riley, W. J., Ringler, T. D., Roberts, A. F.,
1811 Roesler, E. L., Salinger, A. G., Shaheen, Z., Shi, X., Singh, B., Veneziani, M., Wan, H., Wang,
1812 H., Wang, S., Williams, D. N., Wolfram, P. J., Worley, P. H., Xie, S., Yang, Y., Yoon, J.-H.,
1813 Zelinka, M. D., Zender, C. S., Zeng, X., Zhang, C., Zhang, K., Zhang, Y., Zheng, X., Zhou, T.
1814 and Zhu, Q.: The DOE E3SM Coupled Model Version 1 : Overview and Evaluation at Standard
1815 Resolution, *J. Adv. Model. Earth Systms*, 11, 1–41, doi:10.1029/2018MS001603, 2019.

1816 Gregg, W. W., Conkright, M. E., Ginoux, P., O'Reilly, J. E. and Casey, N. W.: Ocean primary
1817 production and climate: Global decadal changes, *Geophys. Res. Lett.*, 30(15), 10–13,
1818 doi:10.1029/2003GL016889, 2003.

1819 Guieu, C., Bonnet, S., Wagener, T. and Loÿe-Pilot, M. D.: Biomass burning as a source of
1820 dissolved iron to the open ocean?, *Geophys. Res. Lett.*, 32(L19608), 1–5,
1821 doi:10.1029/2005GL022962, 2005.

1822 Guieu, C., Aumont, O., Paytan, A., Bopp, L., Law, C. S., Mahowald, N., Achterberg, E. P.,
1823 Marañón, E., Salihoglu, B., Crise, A., Wagener, T., Herut, B., Desboeufs, K., Kanakidou, M.,
1824 Olgun, N., Peters, F., Völker, C., Aumont, O., Paytan, A., Bopp, L., Law, C. S., Mahowald, N.,
1825 Achterberg, E. P., Marañón, E., Salihoglu, B., Crise, A., Wagener, T., Herut, B., Desboeufs, K.,
1826 Kanakidou, M., Olgun, N., Peters, F. and Völker, C.: Global Biogeochemical Cycles deposition
1827 to Low Nutrient Low Chlorophyll regions, *Global Biogeochem. Cycles*, 28, 1179–1198,
1828 doi:10.1002/2014GB004852.Received, 2014.

1829 Hamme, R., Webley, P., Crawford, W., Whitney, F., DeGrandpre, M., Emerson, S., Eriksen, C.,
1830 Giesbrecht, K., Gower, J., Kavanaugh, M., Peña, M., Sabine, C., Batten, S., Coogan, L.,
1831 Grundle, D. and Lockwood, D.: Volcanic ash fuels anomalous plankton bloom in subarctic
1832 northeast Pacific, *Geophys. Res. Lett.*, 37(L19604), 1–5, doi:10.1029/2010GL044629, 2010.

1833 Holben, B. N., Eck, T. F., Slutsker, I., Tanre, D., Cimel, J. P. B., Vermote, E., Reagan, J. A.,
1834 Kaufman, Y. J., Nakajima, T., Lavenu, F., Jankowiak, I. and Smirnov, A.: AERONET-A
1835 Federated Instrument Network and Data Archeive for Aerosol Characterization, 2000.

1836 Hu, M., Peng, J., Sun, K., Yue, D., Guo, S., Wiedensohler, A. and Wu, Z.: Estimation of size-
1837 resolved ambient particle density based on the measurement of aerosol number, mass, and
1838 chemical size distributions in the winter in Beijing, *Environ. Sci. Technol.*, 46(18), 9941–9947,
1839 doi:10.1021/es204073t, 2012.

1840 Huneus, N., Schulz, M., Balkanski, Y., Griesfeller, J., Prospero, J., Kinne, S., Bauer, S.,

1841 Boucher, O., Chin, M., Dentener, F., Diehl, T., Easter, R., Fillmore, D., Ghan, S., Ginoux, P.,
1842 Grini, A., Horowitz, L., Koch, D., Krol, M. C., Landing, W., Liu, X., Mahowald, N., Miller, R.,
1843 Morcrette, J.-J., Myhre, G., Penner, J., Perlwitz, J., Stier, P., Takemura, T. and Zender, C. S.:
1844 Global dust model intercomparison in AeroCom phase I, *Atmos. Chem. Phys.*, 11(15), 7781–
1845 7816, doi:10.5194/acp-11-7781-2011, 2011.

1846 Ingall, E., Feng, Y., Longo, A., Lai, B., Landing, W., Shelley, R., Morton, P., Nenes, A., Violaki,
1847 K., Gao, Y., Sahai, S. and Castorina, E.: Enhanced Iron Solubility at Low pH in Global Aerosols,
1848 *Atmosphere (Basel)*, 9(5), 201, doi:10.3390/atmos9050201, 2018.

1849 Ito, A.: Global modeling study of potentially bioavailable iron input from shipboard aerosol
1850 sources to the ocean, *Global Biogeochem. Cycles*, 27(1), 1–10, doi:10.1029/2012GB004378,
1851 2013.

1852 Ito, A.: Atmospheric processing of combustion aerosols as a source of bioavailable iron,
1853 *Environ. Sci. Technol. Lett.*, 2(3), 70–75, doi:10.1021/acs.estlett.5b00007, 2015.

1854 Ito, A. and Xu, L.: Response of acid mobilization of iron-containing mineral dust to improvement
1855 of air quality projected in the future, *Atmos. Chem. Phys.*, 14(7), 3441–3459, doi:10.5194/acp-
1856 14-3441-2014, 2014.

1857 Ito, A., Myriokefalitakis, S., Kanakidou, M., Mahowald, N. M., Scanza, R. A., Hamilton, D. S.,
1858 Baker, A. R., Jickells, T., Sarin, M., Bikkina, S., Gao, Y., Shelley, R. U., Buck, C. S., Landing, W.
1859 M., Bowie, A. R., Perron, M. M. G., Guieu, C., Meskhidze, N., Johnson, M. S., Feng, Y., Kok, J.
1860 F., Nenes, A. and Duce, R. A.: Pyrogenic iron: The missing link to high iron solubility in
1861 aerosols, *Sci. Adv.*, 5(5), 1–10, doi:10.1126/sciadv.aau7671, 2019.

1862 Jickells, T., Boyd, P. and Hunter, K.: Biogeochemical impacts of dust on the global carbon cycle,
1863 in *Mineral Dust: A Key player in the Earth System*, edited by P. Knippertz and J.-B. Stett, pp.
1864 284–359, Springer Science+ Business Media, Dordrecht., 2014.

1865 Jickells, T. D., An, Z. S., Andersen, K. K., Baker, a R., Bergametti, G., Brooks, N., Cao, J. J.,
1866 Boyd, P. W., Duce, R. a, Hunter, K. a, Kawahata, H., Kubilay, N., LaRoche, J., Liss, P. S.,
1867 Mahowald, N., Prospero, J. M., Ridgwell, a J., Tegen, I. and Torres, R.: Global iron connections
1868 between desert dust, ocean biogeochemistry, and climate., *Science*, 308(5718), 67–71,
1869 doi:10.1126/science.1105959, 2005.

1870 Johnson, M. S. and Meskhidze, N.: Atmospheric dissolved iron deposition to the global oceans:
1871 Effects of oxalate-promoted Fe dissolution, photochemical redox cycling, and dust mineralogy,

- 1872 Geosci. Model Dev., 6(4), 1137–1155, doi:10.5194/gmd-6-1137-2013, 2013.
- 1873 Journet, E., Desbouefs, K., Caquineau, S. and Colin, J.-L.: Mineralogy as a critical factor of dust
1874 iron solubility, Geophys. Res. Lett., 35(L07805), doi:10.1029/2007GL031589, 2008.
- 1875 Kanakidou, M., Seinfeld, J. H., Pandis, S. N., Barnes, I., Dentener, F. J., Facchini, M. C., Van
1876 Dingenen, R., Ervens, B., Nenes, A., Nielsen, C. J., Swietlicki, E., Putaud, J. P., Balkanski, Y.,
1877 Fuzzi, S., Horth, J., Moortgat, G. K., Winterhalter, R., Myhre, C. E. L., Tsigaridis, K., Vignati, E.,
1878 Stephanou, E. G. and Wilson, J.: Organic aerosol and global climate modelling: a review,
1879 Atmos. Chem. Phys., 5(4), 1053–1123, doi:10.5194/acp-5-1053-2005, 2005.
- 1880 Ketterings, Q. M., Bigham, J. M. and Laperche, V.: Changes in Soil Mineralogy and Texture
1881 Caused by Slash-and-Burn Fires in Sumatra, Indonesia, Soil Sci. Soc. Am. J., 64(3), 1108–
1882 1117, doi:10.2136/sssaj2000.6431108x, 2000.
- 1883 Kim, D., Chin, M., Yu, H., Eck, T. F., Sinyuk, A., Smirnov, A. and Holben, B. N.: Dust optical
1884 properties over North Africa and Arabian Peninsula derived from the AERONET dataset, Atmos.
1885 Chem. Phys., 11(20), 10733–10741, doi:10.5194/acp-11-10733-2011, 2011.
- 1886 Kok, J. F.: A scaling theory for the size distribution of emitted dust aerosols suggests climate
1887 models underestimate the size of the global dust cycle, Proc. Natl. Acad. Sci., 108(3), 1016–
1888 1021, doi:10.1073/pnas.1014798108, 2011.
- 1889 Kok, J. F., Mahowald, N. M., Fratini, G., Gillies, J. A., Ishizuka, M., Leys, J. F., Mikami, M., Park,
1890 M. S., Park, S. U., Van Pelt, R. S. and Zobeck, T. M.: An improved dust emission model - Part
1891 1: Model description and comparison against measurements, Atmos. Chem. Phys., 14(23),
1892 13023–13041, doi:10.5194/acp-14-13023-2014, 2014a.
- 1893 Kok, J. F., Albani, S., Mahowald, N. M. and Ward, D. S.: An improved dust emission model -
1894 Part 2: Evaluation in the Community Earth System Model, with implications for the use of dust
1895 source functions, Atmos. Chem. Phys., 14(23), 13043–13061, doi:10.5194/acp-14-13043-2014,
1896 2014b.
- 1897 Kok, J. F., Ridley, D. A., Zhou, Q., Miller, R. L., Zhao, C., Heald, C. L., Ward, D. S., Albani, S.
1898 and Haustein, K.: Smaller desert dust cooling effect estimated from analysis of dust size and
1899 abundance, Nat. Geosci., 10(4), 274–278, doi:10.1038/ngeo2912, 2017.
- 1900 Lamarque, J.-F., Bond, T. C., Eyring, V., Granier, C., Heil, A., Klimont, Z., Lee, D., Liousse, C.,
1901 Mieville, A., Owen, B., Schultz, M. G., Shindell, D., Smith, S. J., Stehfest, E., Van Aardenne, J.,

1902 Cooper, O. R., Kainuma, M., Mahowald, N., McConnell, J. R., Naik, V., Riahi, K. and van
1903 Vuuren, D. P.: Historical (1850–2000) gridded anthropogenic and biomass burning emissions of
1904 reactive gases and aerosols: methodology and application, *Atmos. Chem. Phys.*, 10(15), 7017–
1905 7039, doi:10.5194/acp-10-7017-2010, 2010.

1906 Langmann, B.: Volcanic Ash versus Mineral Dust: Atmospheric Processing and Environmental
1907 and Climate Impacts, *ISRN Atmos. Sci.*, Article ID, 1–17, doi:10.1155/2013/245076, 2013.

1908 Langmann, B., Zakšek, K., Hort, M. and Duggen, S.: Volcanic ash as fertiliser for the surface
1909 ocean, *Atmos. Chem. Phys.*, 10, 3891–3899, 2010.

1910 Lee, C. C. and Chang, C. P.: Energy consumption and economic growth in Asian economies: A
1911 more comprehensive analysis using panel data, *Resour. Energy Econ.*, 30(1), 50–65,
1912 doi:10.1016/j.reseneeco.2007.03.003, 2008.

1913 Levin, N., Levental, S. and Morag, H.: The effect of wildfires on vegetation cover and dune
1914 activity in Australia’s desert dunes: A multisensor analysis, *Int. J. Wildl. Fire*, 21(4), 459–475,
1915 doi:10.1071/WF10150, 2012.

1916 Li, F., Koopal, L. and Tan, W.: Roles of different types of oxalate surface complexes in
1917 dissolution process of ferrihydrite aggregates, *Sci. Rep.*, 8(1), 1–13, doi:10.1038/s41598-018-
1918 20401-5, 2018.

1919 Lindenthal, A., Langmann, B., Pätzsch, J., Lorkowski, I. and Hort, M.: The ocean response to
1920 volcanic iron fertilisation after the eruption of Kasatochi volcano: A regional-scale
1921 biogeochemical ocean model study, *Biogeosciences*, 10(6), 3715–3729, doi:10.5194/bg-10-
1922 3715-2013, 2013.

1923 Liu, X., Easter, R. C., Ghan, S. J., Zaveri, R., Rasch, P., Shi, X., Lamarque, J. F., Gettelman, A.,
1924 Morrison, H., Vitt, F., Conley, A., Park, S., Neale, R., Hannay, C., Ekman, A. M. L., Hess, P.,
1925 Mahowald, N., Collins, W., Iacono, M. J., Bretherton, C. S., Flanner, M. G. and Mitchell, D.:
1926 Toward a minimal representation of aerosols in climate models: Description and evaluation in
1927 the Community Atmosphere Model CAM5, *Geosci. Model Dev.*, 5(3), 709–739,
1928 doi:10.5194/gmd-5-709-2012, 2012.

1929 Liu, X., Ma, P. L., Wang, H., Tilmes, S., Singh, B., Easter, R. C., Ghan, S. J. and Rasch, P. J.:
1930 Description and evaluation of a new four-mode version of the Modal Aerosol Module (MAM4)
1931 within version 5.3 of the Community Atmosphere Model, *Geosci. Model Dev.*, 9(2), 505–522,
1932 doi:10.5194/gmd-9-505-2016, 2016.

1933 Longo, A. F., Feng, Y., Lai, B., Landing, W. M., Shelley, R. U., Nenes, A., Mihalopoulos, N.,
1934 Violaki, K. and Ingall, E. D.: Influence of Atmospheric Processes on the Solubility and
1935 Composition of Iron in Saharan Dust, *Environ. Sci. Technol.*, 50(13), 6912–6920,
1936 doi:10.1021/acs.est.6b02605, 2016.

1937 Luo, C., Mahowald, N., Bond, T., Chuang, P. Y., Artaxo, P., Siefert, R., Chen, Y. and Schauer,
1938 J.: Combustion iron distribution and deposition, *Global Biogeochem. Cycles*, 22(GB1012), 1–17,
1939 doi:10.1029/2007GB002964, 2008.

1940 Mahowald, N.: Aerosol indirect effect on biogeochemical cycles and climate., *Science*,
1941 334(6057), 794–6, doi:10.1126/science.1207374, 2011.

1942 Mahowald, N., Jickells, T. D., Baker, A. R., Artaxo, P., Benitez-Nelson, C. R., Bergametti, G.,
1943 Bond, T. C., Chen, Y., Cohen, D. D., Herut, B., Kubilay, N., Losno, R., Luo, C., Maenhaut, W.,
1944 McGee, K. A., Okin, G. S., Siefert, R. L. and Tsukuda, S.: Global distribution of atmospheric
1945 phosphorus sources, concentrations and deposition rates, and anthropogenic impacts, *Global*
1946 *Biogeochem. Cycles*, 22(4), 1–19, doi:10.1029/2008GB003240, 2008.

1947 Mahowald, N. M., Engelstaedter, S., Luo, C., Sealy, A., Artaxo, P., Benitez-Nelson, C., Bonnet,
1948 S., Chen, Y., Chuang, P. Y., Cohen, D. D., Dulac, F., Herut, B., Johansen, A. M., Kubilay, N.,
1949 Losno, R., Maenhaut, W., Paytan, A., Prospero, J. M., Shank, L. M. and Siefert, R. L.:
1950 Atmospheric iron deposition: global distribution, variability, and human perturbations., *Ann. Rev.*
1951 *Mar. Sci.*, 245–278, doi:10.1146/annurev.marine.010908.163727, 2009.

1952 Mahowald, N. M., Scanza, R., Brahney, J., Goodale, C. L., Hess, P. G., Moore, J. K. and Neff,
1953 J.: Aerosol Deposition Impacts on Land and Ocean Carbon Cycles, *Curr. Clim. Chang. Reports*,
1954 3(1), 16–31, doi:10.1007/s40641-017-0056-z, 2017.

1955 Mahowald, N. M., Hamilton, D. S., Mackey, K. R. M., Moore, J. K., Baker, A. R., Scanza, R. A.
1956 and Zhang, Y.: Aerosol trace metal leaching and impacts on marine microorganisms, *Nat.*
1957 *Commun.*, 9(1), doi:10.1038/s41467-018-04970-7, 2018.

1958 Mann, G. W., Carslaw, K. S., Reddington, C. L., Pringle, K. J., Schulz, M., Asmi, A., Spracklen,
1959 D. V., Ridley, D. a., Woodhouse, M. T., Lee, L. a., Zhang, K., Ghan, S. J., Easter, R. C., Liu, X.,
1960 Stier, P., Lee, Y. H., Adams, P. J., Tost, H., Lelieveld, J., Bauer, S. E., Tsigaridis, K., van Noije,
1961 T. P. C., Strunk, A., Vignati, E., Bellouin, N., Dalvi, M., Johnson, C. E., Bergman, T., Kokkola,
1962 H., von Salzen, K., Yu, F., Luo, G., Petzold, A., Heintzenberg, J., Clarke, A., Ogren, J. a., Gras,
1963 J., Baltensperger, U., Kaminski, U., Jennings, S. G., O'Dowd, C. D., Harrison, R. M., Beddows,

1964 D. C. S., Kulmala, M., Viisanen, Y., Ulevicius, V., Mihalopoulos, N., Zdimal, V., Fiebig, M.,
1965 Hansson, H.-C., Swietlicki, E. and Henzing, J. S.: Intercomparison and evaluation of global
1966 aerosol microphysical properties among AeroCom models of a range of complexity, *Atmos.*
1967 *Chem. Phys.*, 14(9), 4679–4713, doi:10.5194/acp-14-4679-2014, 2014.

1968 Martin, H., Gordon, R. M. and Fitzwater, S. E.: The case for iron, *Limnol. Ocean.*, 36(8), 1793–
1969 1802, 1991.

1970 Martin, J.: Glacial-interglacial CO₂ change: The iron hypothesis, *Paleoceanography*, 5(1), 1–13,
1971 1990.

1972 Mather, T. A., Pyle, D. M., Tsanev, V. I., McGonigle, A. J. S., Oppenheimer, C. and Allen, A. G.:
1973 A reassessment of current volcanic emissions from the Central American arc with specific
1974 examples from Nicaragua, *J. Volcanol. Geotherm. Res.*, 149(3–4), 297–311,
1975 doi:10.1016/j.jvolgeores.2005.07.021, 2006.

1976 Mather, T. A., Witt, M. L. I., Pyle, D. M., Quayle, B. M., Aiuppa, A., Bagnato, E., Martin, R. S.,
1977 Sims, K. W. W., Edmonds, M., Sutton, A. J. and Ilyinskaya, E.: Halogens and trace metal
1978 emissions from the ongoing 2008 summit eruption of Kīlauea volcano, Hawaii, *Geochim.*
1979 *Cosmochim. Acta*, 83, 292–323, doi:10.1016/j.gca.2011.11.029, 2012.

1980 Matsui, H., Mahowald, N. M., Moteki, N., Hamilton, D. S., Ohata, S., Yoshida, A., Koike, M.,
1981 Scanza, R. A. and Flanner, M. G.: Anthropogenic combustion iron as a complex climate forcer,
1982 *Nat. Commun.*, 9(1), doi:10.1038/s41467-018-03997-0, 2018.

1983 Menut, L., Bessagnet, B., Colette, A. and Khvorostiyannov, D.: On the impact of the vertical
1984 resolution on chemistry-transport modelling, *Atmos. Environ.*, 67, 370–384,
1985 doi:10.1016/j.atmosenv.2012.11.026, 2013.

1986 Meskhidze, N., Chameides, W. L., Nenes, A. and Chen, G.: Iron mobilization in mineral dust:
1987 Can anthropogenic SO₂ emissions affect ocean productivity?, *Geophys. Res. Lett.*, 30(21),
1988 2085, doi:10.1029/2003GL018035, 2003.

1989 Meskhidze, N., Chameides, W. L. and Nenes, A.: Dust and pollution: A recipe for enhanced
1990 ocean fertilization?, *J. Geophys. Res. Atmos.*, 110(D03301), 1–23, doi:10.1029/2004JD005082,
1991 2005.

1992 Moore, C. M. M., Mills, M. M. M., Arrigo, K. R. R., Berman-Frank, I., Bopp, L., Boyd, P. W. W.,
1993 Galbraith, E. D. D., Geider, R. J. J., Guieu, C., Jaccard, S. L. L., Jickells, T. D. D., La Roche, J.,

1994 Lenton, T. M. M., Mahowald, N. M. M., Marañón, E., Marinov, I., Moore, J. K. K., Nakatsuka, T.,
1995 Oschlies, A., Saito, M. A. A., Thingstad, T. F. F., Tsuda, A. and Ulloa, O.: Processes and
1996 patterns of oceanic nutrient limitation, *Nat. Geosci.*, 6(9), 701–710, doi:10.1038/ngeo1765,
1997 2013.

1998 Moore, J. K., Doney, S. C. and Lindsay, K.: Upper ocean ecosystem dynamics and iron cycling
1999 in a global three-dimensional model, *Global Biogeochem. Cycles*, 18(4), 1–21,
2000 doi:10.1029/2004GB002220, 2004.

2001 Moore, K., Doney, S. C., Lindsay, K., Mahowald, N. and Michaels Anthony F., A. F.: Nitrogen
2002 fixation amplifies the ocean biogeochemical response to decadal timescale variations in mineral
2003 dust deposition, *Tellus, Ser. B Chem. Phys. Meteorol.*, 58(5), doi:10.1111/j.1600-
2004 0889.2006.00209.x, 2006.

2005 Morrison, H. and Gettelman, A.: A new two-moment bulk stratiform cloud microphysics scheme
2006 in the community atmosphere model, version 3 (CAM3). Part I: Description and numerical tests,
2007 *J. Clim.*, 21(15), 3642–3659, doi:10.1175/2008JCLI2105.1, 2008.

2008 Myriokefalitakis, S., Tsigaridis, K., Mihalopoulos, N., Sciare, J., Nenes, A., Kawamura, K.,
2009 Segers, A. and Kanakidou, M.: In-cloud oxalate formation in the global troposphere: A 3-D
2010 modeling study, *Atmos. Chem. Phys.*, 11(12), 5761–5782, doi:10.5194/acp-11-5761-2011,
2011 2011.

2012 Myriokefalitakis, S., Daskalakis, N., Mihalopoulos, N., Baker, A. R., Nenes, A. and Kanakidou,
2013 M.: Changes in dissolved iron deposition to the oceans driven by human activity: a 3-D global
2014 modelling study, *Biogeosciences*, 12(13), 3973–3992, doi:10.5194/bg-12-3973-2015, 2015.

2015 Myriokefalitakis, S., Ito, A., Kanakidou, M., Nenes, A., Krol, M. C., Mahowald, N. M., Scanza, R.
2016 A., Hamilton, D. S., Johnson, M. S., Meskhidze, N., Kok, J. F., Guieu, C., Baker, A. R., Jickells,
2017 T. D., Sarin, M. M., Bikkina, S., Shelley, R., Bowie, A., Perron, M. M. G. and Duce, R. A.:
2018 Reviews and syntheses: The GESAMP atmospheric iron deposition model intercomparison
2019 study, *Biogeosciences*, 15(21), 6659–6684, doi:10.5194/bg-15-6659-2018, 2018.

2020 Neale, R. B., Chen, C. C., Gettelman, A., Lauritzen, P. H., Park, S., Williamson, D. L., Conley,
2021 A. J., Garcia, R., Kinnison, D., Lamarque, J. F., Marsh, D., Mills, M., Smith, A. K., Tilmes, S.,
2022 Vitt, F., Morrison, H., Cameron-Smith, P., Collins, W. D., Iacono, M. J., Easter, R. C., Ghan, S.
2023 J., Liu, X., Rasch, P. J. and Taylor, M. A.: Description of the NCAR Community Atmosphere
2024 Model (CAM 5.0)., 2010.

2025 O'Dowd, C. D. and de Leeuw, G.: Marine aerosol production: a review of the current knowledge,
2026 Philos. Trans. R. Soc. A Math. Phys. Eng. Sci., 365(1856), 1753–1774,
2027 doi:10.1098/rsta.2007.2043, 2007.

2028 Oakes, M., Ingall, E. D., Lai, B., Shafer, M. M., Hays, M. D., Liu, Z. G., Russell, A. G. and
2029 Weber, R. J.: Iron solubility related to particle sulfur content in source emission and ambient fine
2030 particles, Environ. Sci. Technol., 46(12), 6637–6644, doi:10.1021/es300701c, 2012.

2031 Olgun, N., Duggen, S., Croot, P. L., Delmelle, P., Dietze, H., Schacht, U., Óskarsson, N., Siebe,
2032 C., Auer, A. and Garbe-Schönberg, D.: Surface ocean iron fertilization: The role of airborne
2033 volcanic ash from subduction zone and hot spot volcanoes and related iron fluxes into the
2034 Pacific Ocean, Global Biogeochem. Cycles, 25(GB4001), 1–15, doi:10.1029/2009GB003761,
2035 2011.

2036 Pantias, D., Taxiarchou, M., Paspaliaris, I. and Kontopoulos, A.: Mechanisms of dissolution of
2037 iron oxides in aqueous oxalions, Hydrometallurgy, 42(95), 257–265, 1996.

2038 Paris, R., Desboeufs, K. V., Formenti, P., Nava, S. and Chou, C.: Chemical characterisation of
2039 iron in dust and biomass burning aerosols during AMMA-SOP0/DABEX: Implication for iron
2040 solubility, Atmos. Chem. Phys., 10(9), 4273–4282, doi:10.5194/acp-10-4273-2010, 2010.

2041 Paris, R., Desboeufs, K. V. and Journet, E.: Variability of dust iron solubility in atmospheric
2042 waters: Investigation of the role of oxalate organic complexation, Atmos. Environ., 45(36),
2043 6510–6517, doi:10.1016/j.atmosenv.2011.08.068, 2011.

2044 Perlwitz, J. P., Pérez García-Pando, C. and Miller, R. L.: Predicting the mineral composition of
2045 dust aerosols - Part 1: Representing key processes, Atmos. Chem. Phys., 15(20), 11593–
2046 11627, doi:10.5194/acp-15-11593-2015, 2015a.

2047 Perlwitz, J. P., Pérez García-Pando, C. and Miller, R. L.: Predicting the mineral composition of
2048 dust aerosols - Part 2: Model evaluation and identification of key processes with observations,
2049 Atmos. Chem. Phys., 15(20), 11629–11652, doi:10.5194/acp-15-11629-2015, 2015b.

2050 Price, C. A.: Iron compounds and plant nutrition, Annu. Rev. Plant Physiol., 19, 239–248, 1968.

2051 Reddington, C. L., Spracklen, D. V., Artaxo, P., Ridley, D. A., Rizzo, L. V. and Arana, A.:
2052 Analysis of particulate emissions from tropical biomass burning using a global aerosol model
2053 and long-term surface observations, Atmos. Chem. Phys., 16(17), 11083–11106,
2054 doi:10.5194/acp-16-11083-2016, 2016.

2055 Rémy, S., Veira, A., Paugam, R., Sofiev, M., Kaiser, J. W., Marengo, F., Burton, S. P.,
2056 Benedetti, A., Engelen, R. J., Ferrare, R. and Hair, J. W.: Two global data sets of daily fire
2057 emission injection heights since 2003, *Atmos. Chem. Phys.*, 17(4), 2921–2942,
2058 doi:10.5194/acp-17-2921-2017, 2017.

2059 Ridley, D. A., Heald, C. L., Kok, J. F. and Zhao, C.: An observationally constrained estimate of
2060 global dust aerosol optical depth, *Atmos. Chem. Phys.*, 16(23), 15097–15117, doi:10.5194/acp-
2061 16-15097-2016, 2016.

2062 Rogan, N., Achterberg, E. P., Le Moigne, F. A. C., Marsay, C. M., Tagliabue, A. and Williams,
2063 R. G.: Volcanic ash as an oceanic iron source and sink, *Geophys. Res. Lett.*, 43(6), 2732–2740,
2064 doi:10.1002/2016GL067905, 2016.

2065 Scanza, R. A., Mahowald, N., Ghan, S., Zender, C. S., Kok, J. F., Liu, X., Zhang, Y. and Albani,
2066 S.: Modeling dust as component minerals in the Community Atmosphere Model: Development
2067 of framework and impact on radiative forcing, *Atmos. Chem. Phys.*, 15(1), 537–561,
2068 doi:10.5194/acp-15-537-2015, 2015.

2069 Scanza, R. A., Hamilton, D. S., Perez Garcia-Pando, C., Buck, C., Baker, A. and Mahowald, N.
2070 M.: Atmospheric Processing of Iron in Mineral and Combustion Aerosols: Development of an
2071 Intermediate-Complexity Mechanism Suitable for Earth System Models, *Atmos. Chem. Phys.*,
2072 18, 14175–14196, doi:10.5194/acp-18-14175-80, 2018.

2073 Schroth, A. W., Crusius, J., Sholkovitz, E. R. and Bostick, B. C.: Iron solubility driven by
2074 speciation in dust sources to the ocean, *Nat. Geosci.*, 2(5), 337–340, doi:10.1038/ngeo501,
2075 2009.

2076 Schutgens, N., Tsyro, S., Gryspeerdt, E., Goto, D., Weigum, N., Schulz, M. and Stier, P.: On the
2077 spatio-temporal representativeness of observations, *Atmos. Chem. Phys.*, 17(16), 9761–9780,
2078 doi:10.5194/acp-17-9761-2017, 2017.

2079 Shi, Z., Krom, M. D., Jickells, T. D., Bonneville, S., Carslaw, K. S., Mihalopoulos, N., Baker, A.
2080 R. and Benning, L. G.: Impacts on iron solubility in the mineral dust by processes in the source
2081 region and the atmosphere: A review, *Aeolian Res.*, 5(May), 21–42,
2082 doi:10.1016/j.aeolia.2012.03.001, 2012.

2083 Shoenfelt, E. M., Sun, J., Winckler, G., Kaplan, M. R., Borunda, A. L., Farrell, K. R., Moreno, P.
2084 I., Gaiero, D. M., Recasens, C., Sambrotto, R. N. and Bostick, B. C.: High particulate iron(II)
2085 content in glacially sourced dusts enhances productivity of a model diatom, *Sci. Adv.*, 3(6), 1–

2086 10, doi:10.1126/sciadv.1700314, 2017.

2087 Sholkovitz, E. R., Sedwick, P. N., Church, T. M., Baker, A. R. and Powell, C. F.: Fractional
2088 solubility of aerosol iron: Synthesis of a global-scale data set, *Geochim. Cosmochim. Acta*, 89,
2089 173–189, doi:10.1016/j.gca.2012.04.022, 2012.

2090 Smith, M. B., Mahowald, N. M., Albani, S., Perry, A., Losno, R., Qu, Z., Marticorena, B., Ridley,
2091 D. A. and Heald, C. L.: Sensitivity of the interannual variability of mineral aerosol simulations to
2092 meteorological forcing dataset, *Atmos. Chem. Phys.*, 17(5), 3253–3278, doi:10.5194/acp-17-
2093 3253-2017, 2017.

2094 Sofiev, M., Ermakova, T. and Vankevich, R.: Evaluation of the smoke-injection height from wild-
2095 land fires using remote-sensing data, *Atmos. Chem. Phys.*, 12(4), 1995–2006, doi:10.5194/acp-
2096 12-1995-2012, 2012.

2097 Solmon, F., Chuang, P. Y., Meskhidze, N. and Chen, Y.: Acidic processing of mineral dust iron
2098 by anthropogenic compounds over the north Pacific Ocean, *J. Geophys. Res.*, 114(D2),
2099 D02305, doi:10.1029/2008JD010417, 2009.

2100 Strong, C. L., Bullard, J. E., Dubois, C., McTainsh, G. H. and Baddock, M. C.: Impact of wildfire
2101 on interdune ecology and sediments: An example from the Simpson Desert, Australia, *J. Arid
2102 Environ.*, 74(11), 1577–1581, doi:10.1016/j.jaridenv.2010.05.032, 2010.

2103 Teixeira, J. C., Carvalho, A. C., Tuccella, P., Curci, G. and Rocha, A.: WRF-chem sensitivity to
2104 vertical resolution during a saharan dust event, *Phys. Chem. Earth*, 94, 188–195,
2105 doi:10.1016/j.pce.2015.04.002, 2016.

2106 Tobo, Y., Adachi, K., DeMott, P. J., Hill, T. C. J., Hamilton, D. S., Mahowald, N. M., Nagatsuka,
2107 N., Ohata, S., Uetake, J., Kondo, Y. and Koike, M.: Glacially sourced dust as a potentially
2108 significant source of ice nucleating particles, *Nat. Geosci.*, 12(April), 253–258,
2109 doi:10.1038/s41561-019-0314-x, 2019.

2110 Turquety, S., Logan, J. A., Jacob, D. J., Hudman, R. C., Leung, F. Y., Heald, C. L., Yantosca, R.
2111 M., Wu, S., Emmons, L. K., Edwards, D. P. and Sachse, G. W.: Inventory of boreal fire
2112 emissions for North America in 2004: Importance of peat burning and pyroconvective injection,
2113 *J. Geophys. Res. Atmos.*, 112(12), 1–13, doi:10.1029/2006JD007281, 2007.

2114 Ulery, A. L. and Graham, R. C.: Forest Fire Effects on Soil Color and Texture, *Soil Sci. Soc. Am.
2115 J.*, 57(1), 135–140, doi:10.2136/sssaj1993.03615995005700010026x, 1993.

2116 Wagenbrenner, N. S., Chung, S. H. and Lamb, B. K.: A large source of dust missing in
2117 Particulate Matter emission inventories? Wind erosion of post-fire landscapes, *Elem Sci Anth*,
2118 5(2), 1–10, doi:10.1525/elementa.185, 2017.

2119 Wagner, R., Jähn, M. and Schepanski, K.: Wildfires as a source of airborne mineral dust -
2120 Revisiting a conceptual model using large-eddy simulation (LES), *Atmos. Chem. Phys.*, 18(16),
2121 11863–11884, doi:10.5194/acp-18-11863-2018, 2018.

2122 Wang, R., Balkanski, Y., Boucher, O., Bopp, L., Chappell, A., Ciais, P., Hauglustaine, D.,
2123 Peñuelas, J. and Tao, S.: Sources, transport and deposition of iron in the global atmosphere,
2124 *Atmos. Chem. Phys.*, 15(11), 6247–6270, doi:10.5194/acp-15-6247-2015, 2015.

2125 Ward, D. E. and Hardy, C. C.: Smoke emission from wildland fires, *Environ. Int.*, 17(2–3), 117–
2126 137, 1991.

2127 Ward, D. S., Kloster, S., Mahowald, N. M., Rogers, B. M., Randerson, J. T. and Hess, P. G.:
2128 The changing radiative forcing of fires: Global model estimates for past, present and future,
2129 *Atmos. Chem. Phys.*, 12(22), 10857–10886, doi:10.5194/acp-12-10857-2012, 2012.

2130 Weber, R. J., Guo, H., Russell, A. G. and Nenes, A.: High aerosol acidity despite declining
2131 atmospheric sulfate concentrations over the past 15 years, *Nat. Geosci.*, 9(April), 1–5,
2132 doi:10.1038/NGEO2665, 2016.

2133 Wu, C., Liu, X., Diao, M., Zhang, K., Gettelman, A., Lu, Z., Penner, J. E. and Lin, Z.: Direct
2134 comparisons of ice cloud macro- and microphysical properties simulated by the Community
2135 Atmosphere Model version 5 with HIPPO aircraft observations, *Atmos. Chem. Phys.*, 17(7),
2136 4731–4749, doi:10.5194/acp-17-4731-2017, 2017.

2137 Wu, M., Liu, X., Zhang, L., Wu, C., Lu, Z., Ma, P. L., Wang, H., Tilmes, S., Mahowald, N.,
2138 Matsui, H. and Easter, R. C.: Impacts of Aerosol Dry Deposition on Black Carbon Spatial
2139 Distributions and Radiative Effects in the Community Atmosphere Model CAM5, *J. Adv. Model.*
2140 *Earth Syst.*, 10(5), 1150–1171, doi:10.1029/2017MS001219, 2018.

2141 Xu, N. and Gao, Y.: Characterization of hematite dissolution affected by oxalate coating, kinetics
2142 and pH, *Appl. Geochemistry*, 23(4), 783–793, doi:10.1016/j.apgeochem.2007.12.026, 2008.

2143 Yamasoe, M. A., Artaxo, P., Miguel, A. H. and Allen, A. G.: Chemical composition of aerosol
2144 particles from direct emissions of vegetation fires in the Amazon Basin: Water-soluble species
2145 and trace elements, *Atmos. Environ.*, 34(10), 1641–1653, doi:10.1016/S1352-2310(99)00329-5,

2146 2000.

2147 Zender, C. S., Bian, H. and Newman, D.: Mineral Dust Entrainment and Deposition (DEAD)
2148 model: Description and 1990s dust climatology, *J. Geophys. Res.*, 108(D14),
2149 doi:10.1029/2002JD002775, 2003.

2150 Zhang, Y., Mahowald, N., Scanza, R. A., Journet, E., Desboeufs, K., Albani, S., Kok, J. F.,
2151 Zhuang, G., Chen, Y., Cohen, D. D., Paytan, A., Patey, M. D., Achterberg, E. P., Engelbrecht, J.
2152 P. and Fomba, K. W.: Modeling the global emission, transport and deposition of trace elements
2153 associated with mineral dust, *Biogeosciences*, 12(19), 5771–5792, doi:10.5194/bg-12-5771-
2154 2015, 2015.

2155 Zhu, X., Prospero, J. and Millero, F.: Diel variability of soluble Fe(II) and soluble total Fe in North
2156 Africa dust in the trade winds at Barbados, *J. Geophys. Res.*, 102(7), 21297–21305, 1997.

2157 Zhuang, G., Yi, Z., Duce, R. A. and Brown, P. R.: Link between iron and sulphur cycles
2158 suggested by detection of Fe(n) in remote marine aerosols, *Nature*, 355(6360), 537–539,
2159 doi:10.1038/355537a0, 1992.

2160